The Effects of Tides and Submesoscale Mixed Layer Eddies on Deep Convection in the Labrador Sea: Simulations at Resolutions Consistent with Coupled Climate Models

by

Rowan Brown

A thesis submitted in partial fulfilment of the requirements for the degree of

Master of Science

Department of Earth and Atmospheric Sciences

University of Alberta

Abstract

The Intergovernmental Panel on Climate Change predicts that the large-scale overturning circulation will weaken over the 21st century. As with many other oceanic consequences of anthropogenic climate forcing, such as increased warming, acidification, glacial and sea ice melt, marine heatwaves, and coastal erosion, the high latitudes are predicted to be most strongly affected. A key tool in making these predictions is global coupled climate models, which in the most recent Coupled Model Intercomparison Project (phase 6) commonly utilized ocean components with resolutions of 1 to 1/4°.

The accurate representation of deep convection, a vertical mixing process connecting the surface and abyssal flows, is crucial for accurately predicting the future of the overturning circulation. Simultaneously, it is also a challenge due to the small scales of motion involved. In this monograph, we evaluate the effects of two processes on deep convection in the Labrador Sea, a key site of overturning in the western North Atlantic. We find that both processes, namely tidal forcing and the submesoscale mixed layer eddy parameterization (SMLEp), decrease deep mixed layer depth biases in a 1/4° regional atmospherically-forced model. The mechanisms by which they effect this change are less clear. Both tidal forcing and the SMLEp can alter the lateral boundary current-interior exchange of buoyancy, which can affect stratification. However, fluxes due to tidal forcing are characterized by a cooling and freshening whereas those from the SMLEp either become warmer and saltier or do not change (depending on the atmospheric forcing product). This is likely related to differences in how tidal forcing and the SMLEp affect boundary instabilities, especially baroclinic instabilities, through the water column. What is more clear, however, is that the principal behaviour of

the SMLEp is not to alter the boundary fluxes but to slump isopycnals and accelerate post-convection restratification. To summarize, we find that both tidal forcing and the SMLEp could serve as valid tools for improving MLD biases in future medium-resolution (e.g., 1/4°) coupled climate models, which commonly experience unrealistically deep convection.

Preface

This thesis is an original work by Rowan Brown. No part of this thesis has been previously published. We would like to acknowledge the support of a Canada Graduate Scholarships - Master's program (CGS M) award from the Natural Sciences and Engineering Research Council of Canada (NSERC).

Acknowledgements

First and foremost, I want to thank my supervisor, the indefatigable Dr. Paul Myers, for his outstanding guidance, optimism, and near-constant availability despite having a workload bigger than any other to which I have personally borne witness.

I also want to thank my parents, Kyla and Dave, for their unwavering support, and my brother, Dawson, for keeping me buoyed with late-night games of GeoGuessr. I would like to thank my grandparents, Poppa, Grandpa, Ganny and Nana, for their unconditional love and more.

Among the Geophysical Fluids Dynamics lab, Tahya deserves very special thanks for putting up with the rest of us and our varying degrees of programming (in)competence. Thanks as well to my other past and present labmates, in no particular order: Enrico, Mukulika, Diego, Robin, Adam, Hannah, Pouneh, Kehan, Alain, Akash, Ana, and honourary member Scott, for making Edmonton much more than bearable.

I also want to give special thanks to Drs. Bruce Sutherland, Clark Pennelly, Andrew Hamilton, and Laura Gillard McFarlane for their leadership and guidance. Similarly, although they will never read this, I want to thank Drs. Brian Veitch, David Molyneux, and Changheng Chen for playing instrumental roles in my journey to grad school.

Finally, thanks to Jake Burns, David Bowie, and Nick Drake for keeping me company during many late nights spent toiling in CCIS 3-217.

Contents

List of Figures

List of Tables

Abbreviations

AMOC: Atlantic Meridional Overturning Circulation
ANHA4: Arctic and Northern Hemisphere Atlantic 1/4°
BCE: Boundary Current Eddy
BC: Baroclinic Instability
BT: Barotropic Instability
CE: Convective Eddy
CGRF: Canadian Meteorological Centre's (CMC) Global Deterministic Prediction System (GDPS) Reforecasts
CMIP: Coupled Model Intercomparison Project (phase 5: CMIP5; phase 6: CMIP6; etc.)
CORE: Coordinated Ocean-ice Reference Experiments
DLC: Deep Labrador Current
DSOW: Denmark Strait Overflow Water
DWBC: Deep Western Boundary Current
E-P: Evaporation minus Precipitation
ECMWF: European Centre for Medium-Range Weather Forecasts
EGC: East Greenland Current
ERA-I: ECMWF Re-Analysis Interim
FESOM: Finite-Element/volumE Sea ice-Ocean Model
FWC: Freshwater Content
GHG: Greenhouse gas
HC: Heat Content
HYCOM: HYbrid Coordinate Ocean Model
IC: Irminger Current
IPCC: Intergovernmental Panel on Climate Change
IR: Irminger Ring
LC: Labrador Current
LES: Large Eddy Simulation

LIM2: Louvain-la-neuve Ice Model
LS: Labrador Sea
LSW: Labrador Sea Water
MHW: Marine heatwave
MITgcm: Massachusetts Institute of Technology general circulation model
MLD: Mixed Layer Depth
MOM: Modular Ocean Model
NA: North Atlantic
NADW: North Atlantic Deep Water
NEMO: Nucleus for European Modelling of the ocean
OGCM: Ocean General Circulation Model
OPA: Océan PArallélisé
OSNAP: Overturning in the Subpolar North Atlantic Program
RAPID-MOCHA: Rapid Climate Change-Meridional Overturning Circulation and Heatflux Array
SMLE: Submesoscale Mixed Layer Eddy
SMLEp: Submesoscale Mixed Layer Eddies parameterization
WAIS: West Antarctic Ice Sheet
WGC: West Greenland Current
WGCC: West Greenland Coastal Current

Chapter 1

Introduction

Anthropogenic greenhouse gas (GHG) emissions have unequivocally caused warming of the climate; according to the recent Sixth Assessment Report from the Intergovernmental Panel on Climate Change (IPCC), the global surface temperature reached 1.1°C above the 1850–1900 average during 2011–2020. It is predicted that this value will increase to 1.5°C by the early 2030s, and that it will be very difficult to avoid an increase of 2.0°C by the end of the current century (Lee et al., 2023).

Ocean warming has accounted for 91% of this heating, with the remaining 9% being taken up by land, the cryosphere, and the atmosphere (Lee et al., 2023). The effects of this oceanic heat uptake, along with other facets of ocean change such as increased freshwater input from glacial melt and the oceanic dissolution of GHG emissions, are manifesting diversely and will directly or indirectly affect all people on Earth (Pörtner et al., 2019). It is furthermore incumbent to note that, as with many facets of climate change, it is poor and marginalized communities—who have historically contributed the least to GHG emissions—that are disproportionately exposed to oceanic change (Pörtner et al., 2019; Lee et al., 2023). This is exemplified by the Alaska Inuit village of Shishmaref: As wintertime sea ice cover decreases, the protection it provides from storm-driven coastal erosion is waning, and the community now faces inevitable relocation as the ground beneath it is washed away (Hamilton et al., 2018).

Climate change and its effects on the ocean, such as those above, are central to the motivation for this thesis. My specific focus is deep convection in the Labrador Sea (LS), a marginal sea in the western North Atlantic (NA). In the LS, deep convection occurs seasonally due to cold winter air temperatures, regularly deepening the mixed layer beyond 1,000–2,000 m (Lab Sea Group, 1998; Yashayaev & Loder, 2016; Gillard et al., 2022). This, in turn,

has relevance to the large-scale circulation, sea level rise, sea ice and glacier loss, and marine biogeochemistry. I believe it is therefore important, to contextualize LS deep convection within the broader climate, to begin in the following section with a brief discussion on the oceanic response to climate change. I will then focus my attention on the dynamics of the large-scale circulation—that is, the Atlantic Meridional Overturning Circulation (AMOC)—before further focusing on the Labrador Sea, deep convection, and finally my specific research question.

1.1 The oceans under climate change

One of the foremost consequences of climate change on the ocean is a projected weakening of the large-scale circulation; for all GHG emissions scenarios, the IPCC predicts that the AMOC will very likely slow down over the 21st century (Lee et al., 2023). The formation of deep waters through deep convection in the NA has long been central to this discussion, since it is the main process connecting the meridional surface and abyssal flows (Buckley & Marshall, 2016; Lozier, 2023). And since the AMOC is responsible for approximately 1.3 PW of meridional heat transport at 26° N, which is 25% of the combined oceanic and atmospheric poleward heat flux (Johns et al., 2011), a slowdown of this transport would have severe implications and potentially modulate the progression of climate change. The AMOC is similarly important for the meridional transport and sequestration of freshwater, carbon dioxide (CO_2), oxygen, and other nutrients, meaning that the effects of a slowdown will unquestionably extend into the biogeochemistry of marine organisms (Johns et al., 2011; Buckley & Marshall, 2016; Lozier, 2023).

Large oscillations in the AMOC's strength are not unprecedented, and climate variability has long been linked to ocean dynamics by paleoceanographers. In fact, past millennial-scale climate warming and cooling has been directly attributed to variability in the AMOC (Lozier et al., 2019). For one example, during the most recent ice age, pronounced evidence in ice-core records revealed warming and cooling superimposed on the glacial timescale, and analyses of multiple proxies suggested a connection between these oscillations and the AMOC (Hirschi et al., 2020). However, the incipient AMOC weakening is likely to occur on an accelerated timescale, compared to past oscillations, and it is the abruptness of this change that is most threatening to human systems and marine life. Its direct impacts will likely include decreases in marine productivity in the NA, increases in winter storms over Europe, and reductions in rainfall over the Sahel and South Asia (Pörtner et al., 2019).

Furthermore, as intimated above, the impacts of climate change on the ocean will extend

far beyond those related directly to the AMOC. One important example is global sea level rise, which is currently increasing by 3.7 mm yr^{-1} and which is predicted to reach 0.28–1.01 m by 2100, depending on future GHG emissions (Lee et al., 2023). Crucially, it is becoming clear that a portion of future ice shelf melting, which is responsible for sea level rise, is likely unavoidable due to the long timescales of response from ice shelves to climate forcing. A recent modelling study by Naughten et al. (2023) illustrates this point, identifying little difference in future West Antarctic Ice Sheet (WAIS) loss between the mid-range and the most ambitious GHG emissions targets. This means that mitigation of future GHG emissions might not prevent loss of the WAIS, which contains enough ice to raise the global sea level by 5.3 m. The main cause of this loss is now thought to be ocean-driven basal melting, specifically relating to the upwelling of warm intermediate water onto the continental shelf (Morrison et al., 2020; Naughten et al., 2023). This process has also been linked to the record Antarctic minimum sea ice extent of February 2023, which was approximately 36% less than climatological values (Purich & Doddridge, 2023).

In addition to accelerating ice loss, ocean warming will directly cause disruptions in nutrient cycles, impacting all trophic levels from phytoplankton to fisheries. In fact, it has already contributed to an overall decrease in the maximum catch potential throughout the 20th century, and it is predicted to cause further decreases in fish stocks by 3% per decade, directly impacting human food production (Pörtner et al., 2019; Lee et al., 2023).

Concomitantly with ocean warming, marine heatwaves (MHWs) have doubled in frequency and are becoming more intense and longer lasting. These trends are expected to continue; results from the Coupled Model Intercomparison Project phase 5 (CMIP5) suggest that the frequency of MHWs by the late 21st century will be 20–50 times greater than during 1850–1900. This will cause myriad lasting ecosystem consequences, including to critical foundation species like seagrass and kelp (Pörtner et al., 2019; Richaud et al., 2024). These effects will be particularly severe at high latitudes, where polar amplification has caused the Arctic to warm four times faster than the global average. A recent modelling study by Richaud et al. (2024) illustrates this phenomenon, predicting increases in the frequency and duration of Arctic MHWs triggered by surface heat flux, which itself is increasing due to the strengthening ice-albedo feedback.

Increasing acidification is also predicted, which will impact marine ecosystems around the globe (Beaupré-Laperrière et al., 2020). Ocean acidification is caused by the dissolution of atmospheric CO_2, which leads to a decrease in pH by way of chemical reactions with seawater and carbonic acid, causing waters to become undersaturated with the mineral forms of calcium carbonate (Beaupré-Laperrière et al., 2020; Fennel et al., 2022). In the

broader context of climate change, CO_2 dissolution in the ocean reduces its accumulation in the atmosphere and hence slows climate warming. However, the resultant carbonate-undersaturated waters can lead many calcifying organisms to undergo dissolution or severely hindered growth. This is especially true within the already low-alkalinity waters of the polar oceans (Beaupré-Laperrière et al., 2020).

Global biogeochemical modelling suggests that surface acidification is driven mainly by the concentration of atmospheric CO_2 (Fennel et al., 2022). Hence, even under a low future GHG emissions scenario, the IPCC predicts with virtual certainty that ocean pH will continue to decline. Furthermore, under high GHG emissions, it is likely that the polar oceans will experience year-round undersaturation of calcium carbonate minerals by the end of the 21st century (Pörtner et al., 2019). This will adversely affect fisheries and other food production, particularly shellfish aquaculture (Lee et al., 2023).

As warming and acidification are predicted to progress, so too is deoxygenation, with the potential for all three to create compounding stresses on marine ecosystems (Pörtner et al., 2019; Fennel et al., 2022; Lee et al., 2023). This represents a continuation of the current trend, in which the global average ocean oxygen content has decreased by 2% over the past 50 years (Fennel et al., 2022). One cause of this deoxygenation, among others relating to changes in biogeochemical cycles, is the potential for a slowdown in the large-scale circulation and reductions in ventilation of the deep ocean (Rhein et al., 2017; Fennel et al., 2022).

1.2 The Atlantic Meridional Overturning Circulation

The AMOC is a zonally-averaged description of the complex three-dimensional circulation of the Atlantic Ocean (Buckley & Marshall, 2016). It includes many processes that act on differing timescales, like wind-driven Ekman transport, which exhibits high-frequency variability, and lower-frequency buoyancy anomalies, which can occur for myriad reasons on intra-annual to decadal timescales (Lozier, 2023).

The AMOC can be defined as a streamfunction, Ψ, for volume transport integrated zonally and in depth. Based on the velocity field $v(x, y, z)$, Ψ is calculated as follows:

$$\Psi(y, z) = \int_{x_w}^{x_e} \int_{z}^{\eta} v \; dx \; dz, \tag{1.1}$$

where v is the meridional velocity, x_e and x_w are the limits of zonal integration (east and west, respectively), η is the free surface height, and z is a vertical coordinate increasing upward. Its strength is described as the maximum of Ψ in the water column at each latitude, or

$\Psi_{\max}(y) = \max_z \Psi(y, z)$. Alternatively to z, these expressions can also be represented using a different seawater property such as density or temperature (Buckley & Marshall, 2016; Hirschi et al., 2020).

In the NA, the AMOC can be characterized by two branches of flow; at the surface, it is generally northward, warm, and saline, whereas at depth it is generally southward, cold, and fresh. These two branches are connected by deep convection in the Labrador and Nordic Seas, where buoyancy forcing supplies the lower branch with young, ventilated deep waters. The densest of these waters are formed in the Nordic Seas, north of the Greenland-Scotland Ridge, and are termed overflow waters. In the Labrador Sea, west of Greenland, an intermediate water mass is formed termed Labrador Sea Water (LSW) (Lozier, 2023).

The AMOC plays a central role in the climate, and it accounts for 70% of the poleward oceanic heat transport (Johns et al., 2011). It is also responsible for 41% of the global air-sea CO_2 flux (Lozier, 2023), simultaneously slowing its atmospheric accumulation, thus modulating the trajectory of climate change, while also leading to increased acidification (Buckley & Marshall, 2016; Fennel et al., 2022). Long-term CO_2 sequestration in the ocean is achieved by deep convection, which injects CO_2-rich surface waters into the interior NA. Simultaneously, deep convection is also a main contributor of oxygen and other tracers like chlorofluorocarbons into the abyssal ocean (Rhein et al., 2017).

The AMOC has been colloquially termed 'the ocean conveyor belt' (Lozier, 2023), which permits its mean state to be illustrated pictorially using a series of connected arrows. Figure 1.1 exemplifies this paradigm, with northward-flowing, warm surface waters in red and southward-flowing, cold deep waters in blue. The Nordic Seas and the LS are annotated, as these are the prototypical sites of deep convection in the North Atlantic.

However, it is important to note that the AMOC is in reality complex and highly variable (Buckley & Marshall, 2016). Lagrangian studies show that it is replete with recirculation gyres (Bower et al., 2019); in Figure 1.1, one such example is the Northern Recirculation Gyre, represented by a blue arrow retroflecting northward off the east coast of North America. Recirculation is similarly important at the Tail of the Grand Banks, south of the Labrador Sea, where the Labrador Current (LC) bifurcates. Here, a portion continues southward while the majority joins the North Atlantic Current (NAC), with a fraction of this branch even partially recirculating into the LS via the Irminger Sea (IS) (Fratantoni & McCartney, 2010).

As with the AMOC's spatial variability, its temporal variability is also complex. Once largely the purview of paleoceanographers, its variability in time was interpreted on millennial-scales (Lozier, 2023), and its changes were frequently invoked as key players in paleoclimate shifts (Buckley & Marshall, 2016). However, with the onset of anthropogenic

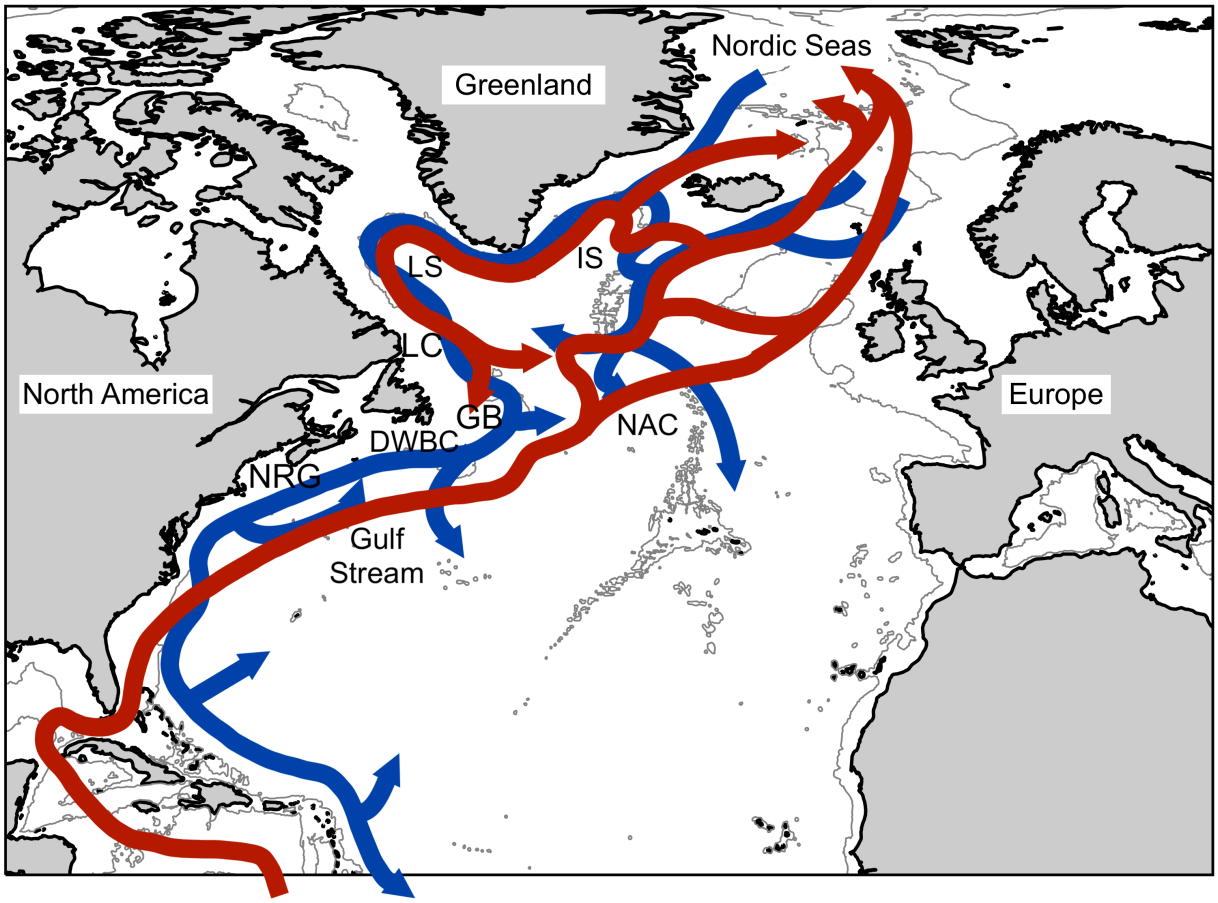

Figure 1.1: A simplified depiction of the AMOC conveyor belt focused on the North Atlantic. Northward-flowing, warm surface waters are depicted in red, and southward-flowing, cold deep waters are in blue. Abbreviations: The Labrador Sea (LS), the Irminger Sea (IS), the North Atlantic Current (NAC), the Deep Western Boundary Current (DWBC), the Northern Recirculation Gyre (NRG), the Labrador Current (LC), and the Grand Banks (GB). Adapted from Bower et al. (2019).

climate change, interest has grown in its variability on decadal or shorter timescales. For example, in Lenton's seminal 2008 paper introducing the concept of climate tipping points, a shutdown of the thermohaline circulation (of which the AMOC is a main component) is considered a potential future tipping element (Lenton et al., 2008). To wit: It was realized that strong and rapid anthropogenic warming might increase surface stratification, inhibit deep convection in the NA, and shutdown the AMOC (Lozier, 2023). One recent study uses statistical methods to predict with 95% confidence that this will begin during 2025–2095 (Ditlevsen & Ditlevsen, 2023). However, numerical modelling studies like those used in the IPCC's recent Sixth Assessment Report indicate that this is unlikely; rather, it is predicted that the AMOC will slow but not shutdown by 2100 (Lee et al., 2023).

The observational record, including shipboard hydrography beginning during the 1920s and transbasin mooring arrays implemented throughout the 21st century (McCarthy et al.,

2020), has exhibited no long-term or systematic changes for at least 50 years (Buckley & Marshall, 2016). Rather, they reveal a consistent long-term average transport of roughly 15 Sv (Buckley & Marshall, 2016). This figure depends on latitude; from seven years of measurement by the RAPID-MOCHA (Rapid Climate Change-Meridional Overturning Circulation and Heatflux Array) array at 26° N, the mean transport was found to be 18.5 Sv (Morison et al., 2012).

Crucially, modelling and observations have revealed that short-term variability is high; over only one year of measurement the overturning at 26° N strengthened sixfold (Lozier, 2023). This variability is driven by high-frequency wind forcing with limited basin-scale coherence. Rather, basin-scale variability is driven by high-amplitude buoyancy forcing in the NA (Buckley & Marshall, 2016; Lozier et al., 2019; Menary et al., 2020). In this region, results from the Overturning in the Subpolar North Atlantic Program (OSNAP) indicate that the overturning is dominated by buoyancy transformations in the Iceland and Irminger Seas (Lozier, 2023). Subsequently, these dense waters are exported southward within the Deep Western Boundary Current (DWBC) and via internal pathways in the abyssal Atlantic (Buckley & Marshall, 2016; Bower et al., 2019; Lozier, 2023).

The role of the LS in this process is debated. At minimum, the dense, ventilated waters formed in the eastern subpolar NA are later supplemented and undergo freshening within the LS (Petit et al., 2023). This is supported in part by OSNAP observations, which found that, although the eastern NA accounts for the bulk of the meridional volume and heat transport, the LS contributes equally to the freshwater transport. Furthermore, a recent modelling study showing good agreement with the OSNAP results (i.e., overturning is dominated by the eastern NA), has indicated that multi-decadal variability in the AMOC is driven by anomalous deep water production in the LS (Yeager et al., 2021). Hence, deep convection in the LS likely plays some role in the dynamics of the AMOC, even if this role is not yet fully understood.

1.3 The Labrador Sea

The LS is a subpolar marginal sea in the NA, situated between Greenland and Labrador. It experiences extremes in wintertime cold and wind, which help to make it one of the few areas of deep convection in the world (Lab Sea Group, 1998). As a result of this deep convection, it produces a distinct water mass, LSW, which is later exported southward as the lightest component of the North Atlantic Deep Water (NADW), within the AMOC lower limb (Rhein et al., 2017).

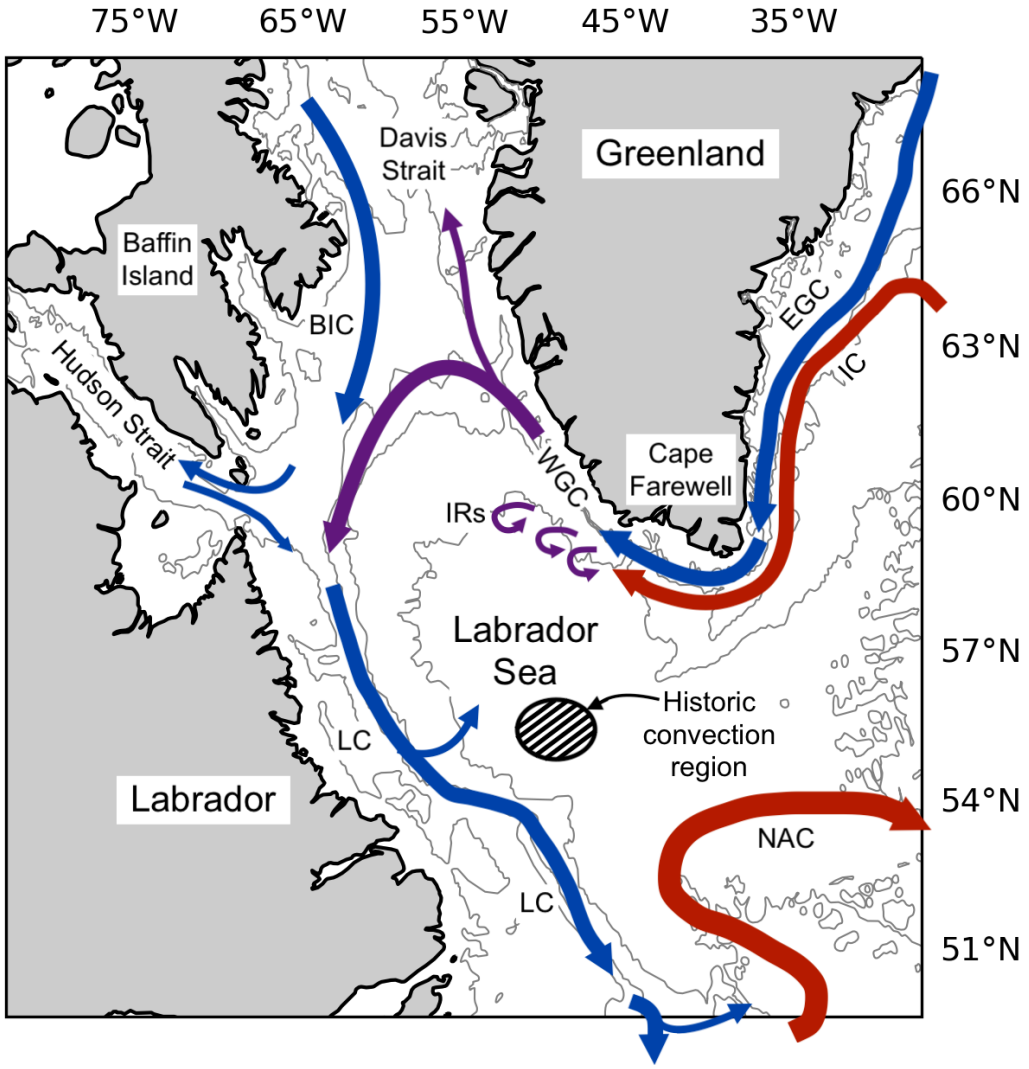

Figure 1.2: Depiction of the main currents bordering the Labrador Sea, including the Irminger Current (IC) and the East Greenland Current (EGC), which merge at Cape Farewell to form the West Greenland Current (WGC), and the Baffin Island Current (BIC), which merges with the WGC to form the Labrador Current (LC). The historical deep convection patch is indicated by black and white stripes. Irminger Rings (IRs), which are depicted fluxing off of the WGC, work in concert with relatively fresh fluxes from the LC to suppress deep convection except in this region. Adapted from Fratantoni and Pickart (2007) and Pennelly and Myers (2022).

The LS is surrounded by cyclonic-flowing boundary currents, shown in Figure 1.2; the West Greenland Current (WGC) is to the east, the Labrador Current (LC) is to the west, and the North Atlantic Current (NAC) is to the south. Through fluxes of heat and freshwater, these currents modulate deep convection within the interior LS, and hence control the production of LSW as well as its southward export pathways.

The WGC is formed by the merging of the Irminger Current (IC) and the East Greenland Current (EGC). The former, originating in the subpolar NA, is characterized by warm and

salty Atlantic waters. Conversely, the latter contains a high volume of Arctic-origin freshwater exported through Fram Strait. The WGC contains a strong front over the shelfbreak in the vicinity of its main jet, separating the relatively cold and fresh inland waters (originating in the EGC) from the warm and salty offshore waters (characterized by the IC). It is important to note that these two branches are not distinguishable in velocity, and are only defined by their hydrographic properties (Fratantoni & Pickart, 2007). Within the inshore branch, salinity decreases until Cape Desolation due to melt and runoff from Greenland. Volume transport also peaks at Cape Desolation. Later, mixing as the current travels north reduces this transport and increases salinity (Myers et al., 2009). The WGC exhibits seasonal oscillations in its properties, and is summer intensified with a maximum in freshwater transport (Rykova et al., 2015).

The LC flows southward along the coast of Labrador, and like the WGC, contains two branches; waters on the continental shelf are cold and fresh whereas beyond the shelfbreak they are warmer and saltier (Fratantoni & Pickart, 2007). These two branches are strongly baroclinic and barotropic, respectively (Lazier & Wright, 1993). Unlike the WGC, the LC is winter intensified, likely for reasons relating to its source waters (Rykova et al., 2015). It is formed by the merging of the WGC, the majority of which flows westward across Davis Strait, with the Baffin Island Current (BIC), which contains cold and fresh water of Arctic Origin. Below this and along the deep continental slope is the Deep Labrador Current (DLC). The DLC is part of the vigorous DWBC, with a large barotropic component carrying the bulk of the Sverdrup return flow of the subpolar gyre (Fratantoni & Pickart, 2007) along with ventilated NADW (Dengler et al., 2006). NADW can be further broken into LSW, its lightest component, and denser ventilated waters from the upstream overflow regions in the eastern NA.

Two types of eddies are responsible for fluxing heat and freshwater from the boundary currents into the interior LS: Irminger Rings (IRs) and Boundary Current Eddies (BCEs). Variability in these fluxes is complex and dependent on many factors, including current speeds (Gou et al., 2023), seasonal and longer variations in the horizontal density gradient (De Jong et al., 2016), the North Atlantic Oscillation (Myers et al., 2009), and more. Modelling studies have found that excess freshwater in the WGC would therefore not necessarily enter the interior LS and shutdown deep convection; rather, depending on myriad factors, a large portion of it would likely transit around the boundary before heading south within the LC (Myers, 2005; Zhang et al., 2021).

Traditionally, IRs are said to be generated from barotropic instabilities within the WGC due to rapidly steepening bathymetry off Cape Desolation. They are characterized by high

eddy kinetic energy (EKE), large diameters of around 45 km, and high buoyancy (Chanut et al., 2008). IRs tend to be found in the northern LS where their high buoyancy, resulting from a fresh surface layer and core of warm, salty Irminger water, suppresses deep convection until the eddy decays, occasionally even contributing to deep convection later in life (Pennelly & Myers, 2022). Based on recent very-high resolution modelling studies, there is now some debate on the types of instabilities that generate IRs; it is possible that baroclinic instabilities play a role near the bottom (Rieck et al., 2019), and that the strength of the baroclinicity could control the direction of eddy rotation (Pennelly & Myers, 2022).

BCEs are generated by weakly energetic baroclinic instabilities throughout the length of the boundary currents, from Cape Farewell to the Grand Banks. Like IRs, BCEs contain a highly stratified core that is fresh and cold at the surface and warm and salty at depth (Rieck et al., 2019). They are a major source of EKE in the southern LS and a minor source in the north, where they work in concert with IRs to limit deep convection. BCEs transport heat towards the interior LS from both the LC and the WGC, although they are more efficient on the WGC side (Chanut et al., 2008). Here, baroclinic instabilities in the upper 1,000 m are as much as twice as strong as barotropic instabilities of the kind that generate IRs (Gou et al., 2023). This results in a patch of uninhibited preconditioning in the southwest LS, which later overturns and produces LSW. This zone is indicated by black and white stripes in Figure 1.2.

LSW is characterized by low salinities, low potential vorticity (i.e., total vorticity scaled by depth), and high concentrations of dissolved tracers (Rhein et al., 2017). Some authors define it in terms of density classes, such as Kieke et al. (2007) and Garcia-Quintana et al. (2019), who use 1,027.68–1,027.80 kg m^{-3}, or Courtois et al. (2020), who use 1,027.68–1,027.82 kg m^{-3}. LSW is the lightest component of the NADW, and it is advected out of the Labrador Sea after joining the DLC, which forms part of the DWBC. The DWBC extends throughout the NA, transporting young ventilated waters southward towards the equator. In addition to LSW, it contains deeper, ventilated waters from the upstream overflow regions east of Greenland. The DLC is principally barotropic throughout its interior (Dengler et al., 2006), with a strong baroclinic component near a bottom core characterized mainly by Denmark Strait Overflow Water (DSOW) (Fischer et al., 2010).

Average transport in the DWBC is around 30 Sv, depending on latitude, recirculation gyres, etc. (Dengler et al., 2006; Fischer et al., 2010). It is the fastest pathway for LSW flowing south (Gary et al., 2012; Rhein et al., 2015). However, its waters are continuously shed into the interior NA, with significant detrainment around the Tail of the Grand Banks (Gary et al., 2012; Rhein et al., 2015). From here, an unquantified amount of LSW is

exported out of the subpolar gyre following southward interior pathways, mainly along the Mid-Atlantic Ridge (MAR). Additional LSW crosses the MAR into the eastern subpolar NA or recirculates into the LS via the Irminger Sea (Kieke et al., 2009; Bower et al., 2019). Both the DWBC and interior pathways are therefore important for the export of LSW. Interior pathways are also important because they bring ventilated water carrying CO_2 and oxygen into the abyssal interior (Kieke et al., 2009).

1.4 Deep convection in the Labrador Sea

Deep convection is a rare mixing process found in three areas of the global ocean: the Labrador Sea, the Nordic Seas, and the Mediterranean Sea (Marshall & Schott, 1999). The deepest mixed layer ever recorded in the LS occurred during winter 1994, when the MLD reached approximately 2,400 m (Yashayaev & Loder, 2016). Shallower convection is more common globally, such as in the Southern Ocean, where it plays a crucial role in drawing warm, melt-inducing waters onto the Antarctic shelf (Morrison et al., 2020; Bennetts et al., 2023).

There are three requirements for seasonal deep convection which are satisfied within the LS: Strong atmospheric forcing, where cold and dry winds from over land or ice induce significant heat flux at the sea surface; pre-existing weak stratification in the water column, which occurs in part due to deep convection from the previous year; and underlying waters that are consistently brought to the surface. The latter is favoured by cyclonic circulation, such as that within the boundary currents around the LS, which causes the doming of isopycnals (Lab Sea Group, 1998).

The first stage of deep convection is *preconditioning* (stage I), during which gyre-scale circulation and buoyancy forcing predispose an area to overturn by bringing weakly stratified interior waters close to the surface. This weak stratification is exemplified in panel (b) of Figure 1.3, which shows a weakly stratified section across the Labrador Sea. As winter sets in, vigorous buoyancy loss and cooling events trigger *active deep convection* (stage II), where the water column is rapidly and deeply homogenized within numerous plumes on lateral scales of O(1 km). Panel (c) shows a convectively-homogenized water column on the leftmost side yielding to more stable stratification on the rightmost side, near the continental shelf. Since Figure 1.3 comes from a hydrostatic 1/4° resolution OGCM, convective plumes of O(1 km) cannot be captured. Hence, only the larger mixed patch is visible. Later, post-convection *lateral exchange* (stage III) takes over as atmospheric cooling ceases and geostrophic scale baroclinic eddies mix the convective patch with its surroundings. This is shown in panel

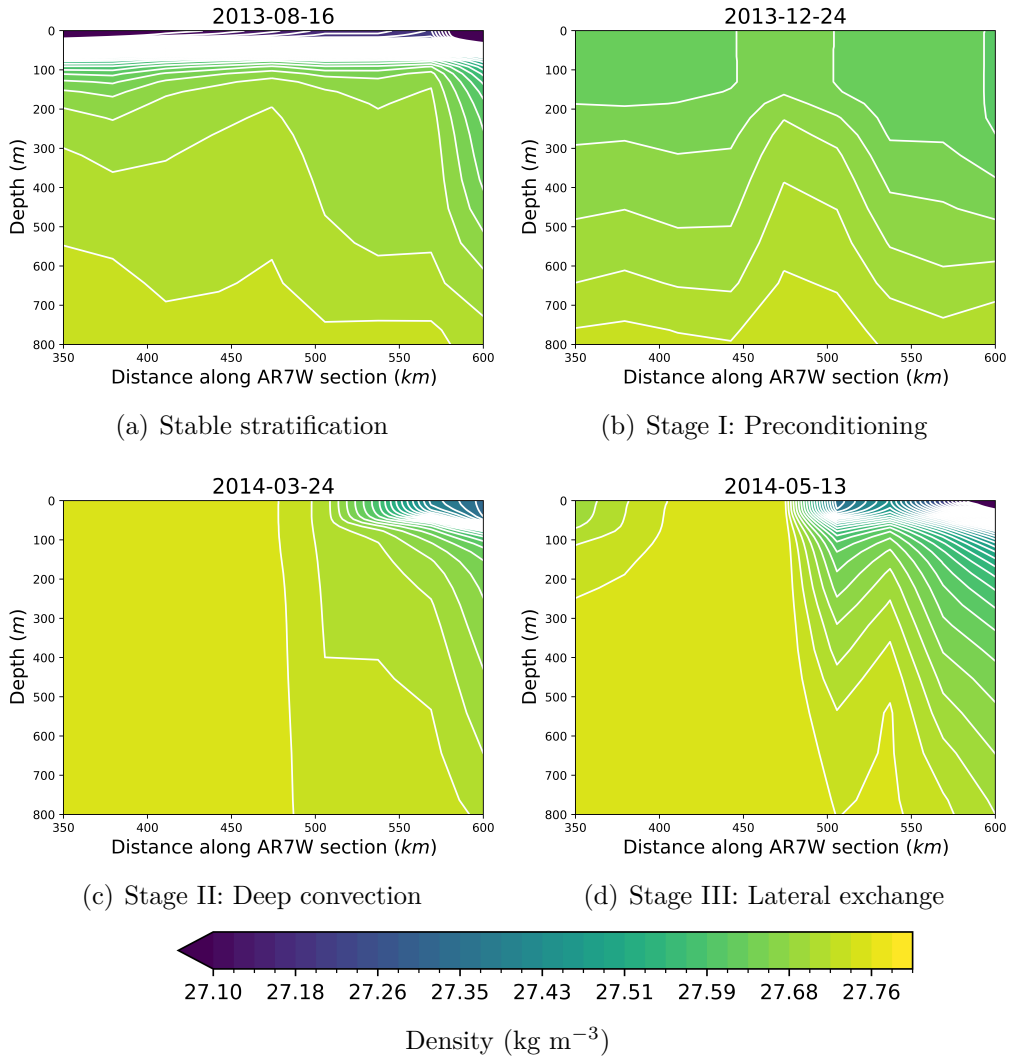

(a) Stable stratification

(b) Stage I: Preconditioning

(c) Stage II: Deep convection

(d) Stage III: Lateral exchange

Figure 1.3: The three stages of deep convection in the interior Labrador Sea, across the AR7W section. White lines are isopycnals of potential density between 1,027.1–1,027.8 kg m^{-3}. **(a)** Stable stratification in late summer. **(b)** Stage I: Preconditioning, where stratification is reduced and the surface is predisposed to overturn. **(c)** Stage II: Active deep convection, where the surface is homogenized beyond 800 m. **(d)** Stage III: Lateral exchange, where mixing with the surrounding ocean begins to restore stratification. The colour bar indicates density following σ_T convention. All figures are 5-day averages from a 1/4° resolution ocean General Circulation Model. Dates are arbitrary, and are chosen to be representative of the progression of deep convection over roughly one year.

(d). As the fluid disperses, stratification reforms; panel (a) shows this stable state (Lab Sea Group, 1998; Marshall & Schott, 1999).

During post-convection lateral exchange, as the water column restratifies and the mixed layer shoals, LSW is subducted into the permanent thermocline (Courtois et al., 2020). Later, a portion of this relatively fresh intermediate water mass is exported southward into the DWBC, the NAC, and the interior abyssal Atlantic, as discussed previously. Variability

in LSW production on yearly timescales is correlated with the strength of the deep convection and the depth of the mixed layer. On longer timescales, variability is not as well understood; Yashayaev and Loder (2016) postulate that intermittent pentadal-to-decadal-scale deep convection is masking long-term trends. As previously discussed, in the context of the wider climate, such trends might have relevance for variability in the AMOC (e.g., Yeager et al., 2021; Lozier, 2023) as well as for the injection of CO_2 and oxygen into the interior Atlantic (Rhein et al., 2017).

Before continuing the discussion on deep convection in the LS, it is useful to define stratification using the Brunt-Väisälä frequency, N. First, we must define buoyancy, b, as

$$b = -g\left(\frac{\rho - \rho_0}{\rho_0}\right), \tag{1.2}$$

where g is gravity and ρ_0 is a constant reference density (e.g., 1,000 kg m^{-3}). We can then define the stability of a water column using

$$N^2 = \partial b/\partial z. \tag{1.3}$$

When $N^2 > 0$, the water column is stable; when $N^2 < 0$, convective overturning occurs (Marshall & Schott, 1999). Figure 1.4 shows profiles from an ocean General Circulation Model (OGCM) midway along the same section as in Figure 1.3. Here, when $N^2 = 0$, density is homogenous within two or more vertically stacked grid points, and when $N^2 < 0$, convective overturning is occurring. During preconditioning (panel b), density is seen to increase slowly with depth compared to the stable case (panel a), and negative N^2 values are found in the still-shallow mixed layer. This implies that stratification is breaking and convection is forming. During active deep convection (panel c), density is homogenized or decreasing with depth throughout the upper 1,100 m, and N^2 values in this layer of 0 or < 0 imply that the water column is mixing downwards.

Stratification, and hence deep convection, can be controlled by fluxes of both heat and salinity. As discussed in Section 1.3, these fluxes can come laterally from the boundary currents. However, we must also consider fluxes at the surface, including sensible and latent heat fluxes as well as precipitation minus evaporation. These fluxes control surface buoyancy according to the expression

$$\mathscr{B} = \frac{g}{\rho_0}\left(\frac{\alpha}{c_w}\mathscr{H} + \rho_0\beta S(E - P)\right), \tag{1.4}$$

where α and β are the non-linear thermal and haline expansion coefficients, c_w is the heat

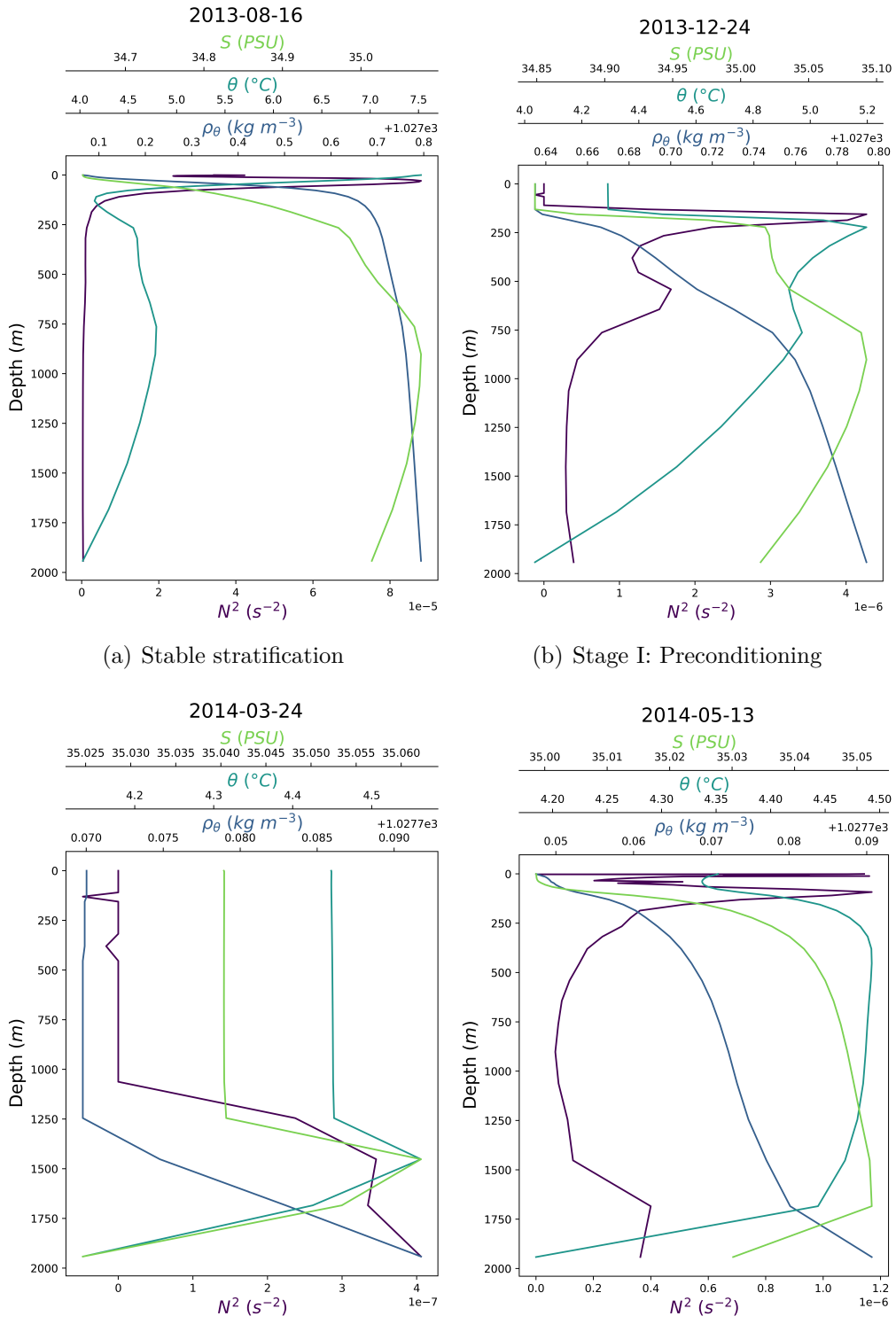

(a) Stable stratification

(b) Stage I: Preconditioning

(c) Stage II: Deep convection

(d) Stage III: Lateral exchange

Figure 1.4: Profiles of potential temperature (θ), salinity (S), potential density (ρ_θ), and the square of the Brunt-Väisälä frequency (N^2) during the three stages of deep convection. All panels are 5-day averages from midway along the AR7W section, produced using the same model and dates as in Figure 1.3.

capacity of water, $\mathscr{H}$ is the surface heat loss, and $(E - P)$ is the freshwater flux due to evaporation minus precipitation (Marshall & Schott, 1999). In the LS, both the α term and the β term are non-negligible. It is therefore considered a transition region between the primarily heat-stratified (i.e., $N^2 = g\alpha\partial T/\partial z > 0$) 'alpha ocean' subtropics and the primarily salt-stratified (i.e., $N^2 = g\beta\partial S/\partial z > 0$) 'beta ocean' Arctic (Carmack, 2007).

In practice, within the LS, the buoyancy effects of surface heat losses are much stronger than the salinity effects of $E - P$ (Lab Sea Group, 1998). The same cannot be said of buoyancy fluxes between the boundary currents and interior, where the exchange of both heat and freshwater play important roles controlling deep convection. This is because, as discussed in Section 1.3, fluxes from the WGC and LC inject both heat and freshwater into the north and west LS. Within Figure 1.4, the effects of both salinity and heat on stratification are clearly visible, where changes within the water column of salinity (green) and temperature (teal) both control the density (dark blue).

1.5 Tidal modelling

Tides are periodic oscillations in sea level arising from the rotation of the Earth and the gravitational forces of the Sun, Moon, and less significantly from other planets and energy sources (Griffiths & Hill, 2015). In the open ocean, the tidal surface amplitude is usually around 50 cm; resonance with coastal bathymetry can significantly amplify this figure, such as in the Bay of Fundy (Griffiths & Hill, 2015), where the tidal amplitude exceeds 6 m (Karsten et al., 2008). In the open ocean, tides are particularly important as a source of mechanical energy driving deep mixing, and without tides the large-scale overturning circulation would cease after a few thousand years (Munk & Wunsch, 1998). In coastal regions, tides create challenges for infrastructure projects and economic activities due to the extreme fluxes of mass, momentum, and energy that can be driven by tidal sea level oscillations (Griffiths & Hill, 2015).

Numerical modelling is often used in modern tidal research, although the modelling approach taken depends on the question(s) being investigated. Much of the ongoing research is devoted to coastal areas and the practical implications of barotropic tides on sea surface heights and currents (e.g., Furner et al., 2016; Lyard et al., 2021). Other research is devoted to the relationship between barotropic tides, internal tides (that is, tidally-generated internal gravity waves existing within the stratified ocean), deep mixing, and the overturning circulation (e.g., Munk & Wunsch, 1998; Assene et al., 2023 and Megann, 2024). The latter, which requires the use of OGCMs, is my principal focus below.

Harmonic analysis shows that tides consist of constituent waves with distinct frequencies, determined by the orbital geometry of the associated celestial bodies. The most energetic of these constituents are directly astronomically forced, while others are so-called 'over-tides' generated by non-linear interactions within the ocean. The strongest directly forced tidal constituents are given in Table 1.1. The principal lunar tide, $M2$, is the largest constituent by global energy of the oceanic response. It is also the largest tide in the Atlantic in terms of the sea surface amplitude. With a period of 12.42 h, or half of a lunar day, it is a so-called 'semi-diurnal' tide, and its dominance in the Atlantic is thought to result from the Atlantic Basin having a normal mode close to semi-diurnal. Additional semi-diurnal lunar and solar tides include $S2$, $N2$, and $K2$. Diurnal (daily) solar and lunar tides include $K1$, $O1$, $P1$, and $Q1$. The largest tide in most of the Pacific is $K1$ (Griffiths & Hill, 2015).

Table 1.1: Some of the most energetic directly forced tidal constituents, based on Table 29.1 from Griffiths and Hill (2015). Forcing amplitudes are used in Equation 1.5 and are taken from Cartwright (1977). Energies are taken from Egbert and Ray (2003) and are based on their TPXO.5 assimilative solution.

Tidal constituent	Period (h)	Energy (PJ)	Amplitude (cm)
$M2$	12.42	312.26	16.98
$K1$	23.93	49.92	10.51
$S2$	12.00	49.87	7.90
$O1$	25.82	24.87	7.07
$N2$	12.66	14.11	3.25
$P1$	24.07	4.78	3.34
$K2$	11.97	4.06	2.15
$Q1$	26.87	1.16	1.35
...			

The equilibrium tide, h_{eq}, accounting for the idealized response of the ocean and the elastic Earth to N directly-forced astronomical constituents, is approximated by

$$h_{eq} = Re\left(\sum_{j=1}^{N} \hat{h}_{eq,j} e^{-i\omega_j t}\right), \tag{1.5}$$

where θ is latitude, ϕ is longitude, and A_j is given by Table 1.1. For semi-diurnal tides, $\hat{h}_{eq,j} = A_j \cos^2\theta e^{-2i\phi}$, and for diurnal tides, $\hat{h}_{eq,j} = A_j \sin 2\theta e^{-i\phi}$. Within global OGCMs, barotropic tidal forcing is achieved by including the equilibrium tide in the momentum equation. A second term can also be included, termed the 'self-attraction and loading potential' (SAL), h_{sal}. The general mathematical expressions for these terms are out of scope for this thesis.

SAL accounts for the following three additional effects: First, changes in the distribution of water masses results in deformations in the seafloor, thereby affecting sea surface level;

second, there is an increase in the gravitational field towards built-up water masses; and third, there is an altered gravitational field from changes in the seafloor, away from depressions and towards protrusions (Stepanov & Hughes, 2004; Arbic, 2022).

In most OGCMs, a third consideration is energy loss from 'drag', $\mathbf{D}$, which captures losses both to the turbulent bottom boundary layer and those related to 'baroclinic conversion' (Griffiths & Hill, 2015). In the Nucleus for European Modelling of the Ocean (NEMO) framework, these effects can be captured using an increased vertical diffusivity, which is a function of the Brunt-Väisälä frequency, the tidal dissipation efficiency (a constant), the mixing efficiency (also a constant), a simple vertical structure function, and a function of the energy transfer due to baroclinic conversion, $E(x, y)$ (Madec et al., 2017).

Baroclinic conversion occurs when tides, which are initially barotropic, break over rough topography and generate baroclinic internal tides. This dissipates a fraction of the tidal energy by conversion into successively smaller scales (Arbic, 2022; Madec et al., 2017). In NEMO, $E(x, y)$ can be taken from a pre-computed wave energy map, which is intended to capture barotropic momentum exchange to internal tides that occurs on scales too small to be captured by the model resolution.

The importance of internal tides on circulation is highlighted by Munk and Wunsch (1998): There are only two possible sources of energy for deep mixing, tides and wind, which is necessary to maintain stratification against the upwelling and deep water formation associated with the large-scale overturning circulation. Munk and Wunsch (1998) and Garrett and Kunze (2007) estimate that the total rate of tidal energy dissipation is 3.7 TW, with roughly 30% of this available for abyssal mixing. The rest is lost to the turbulent bottom boundary layer.

Internal tide generation, and hence barotropic-baroclinic tidal energy flux, is complex and depends on many variables. These include the frequency of the barotropic tide and the associated horizontal currents, the local topography and water depth, the local stratification, and the latitude (Garrett & Kunze, 2007). Some internal tides cascade to turbulence rapidly and dissipate their energy locally, particularly those generated by small-scale features. They are characterized by high vertical modes, with short horizontal scales and more vertical structure. Low vertical modes are generated by larger features like the Hawaiian islands, and they can propagate for thousands of kilometres. Eventually, low mode internal tides break and enhance mixing within the distant abyssal ocean (Arbic, 2022).

Low mode internal tides have horizontal scales of 50–90 km (Megann, 2024), meaning that they can be captured by OGCMs with adequately high resolutions, approximately 1/10° or finer (Arbic, 2022). One such model, a high resolution global implementation of the HYCOM

(HYbrid Coordinate Ocean Model) framework, yielded vertically-averaged dissipation rates similar to those from ARGO float observations (Arbic, 2022). Similarly, Assene et al. (2023) used a 1/36° regional NEMO model to study internal tides offshore of the Amazon River. At this resolution, which yields a horizontal grid spacing of approximately 3.1 km, the low mode internal tides are explicitly resolved. Compared to satellite observations, simulations with tidal forcing were found to produce better sea surface temperatures than those without.

This is a young area of research, and the high resolutions demanded of tidal OGCMs mean they are very expensive to run for global simulations. Assene et al. (2023) therefore use a regional domain, spanning roughly 15–20° of latitude and longitude. This highlights an important limitation of such a model; generally, horizontal boundary forcing includes only the barotropic tide. Hence, remotely-generated low mode internal tides are unrepresented, and larger regional domains are therefore recommended in order to capture increased tidal kinetic energy (Arbic, 2022).

Megann (2024) compared a 1/4° resolution global NEMO model with a tidal atlas and found that it represented the barotropic tide with acceptable realism. Conversely, amplitudes of the $M2$ internal tides were only 30–50% that of a 1/12° HYCOM simulation, likely because the grid points were too far apart to capture the shorter end of the mode-1 internal tides. However, the long distance propagation of these internal tides was realistic, and despite the reduced internal tide energy, stratification in the thermocline was reduced by 10–20% throughout most of the global ocean. This led to reductions in the AMOC and generally improved realism based on temperatures from a climatology.

1.6 Submesoscale Mixed Layer Eddies

The mixed layer contains baroclinic instabilities at horizontal density fronts characterized by fast growth rates of O(1/day) and small scales of O(1 km) (Fox-Kemper & Ferrari, 2008). These instabilities play an important role in restratifying the upper ocean following convective mixing by slumping isopycnals from the vertical to the horizontal.

In OGCMs, this process of dynamical restratification tends to be omitted because most model resolutions cannot directly represent O(1 km) instabilities. Rather, mixed layer restratification is driven mainly by surface heating, which leads to a bias towards weak surface stratification (Fox-Kemper et al., 2008).

Beginning in 2008, Fox-Kemper and others published three papers on this topic. Fox-Kemper et al. (2008) proposed a streamfunction that captures the bulk of the restratification

from finite-amplitude submesoscale mixed layer eddies (SMLEs), which are responsible for most of the dynamical restratification. It does this by tilting steep isopycnals from the vertical to the horizontal, thereby adiabatically overturning strong fronts. Fox-Kemper and Ferrari (2008) propose a parameterization for OGCMs, $\boldsymbol{\Psi}$, based on this streamfunction, and they compare it favourably to very-high resolution Large Eddy Simulations (LES). Fox-Kemper et al. (2011) discuss the implementation of this parameterization within three global OGCMs.

In its OGCM parameterization form, the streamfunction is

$$\boldsymbol{\Psi} = C_e \frac{\Delta s}{L_f} \frac{H^2 \nabla \overline{b}^z \times \hat{\boldsymbol{z}}}{\sqrt{f^2 + \tau^{-2}}} \mu \left(\frac{z}{H} \right), \tag{1.6}$$

where terms are as follows: C_e is an efficiency factor, determined by LES to be between 0.06 and 0.08; Δs is the horizontal grid spacing; H is the mixed layer depth; $\nabla \overline{b}^z$ is the horizontal buoyancy gradient averaged over the mixed layer; $\hat{\boldsymbol{z}}$ is an upward pointing unit vector; f is the Coriolis parameter; and z is depth. Three additional terms are discussed below.

The frontal width parameter, L_f, represents the smallest width of the unresolved fronts within each grid cell. Hence, $\Delta s / L_f$ is meant to account for the sharp buoyancy gradients that remain uncaptured due to aliasing from coarse resolutions (Bodner et al., 2023). It can be represented by

$$L_f = \max \left\{ \frac{NH}{\sqrt{f^2 + \tau^{-2}}}, L_{f_{\min}} \right\}. \tag{1.7}$$

$L_{f_{\min}}$ is used to guard against numerical instabilities. Its most common value, $L_{f_{\min}} = 5$ km, results in conservative behaviour from the parameterization. It has been argued that this value can be omitted under careful numerical implementation, thereby yielding improved MLD representation (Calvert et al., 2020). More generally, L_f is considered a tuneable parameter, with Equation 1.7 chosen because there is no compelling alternative (Fox-Kemper et al., 2011; Calvert et al., 2020). A recent publication by Bodner et al. (2023) suggests a new scaling based on the 'turbulent thermal wind balance', however this is not widely implemented.

The mixing time scale, τ, represents the time needed to mix momentum across the mixed layer, and it is typically taken to be within 1–10 days (Fox-Kemper et al., 2011). It is used to prevent a singularity in the streamfunction at the equator (where, without τ, the denominator f goes to zero), although it has recently been argued that boundary layer turbulence varies widely and so a fixed value of τ is not justified (Bodner et al., 2023).

Finally, a vertical structure function, $\mu(z/H)$, is given by

$$\mu\left(\frac{z}{H}\right) = \max\left\{0, \left[1 - \left(\frac{2z}{H} + 1\right)^2\right]\left[1 + \frac{5}{21}\left(\frac{2z}{H} + 1\right)^2\right]\right\}. \tag{1.8}$$

Equation 1.8 is normalized to one and set to zero below the base of the mixed layer. All remaining constants are thereby collected into the efficiency factor, C_e.

Despite the two issues highlighted above, namely regarding the justifications for L_f and τ, the parameterization has been shown to improve MLDs. Fox-Kemper et al. (2011) evaluated its effects within three global OGCMs and found that it shoals MLDs and reduces deep biases in coarse resolution models, with the largest effect in polar regions. A secondary impact was a strengthening of the AMOC, along with reductions in its variability. Similarly, Calvert et al. (2020) evaluated its effects within a suite of OGCMs of varying resolutions, and they generally found a reduction in global deep MLD biases compared to climatological values. I am aware of no other publications that explicitly evaluate the parameterization.

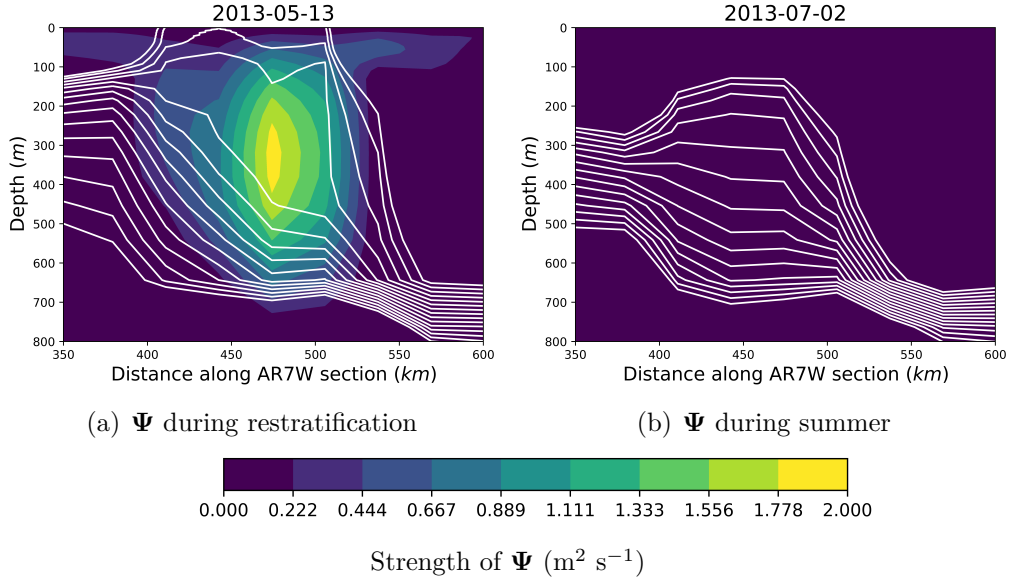

(a) $\mathbf{\Psi}$ during restratification (b) $\mathbf{\Psi}$ during summer

Figure 1.5: Strength of the submesoscale mixed layer eddy streamfunction, $\mathbf{\Psi}$. White lines denote isopycnals of potential density between 1,027.71–1,027.73 kg m^{-3}. **(a)** The parameterization when the mixed layer is deep and isopycnals are steep. **(b)** The parameterization when the stratification is more stable. The colour bar denotes the scalar strength of the streamfunction with units of m^2 s^{-1}. Sections are from a 1/4° ocean General Circulation Model.

The parameterization works by producing fluxes, $\overline{\mathbf{u}'b'}$, and a three-dimensional eddy-induced velocity, $\mathbf{u}^*$, which can both be expressed as follows:

$$\overline{\mathbf{u}'b'} \equiv \mathbf{\Psi} \times \nabla\bar{b}, \quad \mathbf{u}^* = \nabla \times \mathbf{\Psi}. \tag{1.9}$$

Velocities (i.e., $\mathbf{u}^*$) are used to advect density and other tracers. The intended result is to produce reliable vertical fluxes (i.e., $\overline{w'b'}$), where light water is transported upward and towards the dense side of mesoscale fronts and vice versa for dense water (Calvert et al., 2020; Bodner et al., 2023). This vertical buoyancy flux releases available potential energy stored in the front. Horizontal fluxes and any residual fluxes that are not captured by the parameterization are smaller and dominated by mesoscale eddies over large distances.

The parameterization is illustrated in Figure 1.5, which shows a section across the Labrador Sea within a 1/4° OGCM that has the parameterization activated. From Equation 1.6, $\mathbf{\Psi}$ is proportional to the product of the horizontal buoyancy gradient, the mixed layer depth, and the inertial period, leading to faster restratification when fronts are strong and the mixed layer is deep. This is expected, because SMLEs cluster along fronts, where frontal vertical shear allows them to grow rapidly. Elsewhere, growth rates are too slow to compete with damping from turbulent mixing. In deep convection, strong horizontal buoyancy gradients and deep mixed layers result in strong SMLE restratification. However, during active convection, SMLE effects are secondary and do not prevent destratification. Rather, they immediately initiate restratification when convection ceases. Panel (a) in Figure 1.5 shows steeply sloped isopycnals while the mixed layer is relatively deep. The colour indicates the strength of the parameterization, and it is strongest in the vicinity of weak stratification. Panel (b) shows the same section and density range of isopycnals several months later, and $\mathbf{\Psi}$ is approximately 0.

1.7 Research question

Global coupled climate models, such as those used in the IPCC's CMIP6, commonly have resolutions of 1/4° or coarser (Hewitt et al., 2020). This means, if they are forced by the astronomical tidal potential, that they might have the ability to capture the barotropic tide while marginally representing the lowest mode internal tides. Conversely, they cannot directly represent submesoscale mixing.

As discussed in Sections 1.5 and 1.6, recent research has indicated that tidal forcing and the SMLE parameterization (SMLEp) can both improve the representation of mixed layers in OGCMs relative to observations. Our goal is to extend this research by investigating their effects on deep convection in the Labrador Sea using a 1/4° OGCM. Whether they improve MLDs will dictate if we recommend their inclusion within future global coupled climate models, which commonly experience deep MLD biases (Rackow et al., 2019; Hewitt et al., 2020). We thereby hope, ultimately and minutely, to contribute to the community

effort towards improving the accuracy of climate models and their predictions of the AMOC slowdown, sea level rise, ice loss, and more.

Chapter 2

Model description

OGCMs are indispensable tools for understanding the structure of currents, water mass displacements, and the distributions of physical and chemical properties. When integrated into the future they can provide important predictions of how the climate will change. When integrated over historical periods they can provide better understandings of the distant past, they can compensate for temporally and spatially incomplete observations, or they can be compared with climate records to validate their accuracy.

Most modern OGCMs are based on equations first described during the 1960s (e.g., Bryan, 1969; Manabe & Bryan, 1969). These are, briefly, the momentum and continuity equations with the hydrostatic and Boussinesq assumptions and a simple equation of state (Stewart, 2003). Together, these are termed the primitive equations, and many modern OGCMs can be considered primitive equation models. Examples of OGCMs include NEMO (Madec et al., 2022), MOM (Modular Ocean Model; Griffies et al., 2012), FESOM (Finite-Element/volumE Sea ice-Ocean Model; Wang et al., 2014), and MITgcm (Massachusetts Institute of Technology general circulation model; Adcroft et al., 2018).

However, it is crucial to note that many modern modelling frameworks differ in some way from each other, utilizing a range of different discretization methods, coordinate systems, and assumptions (sometimes deviating from the original primitive equation recipe). Examples include MITgcm permitting non-hydrostatic simulations (Adcroft et al., 2018) and FESOM using unstructured meshes (Wang et al., 2014). One noteworthy benefit of the existence of such a range of models is that it permits the calculation of mean results from multi-model ensembles, which are thought to provide 'best estimate' climate projections with minimized model error. This methodology has long been used by the IPCC, and it is the basis for the CMIP.

In this study, we use ANHA4 (Arctic Northern Hemisphere Atlantic 1/4°), a regional configuration of NEMO version 3.6 implemented on Graham, a supercomputer under the purview of the Digital Research Alliance of Canada. Formally, NEMO is a framework of ocean-related engines based around OPA (Océan PArallélisé), a primitive equation ocean model whose development began during the 1980s (Madec et al., 1997). In addition to OPA, which handles ocean dynamics and thermodynamics, NEMO version 3.6 typically also employs the Louvain-la-Neuve (LIM) engine for sea ice dynamics and thermodynamics as well as the Tracer in the Ocean Paradigm (TOP) engine for passive tracers and biogeochemistry.

In this chapter, I will discuss ocean General Circulation Modelling with a special focus on NEMO and ANHA4. First, I will introduce the governing equations and assumptions that are fundamental to NEMO's architecture. I will then provide a short overview of three key ocean modelling concepts: Boundary conditions, time and space discretization, and parameterizations. Finally, I will discuss the specifics of ANHA4 and the six simulations used in our research.

2.1 Governing equations and assumptions

The NEMO model is governed by the momentum and continuity equations plus a non-linear equation of state, which couples temperature and salinity to velocity (Madec et al., 2017). An orthogonal set of unit vectors $(\mathbf{i}, \mathbf{j}, \mathbf{k})$ are defined so that $\mathbf{k}$ is pointing upwards and $(\mathbf{i}, \mathbf{j})$ are tangent to geopotential surfaces.

The momentum equation describes the conservation of momentum. It is, in the horizontal,

$$\frac{\partial \mathbf{U}_h}{\partial t} = -\left[(\nabla \times \mathbf{U}) \times \mathbf{U} + \frac{1}{2}\nabla(\mathbf{U}^2)\right]_h - f\mathbf{k} \times \mathbf{U}_h - \frac{1}{\rho_0}\nabla_h p + \mathbf{D}^{\mathbf{U}} + \mathbf{F}^{\mathbf{U}}, \tag{2.1}$$

where variables are defined as follows: The subscript h denotes a horizontal vector within the $(\mathbf{i}, \mathbf{j})$ plane; $\mathbf{U}$ is velocity, with components (u, v, w) corresponding to the $(\mathbf{i}, \mathbf{j}, \mathbf{k})$ directions such that $\mathbf{U} = \mathbf{U}_h + w\mathbf{k}$; t is time; f is the Coriolis parameter; p is pressure; ∇ is the generalized derivative vector operator in $(\mathbf{i}, \mathbf{j}, \mathbf{k})$; ρ is density (and hence ρ_0 is a reference density); and the terms $\mathbf{D}^{\mathbf{U}}$ and $\mathbf{F}^{\mathbf{U}}$ capture parameterizations of the small scale physics and surface forcing, respectively. In other words, Equation 2.1 relates velocities to the Coriolis force, pressure gradients, small scale physics, and surface forcing.

In the vertical, the hydrostatic approximation is invoked to reduce the momentum equa-

tion to a balance of pressure and gravity, g. It can be expressed as

$$\frac{\partial p}{\partial z} = -\rho g. \tag{2.2}$$

Conservation of mass is expressed using the continuity equation for an incompressible fluid, i.e.,

$$\nabla \cdot \mathbf{U} = 0. \tag{2.3}$$

Potential temperature (T) and salinity (S) are governed by

$$\frac{\partial T}{\partial t} = -\nabla \cdot (T\mathbf{U}) + D^T + F^T \tag{2.4a}$$

$$\frac{\partial S}{\partial t} = -\nabla \cdot (S\mathbf{U}) + D^S + F^S, \tag{2.4b}$$

where D^T, F^T, D^S, and F^S are terms representing the small scale physics (D) and surface forcing (F).

Lastly, density is governed by a non-linear equation of state. It is a function of potential temperature, salinity, and pressure, i.e.,

$$\rho = \rho\left(\theta, S, p\right). \tag{2.5}$$

These equations are subject to a series of assumptions that generally improve computational costs while sacrificing minimal accuracy. The two classical assumptions that are associated with the original primitive equation recipe are:

1. *The Boussinesq approximation:* Variations in density are neglected except when contributing to buoyancy, which has the effect of conserving volume but not mass. This explains the use of ρ_0 in Equation 2.1 whereas ρ is used in Equation 2.2.
2. *The hydrostatic approximation:* The momentum equation is reduced in the vertical to a balance of the pressure gradient and buoyancy, which explains the brevity of Equation 2.2. This requires that convective processes are parameterized, which is discussed further in Section 2.4.3.

Four additional assumptions are as follows:

3. *The spherical Earth approximation:* Geopotential surfaces are taken to be spherical, with gravity parallel to the Earth's radius.
4. *The thin-shell approximation:* Compared to the Earth's radius, ocean depth is neglected. The Earth's radius is approximately 1,800 times the ocean's mean depth

(Stewart, 2003), which justifies this approximation. Together with the spherical Earth approximation, this permits gravity to be assumed constant.

5. *The turbulent closure hypothesis:* Turbulent fluxes (i.e., the effects of small scales on large scales) are expressed in terms of large-scale features.
6. *The incompressibility hypothesis:* Water is assumed to be incompressible such that the three-dimensional divergence of the velocity vector is assumed to be zero. This explains why the continuity equation (Equation 2.3) has no density term.

2.2 Boundary conditions

The ocean component of NEMO is in contact with the atmosphere, land, and ice, and experiences exchanges of salinity, heat, and/or momentum across these boundaries. A reference datum is defined as $z = 0$ m, corresponding to the mean of the sea surface, and permits the definition of the lower and upper boundary of the ocean as

$$z_{\text{bottom}} = -H_B(i, j)$$
$$z_{\text{surface}} = \eta(i, j, k, t),$$

where H_B is the depth of the ocean and η is the sea surface relative to $z = 0$ (Madec et al., 2017).

ANHA4 is atmospherically forced, meaning that atmosphere-ocean surface fluxes are estimated using traditional bulk formulae modulated by the state of the near-surface atmosphere. Six parameters are needed for these calculations: Wind stresses in the u and v directions ($\tau_{u,v}$), which are interpolated onto the model grid and applied to the computation of surface mixing; non-solar heat flux (Q_{ns}), which accounts for non-penetrative sensible, latent, and long wave (terrestrial) heat fluxes, and which is applied to the uppermost model level; solar heat flux (Q_{sr}), which accounts for penetrative heat fluxes and which is applied more deeply than only the uppermost model level; and freshwater flux, which accounts for evaporation minus precipitation ($E - P$) (Madec et al., 2017).

The above heat fluxes, Q_{ns} and Q_{sr}, along with additional heat fluxes between the ocean and sea ice, are applied in Equation 2.4a as part of F^T. Optionally, F^T can also represent heat fluxes due to geothermal heating, river runoff, and glacial melt, although these terms are not included in our model. Analogously, F^S in Equation 2.4b accounts for $E - P$ as well as salt and freshwater exchange with sea ice. Runoff from rivers and glacial melt, which is considered pure freshwater with $S = 0$, is also very important in controlling F^S, and can be

specified using runoff datasets. However, unlike most ocean-atmosphere and ocean-sea ice exchange, runoff inputs are not simply added to the uppermost model level; rather, they are spread across multiple horizontal and vertical grid cells.

An additional consideration pertaining to freshwater fluxes is their effect on the ocean's volume; in NEMO, η can vary due to $E - P$, river runoff, and sea ice freezing/melting. Similarly, boundary conditions can also affect mixing dynamics. In the horizontal momentum equation (Equation 2.1), this is represented by $\mathbf{D}^{\mathbf{U}}$, and it variously captures momentum transfer from sea ice, surface winds, and river runoff. At the ocean-land interface, momentum is also constrained since flow cannot cross the boundary, and it is further modulated by turbulence from friction within the bottom boundary layer.

2.2.1 Tidal forcing

Tidal boundary forcing is an additional option in NEMO, and its effects are a central focus of this thesis. In NEMO version 3.6, 19 constituent waves may be included in the forcing module. In more recent NEMO releases, this number has been increased to 34 (Madec et al., 2022). Different authors utilize different sets of constituents in their NEMO models: Furner et al. (2016) recommend 14 and Assene et al. (2023) use 15. Conversely, Paquin et al. (2020) and Megann (2024) use only 5. Paquin et al. (2020) note that a 9-constituent simulation would require a nearly eightfold increase in runtime compared to their 5-constituent simulations. The question of how many constituents to include in a model must therefore be answered with care.

Tidal forcing is applied in two ways. The first, so-called 'surface tidal forcing', is achieved using additional barotropic (i.e., depth invariant) terms in the momentum equation. These terms are based on the equilibrium tide, sometimes called the 'tidal potential' (Π_{eq}), as well as optionally the self attraction and loading potential (Π_{sal}). Calculation of the latter is computationally expensive and, in the tidally-forced ANHA4 runs used in this study, it is read from an external dataset.

Conversely, the equilibrium tide is calculated based on three types of constituent waves: Semi-diurnal, diurnal, and long-period. Their potentials are

$$\Pi_{eq,\text{semi-diurnal}} = A_j \left(\cos^2\phi\right) \cos\left(\omega_j t + 2\lambda + V_{0j}\right) \tag{2.6a}$$

$$\Pi_{eq,\text{diurnal}} = A_j \left(\sin 2\phi\right) \cos\left(\omega_j t + \lambda + V_{0j}\right) \tag{2.6b}$$

$$\Pi_{eq,\text{long period}} = A_j \left(\frac{1}{2} - \frac{3}{2}\sin^2\phi\right) \cos\left(\omega_j t + V_{0j}\right) \tag{2.6c}$$

where A_j is the amplitude of the wave j, ω_j is the angular frequency of the wave j, V_{0j} is the astronomical phase of the wave j relative to Greenwich, and ϕ and λ are latitude and longitude, respectively (Madec et al., 2017).

The additional barotropic force is then included within $\mathbf{F}^{\mathbf{U}}$ in the horizontal momentum equation (Equation 2.1) based on

$$\frac{\partial \mathbf{U}_h}{\partial t} = ... + g\nabla\left(\gamma \Pi_{eq} + \Pi_{sal}\right) \tag{2.7}$$

where γ is a constant 'tidal tilt factor', normally taken to be $\gamma = 0.7$, based on the Love numbers k and h (Madec et al., 2022).

The second way tidal forcing is applied is through 'tidal harmonic forcing' at lateral boundaries. This is important in non-global simulations, such as ANHA4. Tidal harmonic forcing is only available when surface forcing is already activated, in which case complex harmonic forcing data are read from an external dataset. These data are, specifically, the complex harmonic amplitudes of sea surface height as well as the u and v components of the barotropic tide, all of which are pre-defined on the model grid. The same set of user-specified constituents as employed in surface tidal forcing are used here (Madec et al., 2022).

2.3 Time and space discretization

For the time discretization of non-diffusive processes, NEMO uses the time-centred leapfrog scheme, therefore being applied to momentum and tracer advection, pressure gradient, and Coriolis terms. However, diffusive processes are discretized by either forward or backward differencing schemes (Madec et al., 2017).

Generally, time differencing in NEMO can be expressed as

$$x^{t+\Delta t} = x^{t-\Delta t} + 2\Delta t \mathrm{RHS}_x^{t-\Delta t, t, t+\Delta t} \tag{2.8}$$

where variables are as follows: x represents u, v, T, or S; RHS is the right-hand side of a time-dependent equation; and Δt is the time step. For diffusive processes, a forward or backward time differencing scheme is used. In this case, the RHS is evaluated either at time step $t - \Delta t$ or at $t + \Delta t$; the choice depends on the desired balance of accuracy and expense (Madec et al., 2022).

If the RHS of Equation 2.8 is evaluated at time step t, it represents the leapfrog scheme. This is a common approach for numerical analysis of advection processes in low-viscosity

fluids, in theory achieving second-order accuracy (Madec et al., 2017). However, it permits the coexistence of a physical and a computational mode, leading to divergence of odd and even time steps and thus large phase error. This problem is amended by using a Robert-Asselin time filter, which re-couples the diverging solutions and dampens the computational mode. This has the effect of reducing accuracy to first order. However, the second order error is small, so it is considered a quasi-second order accurate scheme (Leclair & Madec, 2009; Madec et al., 2017).

The size of the time step, Δt, is coupled with the size of the spatial step, Δx, in the determination of numerical stability. Consider a general case in which the barotropic tide is modelled using a depth-averaged tidal model with a horizontal resolution of 1/4°. In high latitudes, this yields a minimum spacing of approximately $\Delta x = 4$ km. Taking a barotropic wave speed in the deep ocean to be approximately 200 m s^{-1}, then the Courant-Friedrichs-Lewy condition can be used as follows to identify the maximum time step:

$$\begin{aligned} c\Delta t/\Delta x \leq 1 \rightarrow \Delta t &\leq \Delta x/c \\ &\leq 4{,}000/200 \\ &\leq 20 \text{ s}, \end{aligned}$$

hence, a time step of 20 s is required to ensure stability (Griffiths & Hill, 2015). In ANHA4, the barotropic time step is 6 s, thereby easily capturing this kind of tidal wave.

NEMO employs the Arakawa C-grid for spatial discretization. In this configuration, cells are centred around scalar points (T, S, p, ρ), with vector points (u, v, w) defined on the cells' faces. This is illustrated in Figure 2.1. At the North Pole, convergence of meridians is avoided by using a tripolar grid, where singularities are placed in Canada and Russia rather than in the ocean (Madec et al., 2022).

In the vertical, ANHA4 uses the popular z^*-coordinate system. In this case, a non-linear free surface is assumed. In a traditional z-coordinate system, where levels are based on geopotentials, undulations in the free surface are concentrated at the surface level. Conversely, in the z^* system, they are distributed equally over the water column. Hence, the vertical discretization, δz^*, is scaled by a factor, r, according to

$$\delta z^* = \delta z / r \quad \text{with} \quad r = \frac{H_B + \eta}{H_B}, \tag{2.9}$$

where variables are as follows: $z^* = 0$ and $z^* = -H_B$ denote the upper and lower boundary, respectively; δ denotes a vertical discretization; and η denotes the sea surface height (Madec et al., 2022). In recent NEMO releases, the z^* system is the default vertical coordinate.

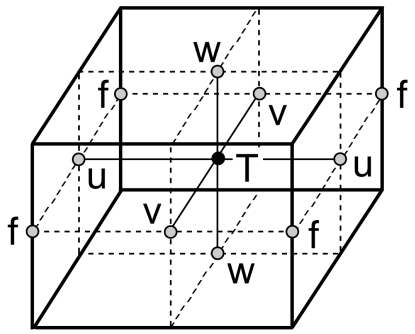

Figure 2.1: Variables on the NEMO model grid. T indicates where scalar values are defined, such as temperature, salinity, density, and pressure. u, v, and w indicate where velocities are defined. f is where vorticity is defined. Adapted from (Madec et al., 2017).

Alternative coordinate systems include terrain-following coordinates, isopycnal coordinates, and combined systems. Megann (2024) evaluate the performance of several tidally-forced 1/4° resolution NEMO models with different coordinate systems. They found that, while tidal forcing with the z^*-coordinate system improved realism, the presence of internal tides led to spurious diapycnal mixing. And, by switching to a combined-type coordinate system ($\tilde{z}$-coordinates), spurious mixing was reduced and realism was further improved.

2.4 Parameterizations

Parameterizations are used to represent complex processes that are in some way out of the scope of a model. Mostly, this refers to processes that are too small to be realistically captured on the model grid. In the horizontal momentum equation (Equation 2.1), such motions are represented by $\mathbf{D}^{\mathbf{U}}$. Analogous terms are used for tracer parameterizations, represented by the terms D^T and D^S in Equations 2.4a and 2.4b, respectively.

A prototypical type of OGCM parameterization is for turbulent vertical mixing. In NEMO, vertical eddy viscosity and diffusivity coefficients can be constants, or functions of the local Richardson number (which measures the ratio of buoyancy to flow shear), or a turbulent closure model. Other examples of parameterizations include bulk formulae, used in the calculation of atmospheric fluxes, and Love numbers, used in the calculation of tidal surface forcing (Madec et al., 2017).

There are a large number of parameterizations that can or must be configured within NEMO. Three parameterized processes with particular relevance to this thesis are related to

convection, tidal mixing, and SMLEs. They are briefly discussed below.

2.4.1 Convection

When static instabilities occur in nature (i.e., when dense water is overlying less-dense water), convective mixing re-establishes stability. This cannot occur in NEMO due to the hydrostatic approximation, and some combination of parameterizations is therefore necessary. In ANHA4, the 'enhanced vertical diffusion' parameterization is employed. In this case, large vertical eddy mixing coefficients are assigned wherever stratification is unstable (Madec et al., 2017). This is optionally done to both tracers and momentum, as in ANHA4, or to tracers only.

Alternatively, 'non-penetrative convective adjustment' can be used. In this case, the two topmost statically unstable cells in a water column are identified. Potential temperatures and salinities are then mixed, conserving heat and salt contents. Next, the resultant density is estimated using a linear equation of state, and if density is still greater than the next deepest cell, the process is repeated. This occurs until static stability is re-established. One issue with this algorithm is its temporary use of a linear equation of state, which cannot capture the effects of cabbeling or thermobaricity. This can lead to inaccuracies persisting for multiple time steps. It is also more time-consuming than the enhanced vertical diffusion scheme. And additionally, its use of potential density referenced to the sea surface can yield errors for realistic ocean simulations, in which some actually-stable columns are erroneously deemed unstable and subsequently mixed (Madec et al., 2017).

2.4.2 Tidal mixing

Tidal mixing is a separate concept from tidal forcing (Section 2.2.1), and it refers to tidally-enhanced subgrid-scale mixing. In NEMO, there are two parameterizations associated with tidal mixing.

The first is 'bottom intensified tidal mixing', which is intended to capture the effect of internal tides breaking (Madec et al., 2017). It works via an enhanced vertical diffusivity, and has already been briefly discussed in Section 1.5. It is a function of the Brunt-Väisälä frequency, the tidal dissipation efficiency (a constant), the mixing efficiency (also a constant), a simple vertical structure function, and a function of the energy transfer associated with baroclinic conversion, $E(x, y)$. The latter term is retrieved from an internal wave energy map with a global mean value of 1.1 TW (Madec et al., 2017). This agrees well with estimates of

energy dissipation from internal tides, which typically fall in the range of 1–1.25 TW (e.g., Munk & Wunsch, 1998; Garrett & Kunze, 2007). In order to focus on the effects of tidal forcing and SMLEs, this parameterization is not used in our study.

The second parameterization associated with tidal mixing relates to 'Indonesian area specific treatment'. Indonesia is not within the ANHA4 grid, so this parameterization cannot be expected to affect our study. However, for completeness I will briefly describe it here. It is intended to capture the effects of the topographically-complex Indonesian Archipelago, which tends to retain internal tides within its semi-enclosed border. Hence, its principal effect is to increase the fraction of locally-generated tidal energy that is available for mixing. It also alters the vertical structure function so that it is not based on bottom intensified mixing, but rather on the structure of the thermocline (Madec et al., 2017).

2.4.3 The Submesoscale mixed layer eddies parameterization

The SMLEp was developed following the earlier Gent and McWilliams (1990) parameterization of mesoscale eddy-induced turbulence (Fox-Kemper et al., 2008). The intention of the Gent and McWilliams parameterization is to capture lateral mixing from mesoscale eddies, and it does this by advecting tracers based on large-scale quantities (namely the slope of iso-neutral surfaces), eventually releasing mean potential energy (Madec et al., 2017).

SMLEs have already been discussed at length in Section 1.6. The SMLEp is cast as an overturning streamfunction, $\mathbf{\Psi}$, which produces a velocity field, $\mathbf{u}^* = \nabla \times \mathbf{\Psi}$. Similarly to Gent and McWilliams (1990), the resultant velocity field is used to advect tracers such that density fronts are slumped from the vertical to the horizontal, thereby releasing potential energy (Fox-Kemper et al., 2011).

The theoretical streamfunction developed by Fox-Kemper et al. (2008) is based on the product of the mixed layer depth, the horizontal buoyancy gradient, and the Coriolis parameter. However, for $\mathbf{\Psi}$ to be implemented in OGCMs, it is modified in two ways—Equation 1.6 is the modified formulation. The first modification is to the denominator. Originally, it contains only the Coriolis parameter, f, which creates a singularity at the Equator where $f \to 0$. In the modified streamfunction, the denominator includes an additional term based on the time to mix momentum across the mixed layer, τ. The second modification is necessary because coarse resolutions cannot define sharp horizontal buoyancy fronts. The parameterization is therefore scaled by $\Delta s / L_f$, where Δs is the horizontal grid spacing and L_f is the smallest width of unresolved fronts within each grid cell (Fox-Kemper et al., 2011).

In ANHA4, a third NEMO-specific modification is also implemented, and in so doing it

deviates from the original Fox-Kemper et al. (2011) parameterization. Specifically, it uses an updated definition of L_f,

$$L_f = L_0 f_0, \tag{2.10}$$

where L_0 and f_0 are reference values. The original definition of L_f is given in Equation 1.7.

In ANHA4, L_0 is based on the conservative minimum recommendation of $L_{f_{\min}} = 5$ km from Fox-Kemper et al. (2011), and f_0 is taken at 20° N. Since this means the $\Delta s / L_f$ scaling is constant in time, this new formulation is a simplification of the original parameterization. However, it has the advantages of not relying on a specific method for calculating the buoyancy frequency (which is used in Equation 1.7), and it guards $\mathbf{u}^*$ from excessively large values since L_f remains relatively large throughout all latitudes. Additionally, L_f is no longer a function of H (the MLD), meaning that the parameterization is more sensitive to H than in the original formulation (Calvert et al., 2020).

Making this simplification is justified since, as noted in Section 1.6, L_f is a tuneable parameter with no compelling alternative definition (except perhaps the recently proposed definition from Bodner et al., 2023). Admittedly, this means that there might be more optimal values than $L_0 = 5$ km and $f_0 = f(20°\ N)$, although it is out of the scope of this thesis to identify them. It is furthermore reassuring to note that, while using these same values in a 1/4° ocean-sea ice NEMO model, Calvert et al. (2020) found that the parameterization reduced wintertime deep MLD biases from 17% to 9%. In the Labrador Sea, bias was reduced even further, from 185% to 157%. Conversely, shallow MLD biases increased 2% globally.

2.5 Overview of ANHA4

The ANHA4 grid was extracted from the 1/4° tripolar ORCA025 grid (Garcia-Quintana et al., 2019). It extends across the Arctic and Atlantic Oceans, from approximately 20° S to Bering Strait. In the LS, its 1/4° resolution yields a horizontal grid spacing of approximately 15–20 km. This is shown in Figure 2.2. In the vertical, ANHA4 uses z^*-coordinates with 50 vertical levels. Layer thickness increases with depth, from 1.02 m at the surface to 458.39 m at depth. However, in the LS, bathymetry limits the model to 46 levels, with the deepest layer centred at a depth of 3,992.48 m and having a thickness of 404.42 m.

A horizontal resolution of 1/4° is generally the finest ocean resolution commonly used in modern global coupled climate models (Hewitt et al., 2020). It can be termed 'eddy permitting' because it captures much of the mesoscale eddy field (Hirschi et al., 2020). However, it

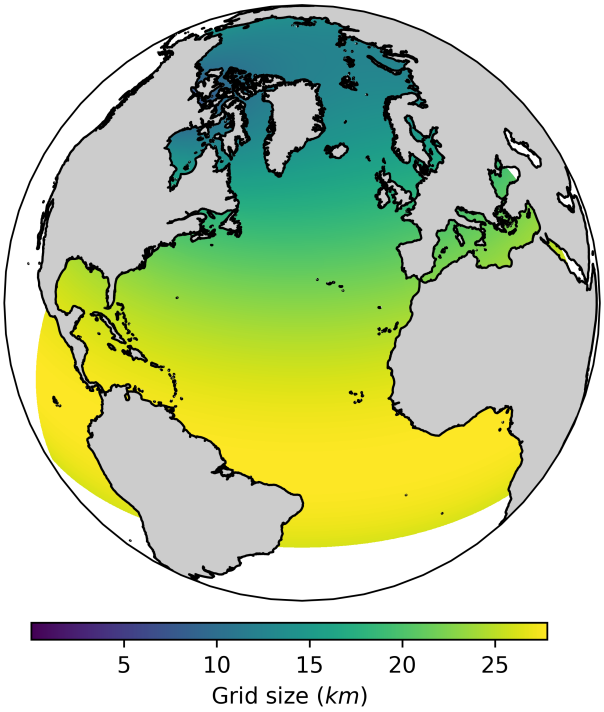

Figure 2.2: The ANHA4 domain, encompassing the North Atlantic and Arctic Oceans, from 20° S to Bering Strait. Grid spacing is indicated by colour, and is approximately 15–20 km in the Labrador Sea.

is important to note that, during deep convection, the Rossby radius of deformation (defined as $L_\rho = NH_B/f_0$ following Marshall & Schott, 1999) can be reduced to as small as a few kilometres. The ANHA4 grid therefore cannot be expected to capture a large portion of the geostrophic eddy field during deep convection in the LS.

ANHA4 is a coupled ocean-sea ice model using the Louvain-la-Neuve version 2 (LIM2) sea ice module (Fichefet & Maqueda, 1997). Sea ice thicknesses from this setup compare reasonably well with observations except in the high Arctic; we refer the reader to Hu et al. (2018) for further reading on this topic. The model is also coupled with BLING (Biogeochemistry with Light Iron and Nutrient limitation and Gases), a reduced complexity biogeochemistry model (Galbraith et al., 2010).

In the present study, six ANHA4 simulations are analyzed. All six simulations are initialized and forced at the open boundaries by GLORYS2v3 (Global Ocean Reanalysis and Simulations; Masina et al., 2017). Monthly interannual river discharge is mostly based on the 1° resolution dataset from Dai et al. (2009). In the Arctic, a newer runoff dataset is used, based on the Arctic-HYPE (Hydrological Predictions of the Environment) model (Lindström et al., 2010). Additional freshwater fluxes from Greenland are based on Bamber et al. (2018).

Each run has a unique combination of atmospheric forcing, tidal forcing, and the SMLEp.

Table 2.1 clarifies these differences.

Table 2.1: The six runs analyzed in our study, which differ in their atmospheric forcing (CGRF[1] or ERA-I[2]), tidal forcing, and use of the SMLEp. Our internal naming system is given for future reference as well as the naming system used henceforth within this text.

	Internal name		Abbreviation	
Model setup	CGRF	ERA-I	CGRF	ERA-I
Control	EPM157	EPM158	CGRF-C	ERAI-C
Tidal forcing	EPM151	EPM152	CGRF-T	ERAI-T
Tidal forcing and SMLEs	EPM155	EPM156	CGRF-TS	ERAI-TS

Three runs employ ERA-I for atmospheric forcing, which is a popular global atmospheric reanalysis product with a horizontal resolution of 79 km and a temporal resolution of 3 hours (Dee et al., 2011). The other three runs are forced by CGRF, a global atmospheric reforecast product with similar temperature, humidity, and wind biases to ERA-I but with a considerably higher nominal resolution of 33 km and a temporal resolution of one hour (Smith et al., 2014). Two runs, one per atmospheric product, are considered control runs with neither tidal forcing nor the SMLEp. Four runs employ surface tidal potential forcing, in which case 9 constituents are used; $K1$, $K2$, $M2$, $M4$, $N2$, $O1$, $P1$, $Q1$, and $S2$. SAL is also included in these four runs, as well has harmonic forcing at the lateral boundaries. Additionally, two of these tidally-forced runs also employ the SMLEp.

[1]The Canadian Meteorological Centre's Global Deterministic Prediction System Reforecasts (Smith et al., 2014)

[2]The European Centre for Medium-Range Weather Forecasts Re-analysis Interim (Dee et al., 2011)

Chapter 3

Results

3.1 Introduction

Our goal is to evaluate how tidal forcing and the SMLEp affect deep convection in the LS. To do this, we consider six ANHA4 simulations with different combinations of tidal forcing, the SMLEp, and atmospheric forcing. When evaluating these simulations, it is useful to consider two separate but linked categories of phenomena: boundary-interior exchange and interior-only dynamics. As discussed previously, boundary currents surrounding the LS contain waters of Arctic origin as well as waters of Atlantic origin. Instabilities, both barotropic and baroclinic, can flux these highly-stratified waters into the interior and inhibit deep convection (Chanut et al., 2008; Rieck et al., 2019; Pennelly & Myers, 2020). Baroclinic instabilities are also generated within the interior alone, caused by strong lateral density gradients at the borders of convective plumes. Submesoscale eddies of this type have fast growth rates of O(1/day) and small scales of O(1 km), and play an important role in restratifying the surface following deep convection (Fox-Kemper et al., 2008; Frajka-Williams et al., 2014). With a horizontal resolution of 1/4°, ANHA4 cannot be expected to represent any of these submesoscale eddies; this is the justification for using the SMLEp.

Similarly, ANHA4 cannot be expected to represent the full internal tide spectrum. However, Megann (2024) demonstrates that 1/4° NEMO simulations can represent at least the first mode internal tide for the five constituents he considers (all of which are included here, within our simulations, along with four additional constituents). In the open ocean, the expected behaviour of such internal tides is to increase diapycnal mixing (Munk & Wunsch, 1998). Megann (2024) found that tidal forcing in z^*-coordinate simulations indeed increased mixing over much of the ocean, generally reducing its stratification, except in the Southern

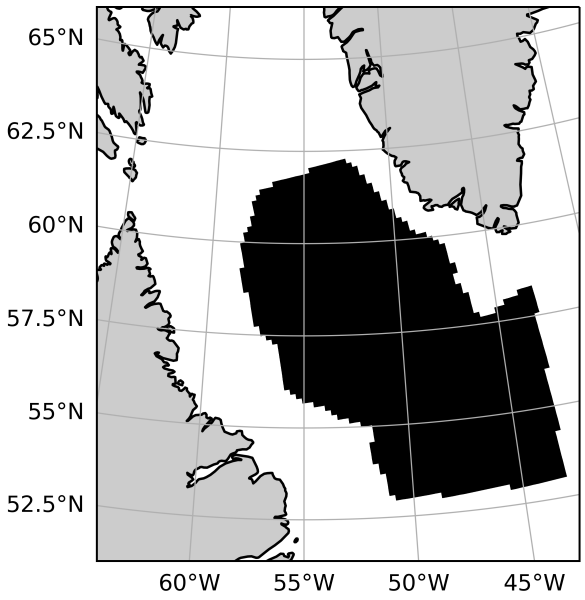

Figure 3.1: Definition used hereafter for the interior Labrador Sea, which follows the 3,000 m isobath around the continental shelves. Its southern and eastern borders extend zonally and meridionally from southern Labrador and Cape Farewell (Greenland), respectively.

Ocean. The net result was improved realism, although he does not explicitly consider the mixed layer or deep convection zones like the Labrador Sea.

In this section we demonstrate the effects of tidal forcing and the SMLEp on deep convection in the LS. Our analyses are primarily focused on the interior of the LS; Figure 3.1 shows how we define this region based on the 3,000 m isobath. In the next subsection, we begin with a review of how ANHA4 represents the boundary currents and mean hydrography of the LS. We then evaluate the strength of the deep convection in our simulations. Next, we analyze the modulating factors of LS buoyancy, namely, FWC and heat content as well as freshwater and heat fluxes. We then evaluate the energetics of ANHA4, focusing on proxies of baroclinic and barotropic instabilities. Finally, we diagnose the strength of the SMLEp, to provide context on its behaviour, as well as the concentrations of oxygen and carbon contents.

3.2 Boundary currents and mean hydrography

Before discussing the effects of tidal forcing and the SMLEp on deep convection in the LS, it is prudent to first evaluate how ANHA4 represents the basic current system and hydrography. As discussed in Section 1.3, the LS is surrounded by cyclonic boundary currents, typically classified as the WGC and the LC. The WGC is characterized by a strong front over the shelfbreak, separating cold and fresh inland waters from warm and salty waters farther offshore and down the continental slope. Using a 1/60° resolution NEMO model, Gou et al. (2022) further differentiate the WGC from the West Greenland Coastal Current

(WGCC), which carries the coldest and freshest waters in the region. The LC is formed by the WGC merging with the BIC as it crosses Davis Strait, turns southward, and then merges with outflow from Hudson Strait. Like the WGC, it is typically said to have two branches separated by a front, with cold, fresh waters on the continental shelf and warm, salty waters farther offshore (Fratantoni & Pickart, 2007; Chanut et al., 2008).

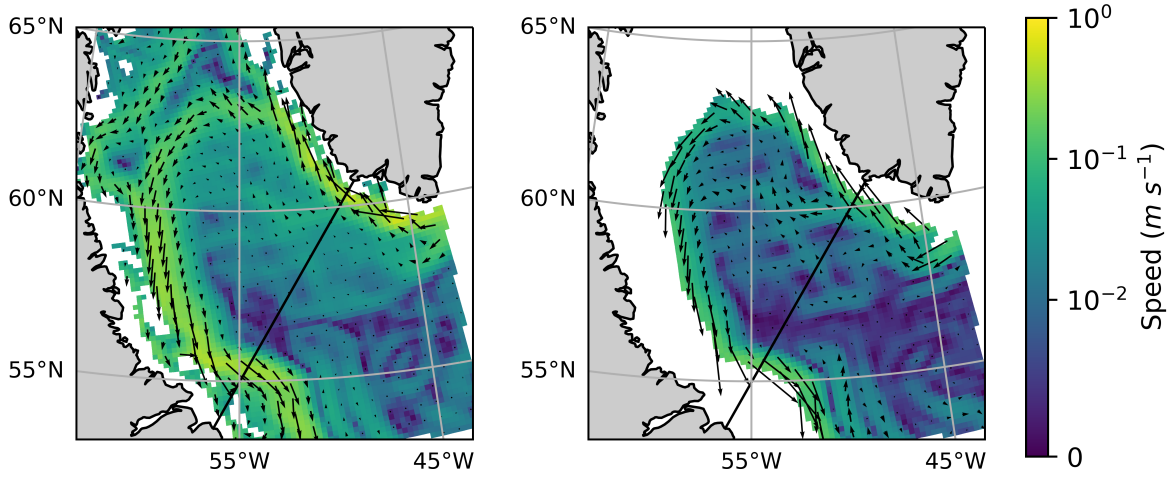

Figure 3.2: Maps of Labrador Sea currents averaged during 2008–2018 (inclusive) within an ANHA4 simulation. The colour scale is linear from 0 to 10^{-2} and logarithmic elsewhere, and it indicates speed. The black arrows represent velocity vectors. The black line extending from Labrador to Greenland approximately demarcates the AR7W section. **Left**: Average velocity from the surface to 200 m. **Right**: Average velocity from 200 m to 2,000 m. For both the left and right panels, we mask out depths shallower than 200 m and 2,000 m, respectively.

This behaviour is generally well-represented in ANHA4, with some shortcomings discussed below. In Figure 3.2, the left panel shows a realistic surface jet. It begins at Cape Farewell before bifurcating at Davis Strait. As the major, westward portion reaches the Labrador Coast, it joins with the BIC and subsequently follows the shelfbreak southward. The right panel shows a weaker but persistent system which mimics the surface current. In both panels, the lowest speeds are located in the southwest interior LS, which is the prototypical site of deep convection. The surface jet is also shown in the top panels of Figure 3.3, where intensified velocities co-occur with steepened isopycnals at the shelfbreak. On the Labrador side (top left), an inshore current is also present, as indicated by a modest jet and steepened isopycnals. Conversely, in the top right panel, no such inshore current (i.e., the WGCC) is captured. This is expected, since ANHA4's 1/4° resolution results in only one cell over the west Greenland shelf.

Figure 3.3 also shows mean salinity across the full AR7W section (bottom panel). The saltiest class of water, with a salinity above 35.00 PSU, is located at intermediate depth. Above and below this, salinities are lower. This is broadly consistent with the idea that a

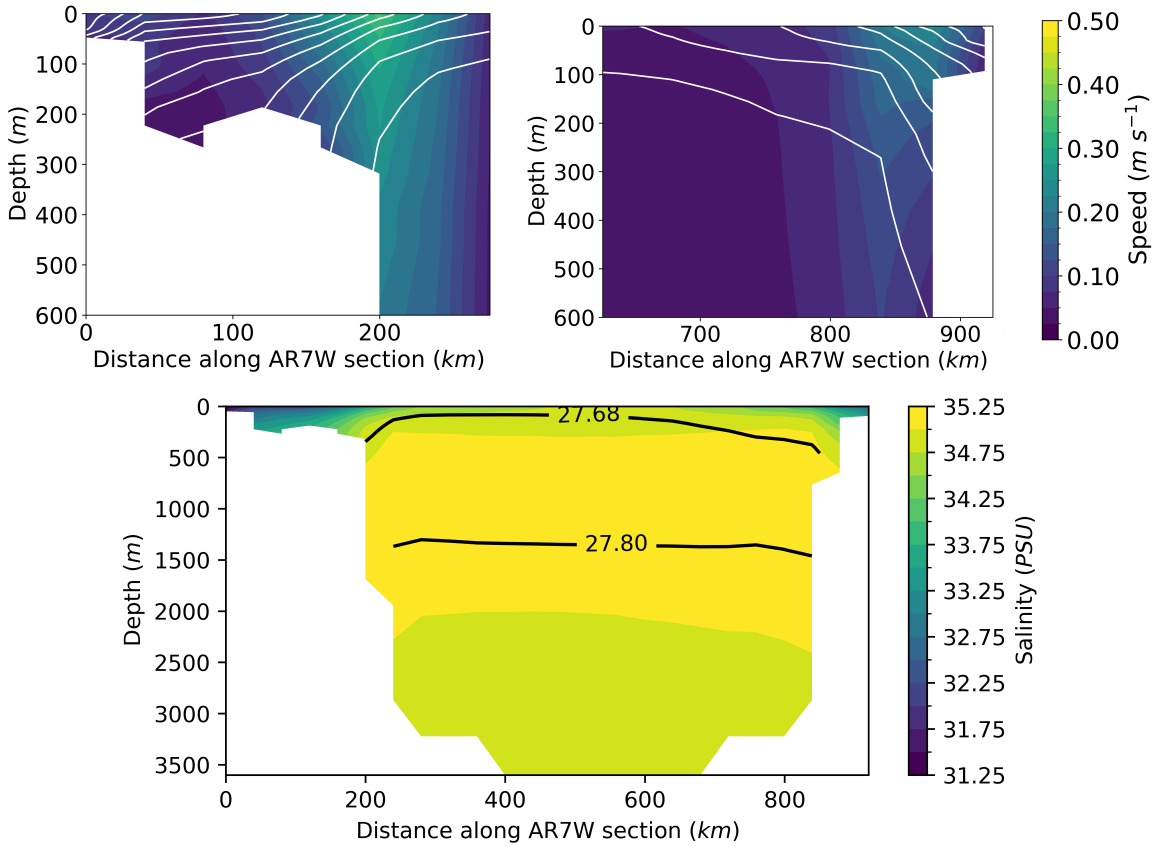

Figure 3.3: Cross-sections of the mean currents and hydrography in the Labrador Sea along the AR7W section, averaged during 2008–2018 (inclusive) within an ANHA4 simulation. **Top**: Velocities and ispocycnals in the Labrador Current (**left**) and the West Greenland Current (**right**). White lines denote isopycnals incremented every 0.2 kg m^{-3}, with the densest isopycnals in both panels corresponding to a potential density of 1,027.6 kg m^{-3}. **Bottom**: Salinity across the full AR7W section, with two isopycnals at 1,027.68 kg m^{-3} and 1,027.80 kg m^{-3} (using σ_T notation), which correspond to a common definition of Labrador Sea Water.

thick layer of relatively salty NADW lies beneath fresher LSW and overtop denser DSOW (Hall et al., 2013; Yashayaev & Loder, 2016; Petit et al., 2023).

Isopycnals of potential density corresponding to a common definition of LSW, 1,027.68–1,027.80 kg m^{-3} (e.g., Kieke et al., 2007; Garcia-Quintana et al., 2019), are also shown. The considerable overlap of this density class with the >35.00 PSU layer disagrees with shipboard hydrography, which usually finds that salinities do not peak until well below the 1,027.80 kg m^{-3} isopycnal (e.g., Hall et al., 2013; Yashayaev & Loder, 2016). This discrepancy is likely explained in part by seasonal aliasing in shipboard measurements along the AR7W section. Additionally, there is a noted tendency for numerical models to experience a positive salinity drift, which might also explain the excessive amount of water in our cross-sections over 35.00 PSU (Rattan et al., 2010). While this is an important cause for concern, it is somewhat

mitigated in our study by limiting most analyses to our twinned simulations, which all show the same excessive >35.00 PSU layer. Similarly, all of our simulations exhibit the same shelfbreak front and jet. For these reasons, in both Figure 3.2 and 3.3, we are only showing the means of CGRF-TS, and it would be redundant to include corresponding figures for the other five runs.

3.3 Stratification and mixed layer depths

In this section, we focus our attention on how tidal forcing and the SMLEp affect deep convection. We begin our analyses by considering convective resistance, Ω_{CR}, for the decade from 2008 to 2017. We use this period because it avoids model spin-up and also includes years of both shallow (2010–2013) and deep (2015–2018) observed MLDs (Rühs et al., 2021; Yashayaev, 2024). Convective resistance measures the amount of energy that must be removed from a region to produce neutral stratification from the surface to a reference depth, h. It is given by

$$\Omega_{CR}(h) = \frac{g}{A} \iint \left[h\rho_\theta(h) - \int_0^h \rho_\theta(z) dz \right] dA, \tag{3.1}$$

where A is the area of our region of interest, $\rho_\theta(h)$ is potential density at the reference depth h, and $\rho_\theta(z)$ is potential density through the water column (Pennelly & Myers, 2020). In this study, h is taken as 2,000 m.

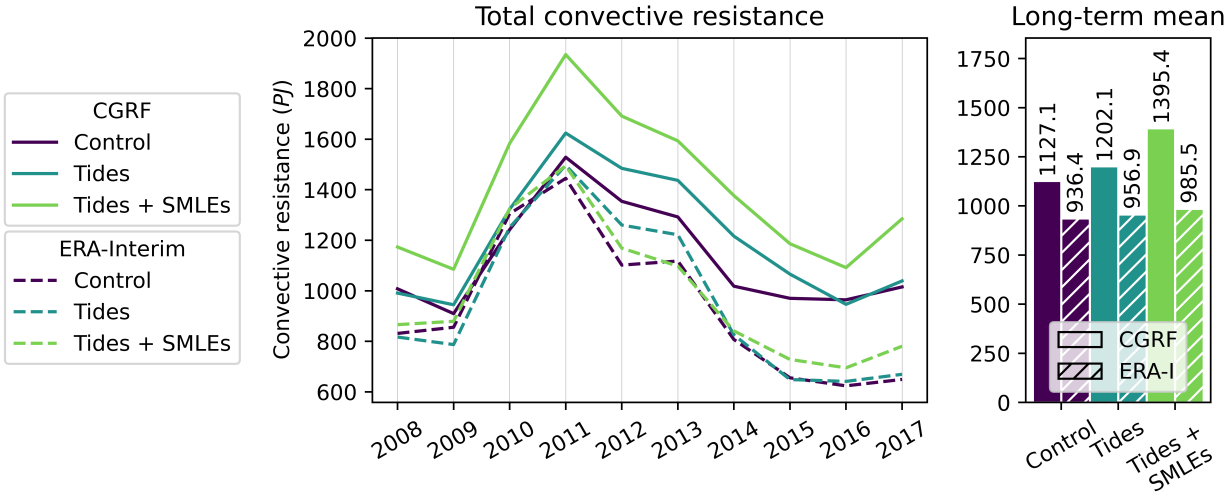

Figure 3.4: Spatially-totalled convective resistances in the interior Labrador Sea, referenced to a depth of 2,000 m. The time-series uses yearly averages, defined from December to November (e.g., the 2008 year is defined from December 2007–November 2008). Long-term means are calculated during the decade from 2008 to 2017.

The units of Ω_{CR} are J m^{-3}. Hence, we obtain the total energy that must be removed to produce neutral stratification in a given region by integrating Ω_{CR} over the region's volume. Figure 3.4 shows integrated values for all six simulations within the interior LS. Considering the long-term means, tidal forcing increases Ω_{CR} for both the CGRF and ERA-I runs, with a stronger effect on the former (6.7%) than the latter (2.2%). By introducing SMLEs, Ω_{CR} is further increased compared to the tidal runs, with a significantly stronger effect using CGRF (16.1%) than using ERA-I (3.0%). Throughout the full time-series, CGRF-TS consistently has the highest convective resistance, peaking at 2,237 PJ in late September 2011. The five other runs also experience maximums of 1,857–1,947 during autumn 2010–2011, a period with noted weak atmospheric forcing (Yashayaev, 2024). Later, strong atmospheric forcing in 2015–2016 leads to minima in the range of 203.3–663.8 PJ, with the former value corresponding to ERAI-C during early April 2016. To summarize, both tidal forcing and the SMLEp increase convective resistance, as does using CGRF forcing compared to using ERA-I.

We define MLDs in this study using the density algorithm method from Holte and Talley (2009). The density algorithm method was created as an alternative to density threshold methods, which tend to produce overestimations of the MLD (Courtois et al., 2017; Pennelly & Myers, 2020; Rühs et al., 2021). Figure 3.5 shows MLDs averaged spatially within the interior LS. In addition to the six ANHA4 runs, we also include MLDs from LAB60, a 1/60° nest of the LS (Pennelly & Myers, 2020), as well as observational data from Argo floats (Holte et al., 2017).

LAB60 is nested within a 1/12° nest which itself is within ANHA4. It was created to investigate the effects of small-scale features (e.g., boundary current instabilities) that would be otherwise unresolved in ANHA4 (Pennelly & Myers, 2020). Since such features can strongly affect LS stratification, it might be expected that LAB60 MLDs are a reasonable target for our six ANHA4 simulations. However, during our period of interest, 2008–2017, the specific LAB60 run analyzed here (LAB60-DFS) utilizes the DRAKKAR Forcing Set 5.2 (Dussin et al., 2016) rather than CGRF or ERA-I. For this reason and others relating to the model setup, it is not an ideal comparison for our ANHA4 runs, and we do not readily assume its MLDs are more accurate.

We therefore also consider Argo float data. To permit comparison with model MLDs, the Argo data require some processing. They are first placed onto the ANHA4 grid and discretized into 5-day periods. Within each grid square and period, the MLDs are then averaged. This allows the Argo data to be analyzed in exactly the same way as the ANHA4 output, and it avoids over-weighting MLDs from float measurements that are too close together in

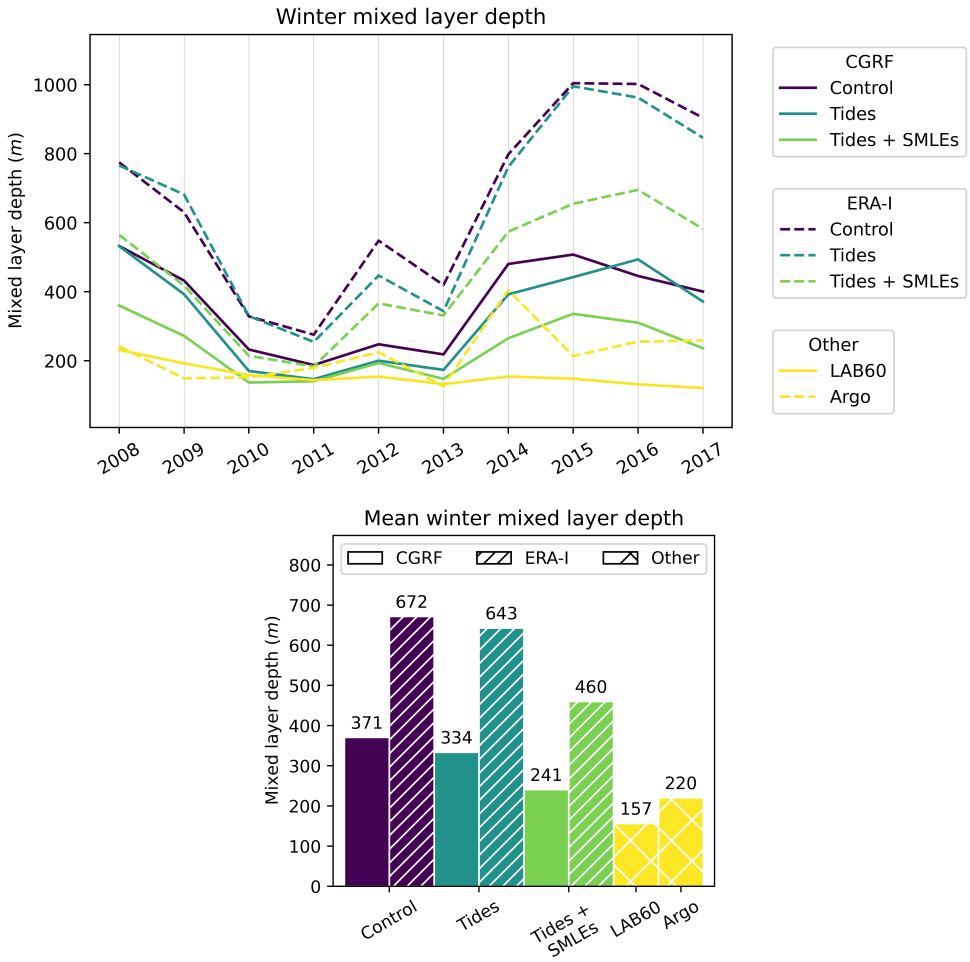

Figure 3.5: Spatially-averaged winter (December to April) mixed layer depths in the interior Labrador Sea. **Top**: Yearly averages. **Bottom**: Ten-year means from 2008 to 2017.

space and time.

In Figure 3.5, the two most shallow mean winter MLDs (bottom panel) belong to Argo and LAB60. This lends currency to the overall accuracy of LAB60 as a more sophisticated model than ANHA4. However, the closest simulation to the observations is actually CGRF-TS, which is only 9.5% too deep compared to LAB60's shallow bias of 28.6%. The other ANHA4 simulations are less accurate than LAB60, with the control runs having the deepest biases for their respective forcing products and with all ERA-I simulations being considerably more biased than those using CGRF.

Considering the time-series (top panel, Figure 3.5), the 2–3 year period after 2010 saw a drastic shoaling of the mixed layer in all runs and in the Argo data. This is unsurprising, based on the weak forcing and strong convective resistances noted previously during this period. Similarly, the strong atmospheric forcing of 2015, which reduced convective resistances for

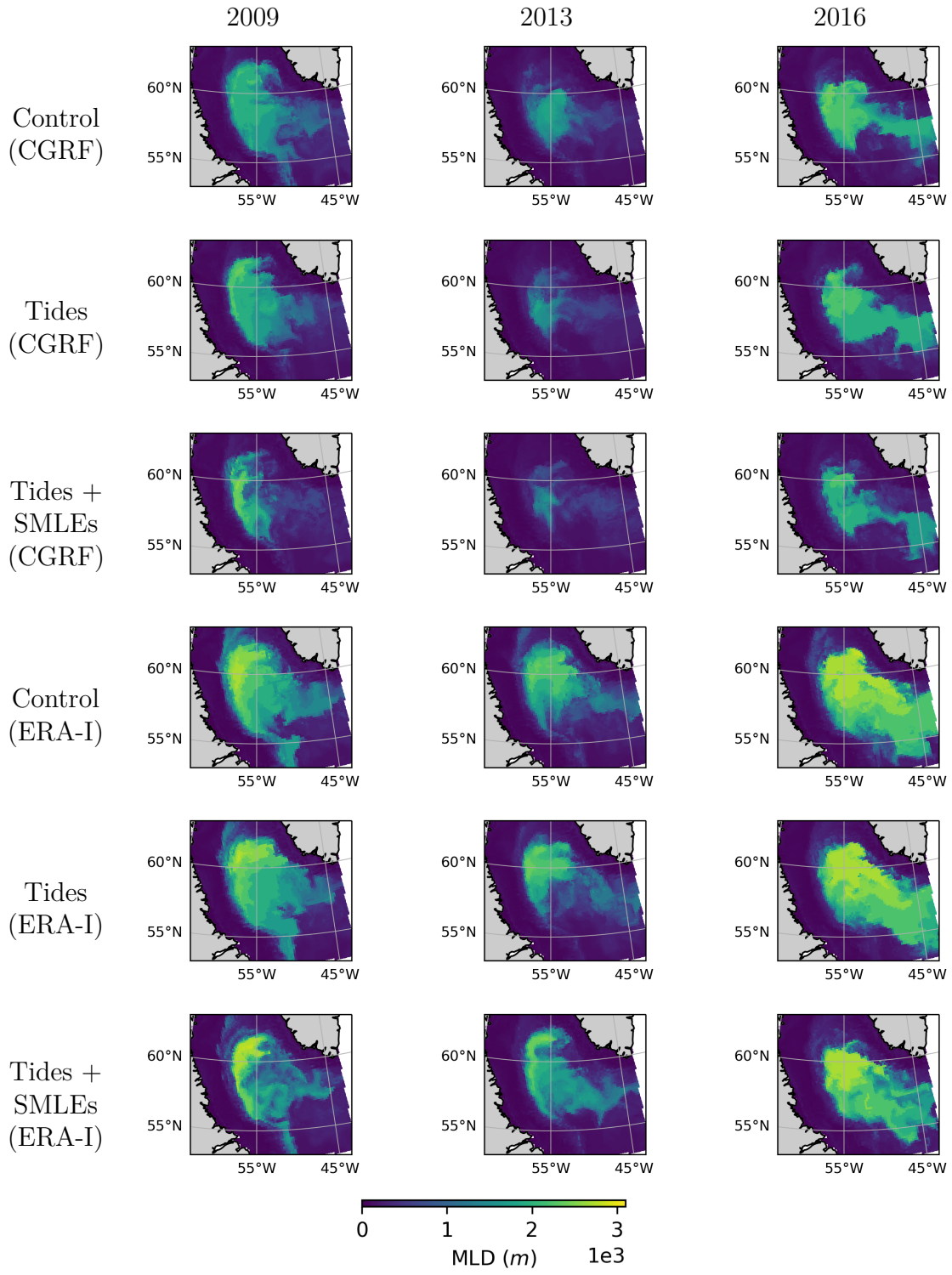

Figure 3.6: Maps of yearly maximum mixed layer depths for all six simulations. Three years are shown from before, during, and after the period of reduced deep convection in 2010–2013.

all runs, is also mirrored here: all six runs experience their deepest MLDs during 2015–2016. This generally follows the observational record, in which 2015 experienced the highest winter cooling for the 1994–2023 period. However, Yashayaev (2024) notes that despite the post-2015 winters producing relatively less cooling, the convective mixing progressively intensified during 2015–2018. This is explained by preconditioning, during which anomalous deep convection leaves the water column more susceptible to overturning in the following winter. Our ANHA4 simulations do not replicate this behaviour during the same 2015–2018 period.

Figure 3.6 shows maps of yearly maximum MLDs for all six runs. Based on the deep-shallow-deep variability in the time-series, three years are shown which correspond to before, during, and after the 2010–2013 period of reduced MLDs. As with Figure 3.5, the runs forced with ERA-I clearly have deeper MLDs than those using CGRF, and they also have larger areal extents of the convective patch. Considering the effects of tidal forcing, it appears to slightly reduce the convective patch, but the effects are subtle, and it is difficult to draw clear conclusions. Conversely, the SMLEp has a stronger effect, with clear reductions in the southern and western extents of the patch. Additionally, it has the interesting effect of introducing more spatial variability within the patch itself, which manifests as dark blue 'filaments' visible throughout the yellow/green region. Another interesting phenomenon is the anomalous eastward shift of the patch, shown here in 2016. This was noted previously by observationalists, who hypothesized that it was related to enhanced melt from Greenland and the advection of an earlier fresh anomaly into the interior LS (Rühs et al., 2021).

In summary, both tidal forcing and the SMLEp reduce the control runs' deep MLD biases, based on the spatially averaged interior MLDs, as does using CGRF forcing compared to using ERA-I. Areal extents are also clearly reduced by the SMLEp, while the effect of tidal forcing is more subtle. However, this is not the full story: the deepest single MLD value in all 18 maps—2,863 m—belongs to ERAI-TS, not the control run. We therefore continue this discussion using an alternative approach to evaluate MLD, the z_{crit} method from Rühs et al. (2021). Figure 3.7 shows this analysis.

The z_{crit} method is used by defining the convective region anywhere the MLD is deeper than a chosen threshold. We follow Rühs et al. (2021) and choose z_{crit} = 1,000 m. This is towards the deep end of the recommended range, which is justified since our simulations have deep MLD biases. Figure 3.7 shows the average MLD within this region, and perhaps surprisingly, there is no significant effect from using tidal forcing or the SMLEp. In fact, while the SMLEs slightly reduces the mean winter MLDs, tidal forcing has a diverging result, slightly reducing the MLD in CGRF-T while slightly increasing it in ERA-T.

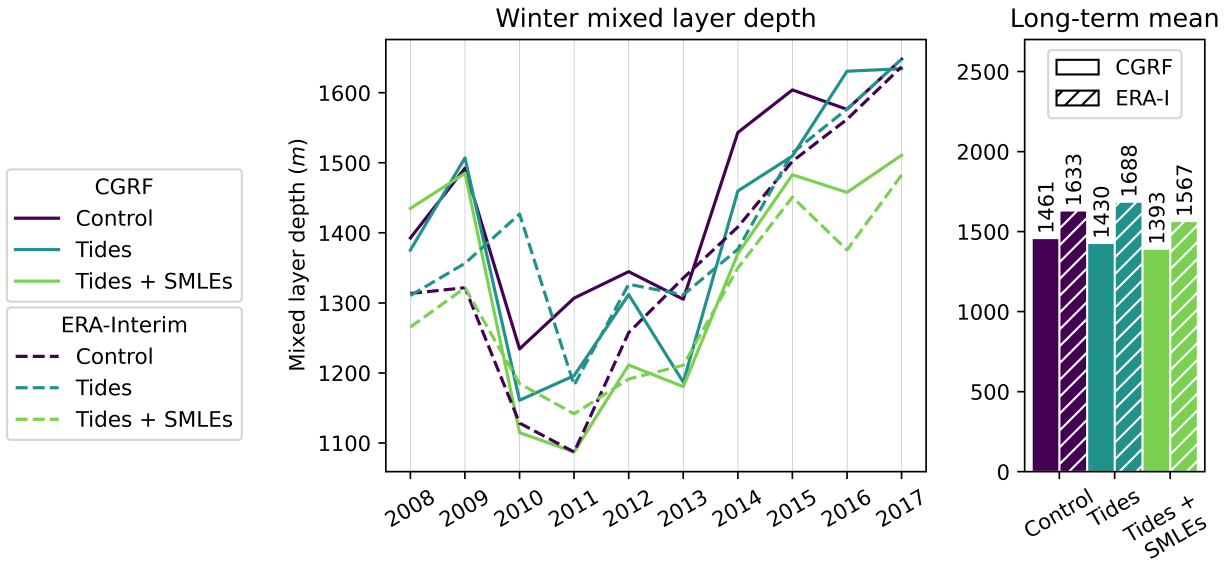

Figure 3.7: Spatially averaged winter (December to April) mixed layer depths in the convection region, defined following Rühs et al. (2021) wherever the mixed layer is deeper than z_{crit} = 1,000 m.

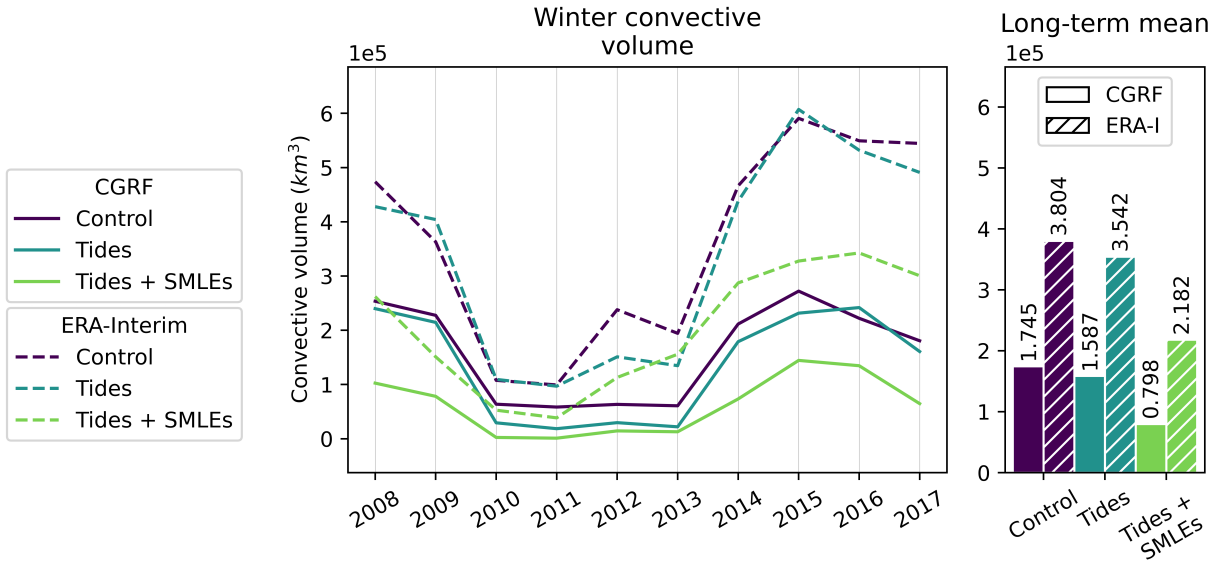

Figure 3.8: Winter (December to April) convective volumes, defined as the volume of the mixed layer wherever it exceeds z_{crit} = 1,000 m.

These results can be explained by considering convective volume, shown in Figure 3.8. Convective volume is defined as the volume of the mixed layer wherever MLD > z_{crit}, and both the time-series and the 10-year means in Figure 3.8 closely resemble the shape and trends of Figure 3.5. In other words, both tidal forcing and the SMLEp reduce convective volume, and using CGRF forcing also reduces it compared to ERA-I. Specifically, the SMLEp

causes reductions of 49.7% (CGRF) and 38.3% (ERA-I), while tidal forcing leads to more modest reductions of 9.5% (CGRF) and 5.9% (ERA-I). These results, taken together with the insignificant differences between the mean z_{crit} MLDs, reveal that the primary effect of tidal forcing and the SMLEp is to reduce the areal extent of the convective patch, rather than to reduce the deepest MLDs.

3.4 Freshwater and heat content

Stratification in the interior LS, and thus deep convection, is modulated by buoyancy fluxes through the surface as well as between the boundary currents and the interior. Since the LS is a transition ocean, where both heat and freshwater affect buoyancy, we begin by discussing heat and freshwater contents (HC and FWC, respectively) in the interior LS. These are given by

$$HC = \rho_0 C_p \int (T - T_{ref})\, dV \tag{3.2a}$$

$$FWC = \int \frac{S_{ref} - S}{S_{ref}} dV, \tag{3.2b}$$

where S is salinity, T is temperature, V is volume, ρ_0 is a reference density (1,026 kg m^{-3}), and C_p is the specific heat capacity of water (4 kJ kg^{-1} °C^{-1}). The salinity and temperature reference values are taken in this thesis as $S_{ref} = 34.8$ PSU and $T_{ref} = -2.0$ °C.

Figure 3.9 shows heat contents in the interior LS integrated both from the surface to 200 m (top panel) and from the surface to the sea floor (bottom panel). Differences in the 10-year means are generally small, although variability between runs is also low. In both panels, tidal forcing has a small but consistent effect of reducing the heat content. Conversely, the effect of the SMLEp diverges depending on the forcing product, causing an increase in heat content in the surface and at depth in CGRF-TS (compared to CGRF-T) but having an insignificant effect in ERAI-TS. Interestingly, the simulations forced with ERA-I generally have higher heat content, with the only exception being CGRF-TS. This is unexpected since the ERA-I simulations have lower convective resistances.

Analogously to Figure 3.9, Figure 3.10 shows FWC from the surface to 200 m (top panel) and from the surface to the sea floor (bottom panel). High-frequency variability is low, so the time-series are not yearly averages, as in most other figures within this thesis. As with heat content, variability between runs is minimal, clearly revealing several important points. First, unlike with heat content, FWC is lower in the ERA-I simulations. This is not surprising,

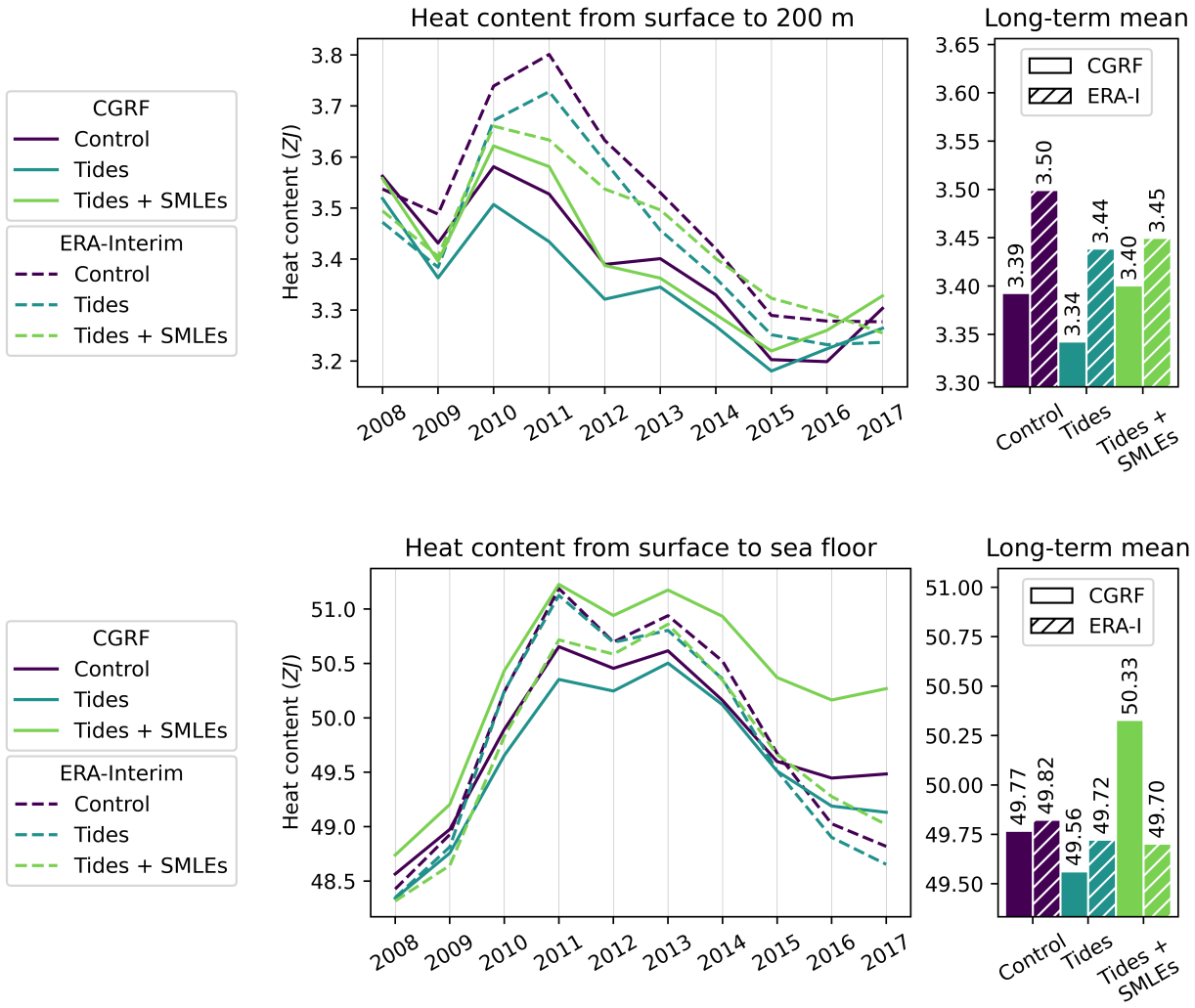

Figure 3.9: Spatially totalled heat contents in the interior Labrador Sea, with yearly averages (defined from December to November) on the left and long-term means on the right. Note 1 ZJ = 10^{21} J. **Top**: Surface heat contents to 200 m. **Bottom**: Heat contents from the surface to the sea floor.

since the ERA-I simulations also have lower convective resistances. Second, tidal forcing has a consistent effect of increasing FWC, both at the surface and at depth. Conversely, the effect of the SMLEp is less pronounced; it increases the surface FWC in CGRF-TS while decreasing the FWC at depth, but it has very little effect within ERAI-TS. Finally, it is interesting to note that all six simulations experience a well-documented (e.g., Rattan et al., 2010; Courtois et al., 2020) salinity drift, with a strongly decreasing FWC until approximately 2011–2012, a decade after the simulations are initialized. We do not know if this behaviour is masking other long-term trends in the models' salinities.

Because heat content and FWC are calculated relative to essentially arbitrary reference values, it is difficult to qualify the significance of the run-to-run differences. However, it

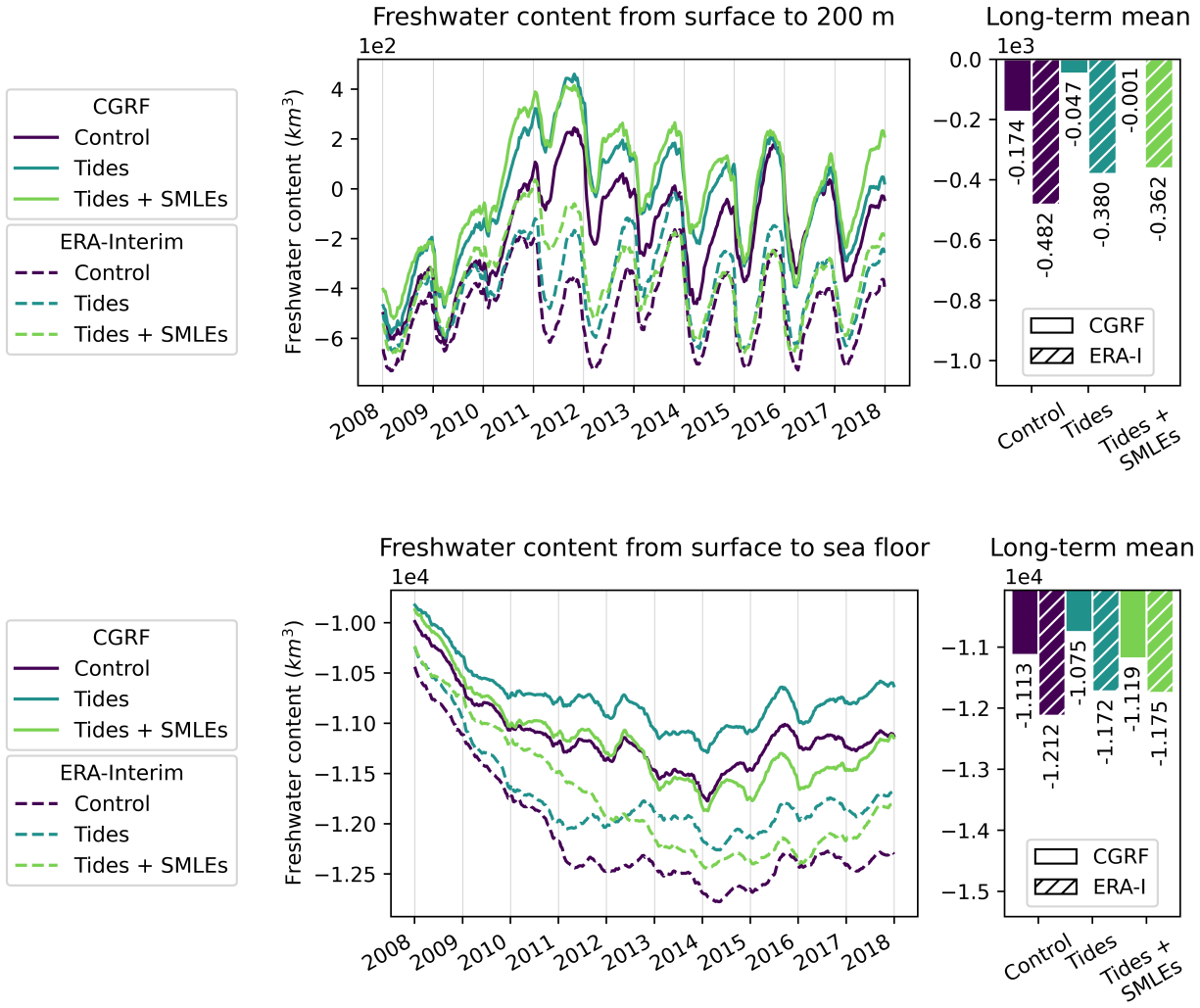

Figure 3.10: Spatially totalled freshwater contents in the interior Labrador Sea, with a time-series on the left and long-term means on the right. **Top**: Surface freshwater contents to 200 m. **Bottom**: Freshwater contents from the surface to the sea floor.

is instructive that heat and freshwater contents are consistently affected by tidal forcing, leading to decreases in heat content and increases in FWC for both CGRF-T and ERAI-T. The effects of the SMLEp are less clear, having a relatively insignificant effect on ERAI-TS but affecting CGRF-TS more noticeably. These effects are, however, inconsistent, increasing heat content at both the surface and at depth while increasing FWC at the surface and decreasing it at depth.

Before entering into a discussion on possible explanations of this behaviour, we would first ideally investigate all possible sources of freshwater and heat into and out of the LS. This would include fluxes through the sea surface as well as lateral fluxes from the WGC, the LC, the NAC, and Davis Strait. However, due to time constraints and the complexity of

calculating fluxes through curved isobath-following sections, we offer only preliminary results below.

Surface fluxes are obtained using Python tools based on the Coordinated Ocean-ice Reference Experiments (CORE) bulk formulae. We refer the reader to W. B. Large (2006), W. Large and Yeager (2009), and Madec et al. (2022) for more details on these algorithms. Using the resultant surface fluxes along with the freshwater and heat contents calculated above, we can then infer the lateral boundary-interior exchange using

$$\Delta\text{FWC} = \Delta t\,[(E - P) + \text{lateral FW flux}] \tag{3.3a}$$

$$\Delta\text{HC} = \Delta t\,[\text{turbulent flux} + \text{radiative flux} + \text{lateral flux}]\,. \tag{3.3b}$$

The principal source of error in these calculations is our treatment of evaporation; its units are kg s^{-1}, and due to time constraints we neglect thermal expansion by converting it to a volume flux using a constant factor of 1,000 kg m^{-3}.

Figures 3.11 and 3.12 show fluxes through the sea surface (top panels) as well as lateral fluxes into the interior LS (bottom panels). Run-to-run variability in the heat fluxes, both through the surface and laterally, are relatively consistent. Comparing the ERA-I and CGRF simulations, those using ERA-I experience significantly stronger atmospheric heat loss, which is consistent with their reduced convective resistances in Figure 3.4. Considering the effects of tidal forcing, both tidally-forced runs experience reduced surface export and reduced lateral import across all years compared to the control runs. Conversely, the SMLEp has a more varied influence; as with the heat content, it affects CGRF-TS more strongly by increasing the magnitude of the heat fluxes, while it has a less significant effect within ERAI-TS.

An interesting phenomenon in Figure 3.11 is the low run-to-run heat flux variability. This, coupled with the mirrored shape of the panels, indicate that the lateral and surface fluxes are tightly correlated with minimal lag. In other words, years with strong surface heat export (e.g., 2015) also experience strong lateral import, and years with weak surface export (e.g., 2010) also experience weak lateral import. This raises an important question: does surface flux drive lateral flux, or vice versa, or are they both driven by something else? To answer this, we must consider the three processes known to drive boundary-interior exchange: wind-driven offshore transport, baroclinic instabilities, and barotropic instabilities (Gou et al., 2022). Since heat diffusion is not one of these processes, we can likely rule out the idea of surface heat loss driving the lateral heat import. In the following section, we consider the other possibilities in greater detail.

Variability between runs in the surface freshwater flux (top panel, Figure 3.12) is mini-

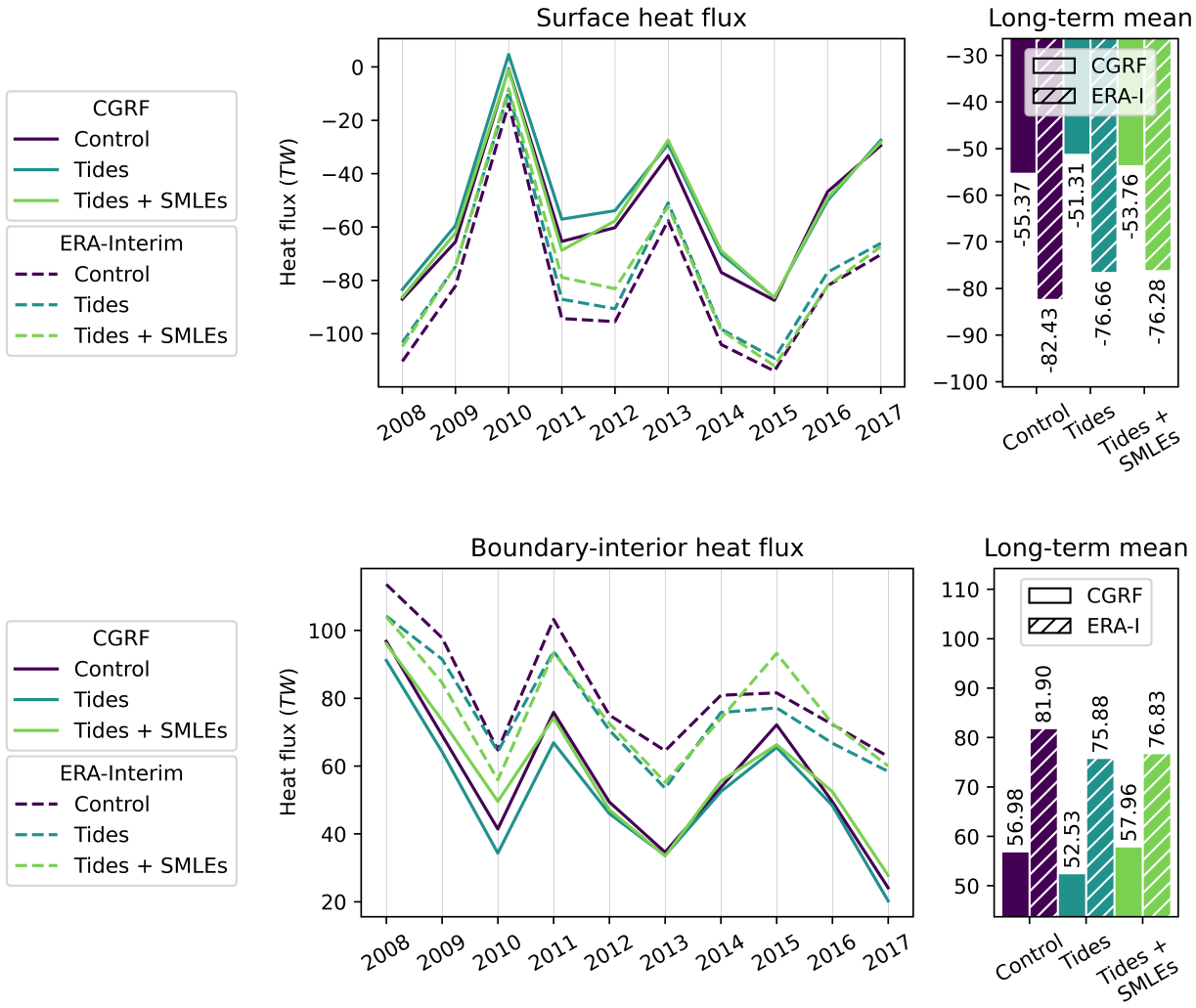

Figure 3.11: Heat fluxes into the interior Labrador Sea, with inward defined as positive. The time-series show yearly averages (defined from December to November) and the bar charts are long-term (10-year) means. **Top**: Surface heat flux. **Bottom**: Lateral heat flux.

mal. Consider, for example, the difference between CGRF-C (11,819 m^{-3} s^{-1}) and CGRF-T (12,023 m^{-3} s^{-1}), an increase of only 1.7%. Conversely, year-to-year variability in the lateral freshwater flux is much stronger. Compared to the heat fluxes, the surface and lateral freshwater fluxes are less tightly coupled. This is not surprising, since surface heat flux can act as a buffer to the interior heat content in a way that $E - P$ likely cannot. In other words, high heat content will lead to higher heat export to the atmosphere, but the feedback loop between the ocean and $E - P$ is likely much weaker.

It is difficult to confidently draw conclusions about the boundary-interior freshwater flux due to the high year-to-year variability. Based on the long-term means, the following is likely true: ERA-I reduces freshwater flux compared to CGRF; tidal forcing increases freshwater

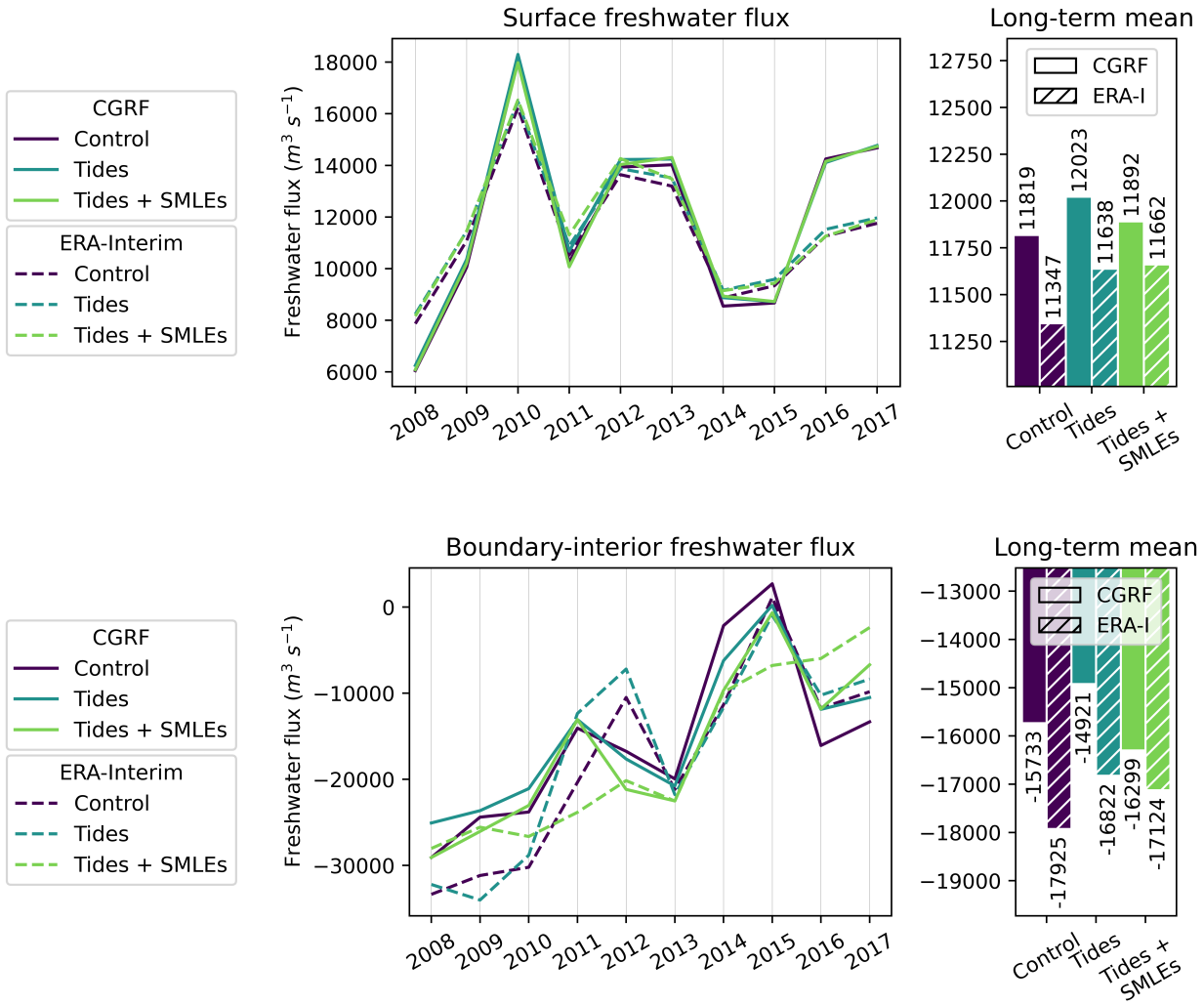

Figure 3.12: Freshwater fluxes into the interior Labrador Sea, with inward defined as positive. The time-series show yearly averages (defined from December to November) and the bar charts are long-term (10-year) means. **Top**: Evaporation minus precipitation. **Bottom**: Lateral boundary-interior exchange.

flux compared to the control runs; and the SMLEp decreases freshwater flux, especially with CGRF forcing. Comparing these observations with Figure 3.10 lends them some currency, since they are consistent with the pattern of surface-to-sea floor FWC.

In summary, long-term means in heat and freshwater contents are well coupled to the fluxes. Namely: (1) runs forced with ERA-I experience increases in heat content, lateral heat import, and surface heat export; (2) they also experienced reductions in FWC and lateral freshwater import (surface fluxes are not strongly affected); (3) tidal forcing reduces heat content, lateral heat import, and surface heat export; (4) tidal forcing also increases FWC and lateral freshwater import (surface fluxes are not strongly affected); (5) the SMLEp has little effect on heat content, FWC, and fluxes in ERAI-TS; (6) however, it does affect

CGRF-TS. Specifically, it increases the magnitude of the heat fluxes (especially the lateral flux) while also increasing the heat content, and it decreases the lateral freshwater import while also decreasing the FWC from the surface to the sea floor.

We have thus far hesitated to offer explanations for any of the behaviour discussed above. Questions therefore persist. For example, is the principal effect of tides to directly modulate heat and freshwater content, and thus stratification, by altering the boundary fluxes? Why does the SMLEp affect the fluxes and contents in CGRF-TS but not ERAI-TS? And why does it increase the FWC at the surface in CGRF-TS while reducing it at depth? To answer these questions, it is useful to first consider the energetics associated with the boundary current instabilities.

3.5 Energetics

EKE measures the strength of eddy activity using the horizontal velocity anomalies (u' and v'). It is formally defined as

$$EKE = \frac{1}{2}\rho_0 \left(u'^2 + v'^2\right), \tag{3.4}$$

where the reference density ρ_0 is taken as 1,025 kg m^{-3}. The velocity anomalies are given by $(u', v') = (u - \overline{u}, v - \overline{v})$, where overbars denote time-averages. Since our model velocities are saved as 5-day means, we cannot capture the very high-frequency EKE. Time-averages are taken using 105-day rolling windows, thereby focusing on intraseasonal variability.

Baroclinic and barotropic instabilities (BCs and BTs, respectively) both contribute to the generation of EKE. Following Rieck et al. (2019) and Gou et al. (2023), we use the following two energy transfer terms as proxies for BCs and BTs:

$$\text{BC} \equiv C(\text{MAPE}, \text{EAPE}) = -\rho_0 \left(\frac{g}{N\rho_0}\right)^2 \left(\overline{u'\rho'}\frac{\partial\overline{\rho}}{\partial x} + \overline{v'\rho'}\frac{\partial\overline{\rho}}{\partial y}\right) \tag{3.5a}$$

$$\text{BT} \equiv C(\text{MKE}, \text{EKE}) = -\rho_0 \left[\overline{u'^2}\frac{\partial\overline{u}}{\partial x} + \overline{v'^2}\frac{\partial\overline{v}}{\partial y} + \overline{u'v'}\left(\frac{\partial\overline{u}}{\partial y} + \frac{\partial\overline{v}}{\partial x}\right)\right], \tag{3.5b}$$

where, as with Equation 3.4, ρ_0 is taken as 1,025 kg m^{-3}. We also include the naming convention from Von Storch et al. (2012), where the energy transfer from $X \to Y$ is denoted as $C(X, Y)$. BCs are thus associated with the transfer from mean available potential energy (MAPE) to eddy available potential energy (EAPE), and BTs are thus associated with the transfer from mean kinetic energy (MKE) to EKE.

Figure 3.13 shows maps of yearly maximums in EKE within our six ANHA4 simulations

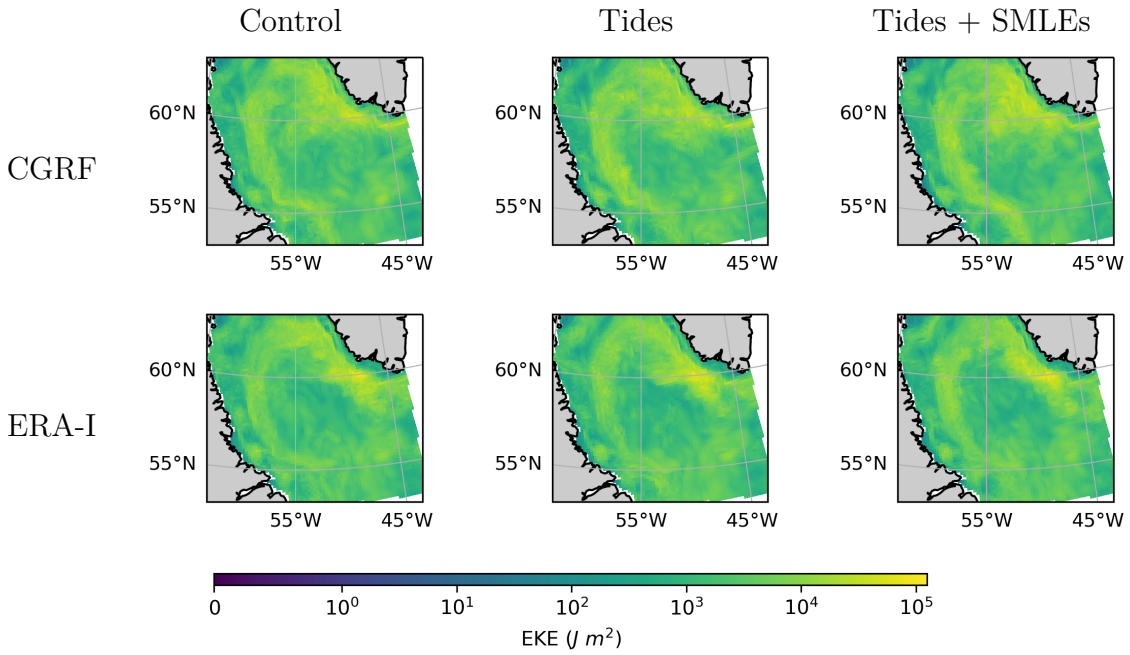

Figure 3.13: Maps of maximums in eddy kinetic energy in the top 2,000 m for all six simulations during the year from October 2016 to September 2017. The colour scale is linear from 0 to 10^0 and logarithmic elsewhere.

for 12 months during 2016–2017. Since our horizontal resolution is 1/4°, we cannot capture a range of the small-scale features. This includes part of the geostrophic eddy field and, importantly, many of the small-scale eddies in the boundary currents that are responsible for part of the boundary-interior exchange. However, Figure 3.13 still reveals several important characteristics. First, across all runs, EKE is highest at Cape Desolation, the main site of IR generation, with the signature of increased EKE in this region extending relatively far into the interior LS. And second, EKE remains high around the full length of the shelfbreak, characteristic of BCEs, which do not travel as far into the interior as IRs (Chanut et al., 2008).

It is difficult to draw any conclusions about the effects of tidal forcing and the SMLEp from Figure 3.13, and neither EKE maps for other years nor difference plots between the simulations reveal any strong qualitative trends. We therefore look to Figure 3.14, which shows average interior EKE over time. In both the top and bottom panels, year-to-year variability is high, and differences in the long-term means are relatively small. This means we must be careful when making inferences. However, there appears to be 5–10% decreases in the long-term means of the tidally-forced simulations compared to the controls, while the SMLEp leads to increases of a similar magnitude.

Figures 3.15 and 3.16 show maps of yearly averages in the BC and BT fields for 12

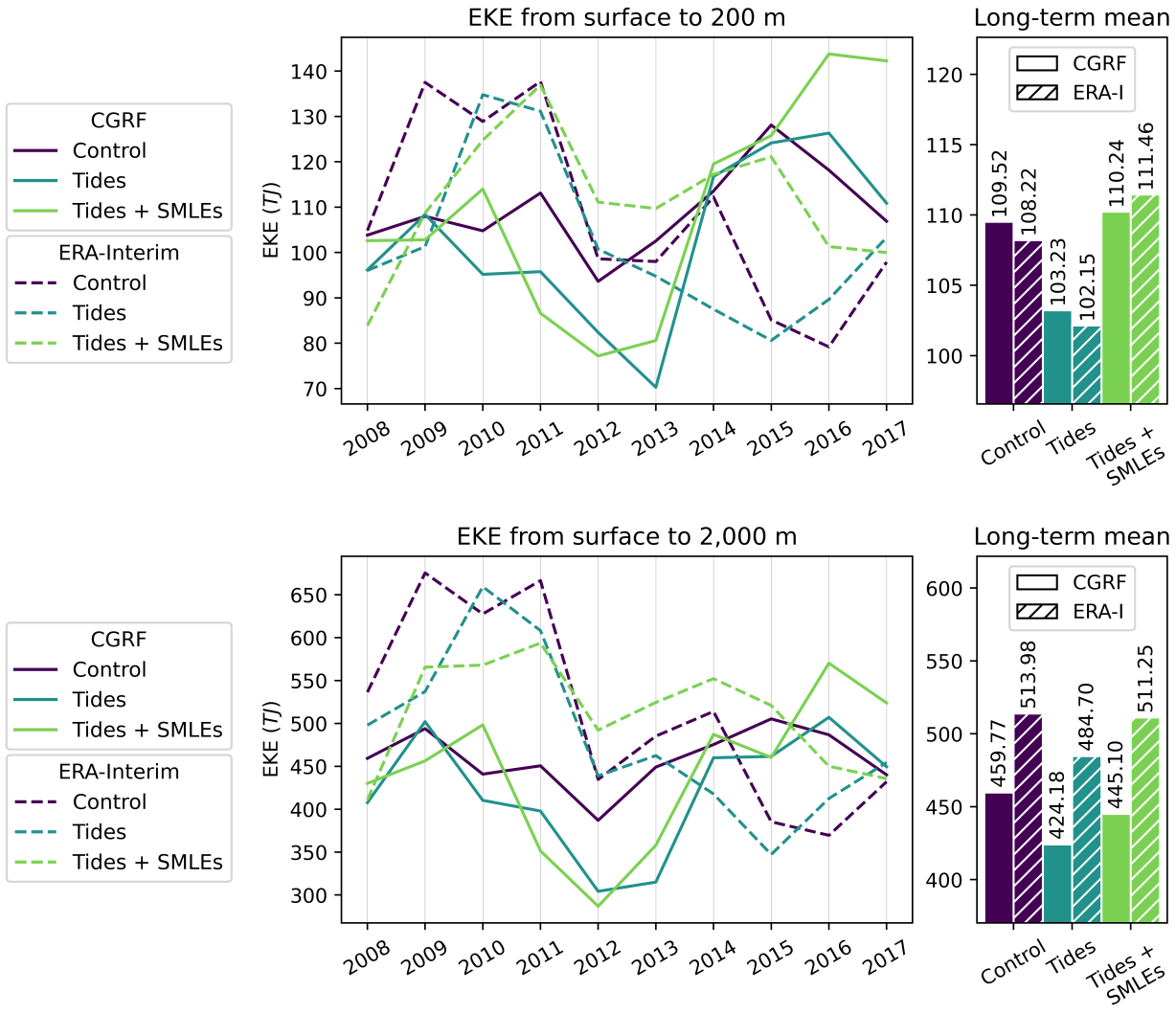

Figure 3.14: Eddy kinetic energy within the interior Labrador Sea from the surface to 200 m (**top**) and to 2,000 m (**bottom**). Yearly averages are defined from October to September.

months during 2016–2017. As with Figure 3.13, the strongest instability activity is at Cape Desolation, with an extended signature of BCs and BTs also continuing along the length of the shelfbreak. It is important to note that mean values are used here instead of maximums because, unlike EKE, BCs and BTs can be negative; this implies eddy attenuation rather than eddy generation. For all six simulations, the signature of BCs (Figure 3.17) show a pattern of generation-attenuation-generation along the west Greenland shelf, previously noted by Gou et al. (2023). Following the shelfbreak, there is a weak but clear signal of positive BC generation, consistent with BCEs (which are primarily baroclinic). As with the EKE maps in Figure 3.13, difference plots are not instructive. However, unlike with EKE, some qualitative trends can be seen in the BC maps. Namely, tidal forcing and the SMLEp

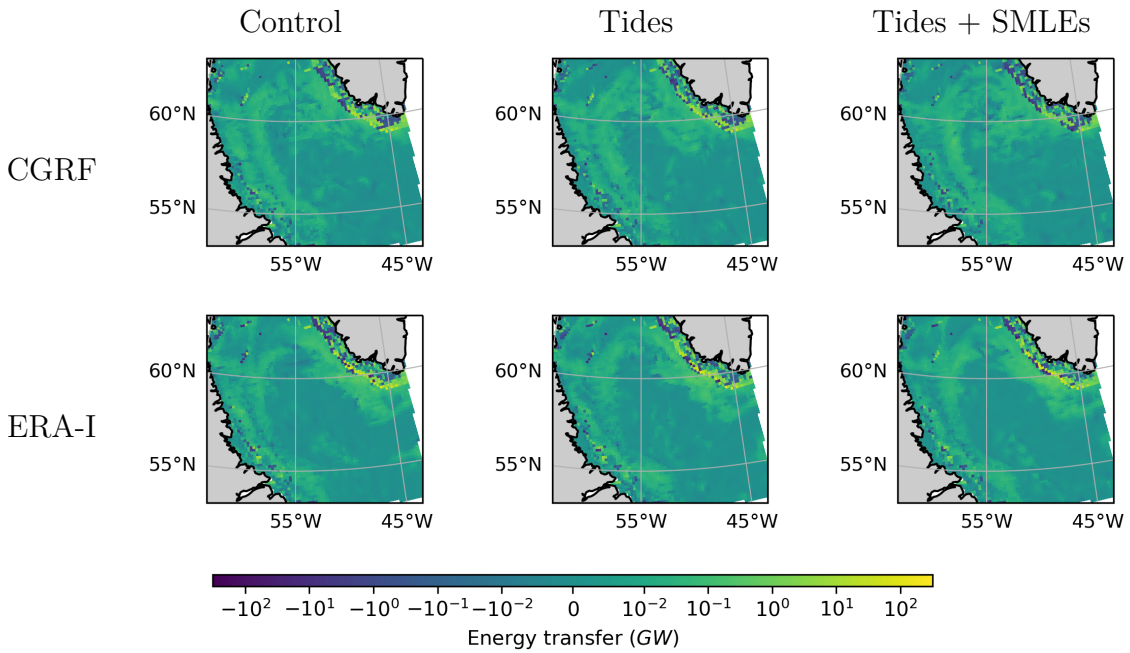

Figure 3.15: Maps of average mean available potential to eddy available potential energy transfer (i.e., baroclinic instabilities) in the top 2,000 m for all six simulations during the year from October 2016 to September 2017. The colour scale is linear from -10^{-2} to 10^{-2} and logarithmic elsewhere.

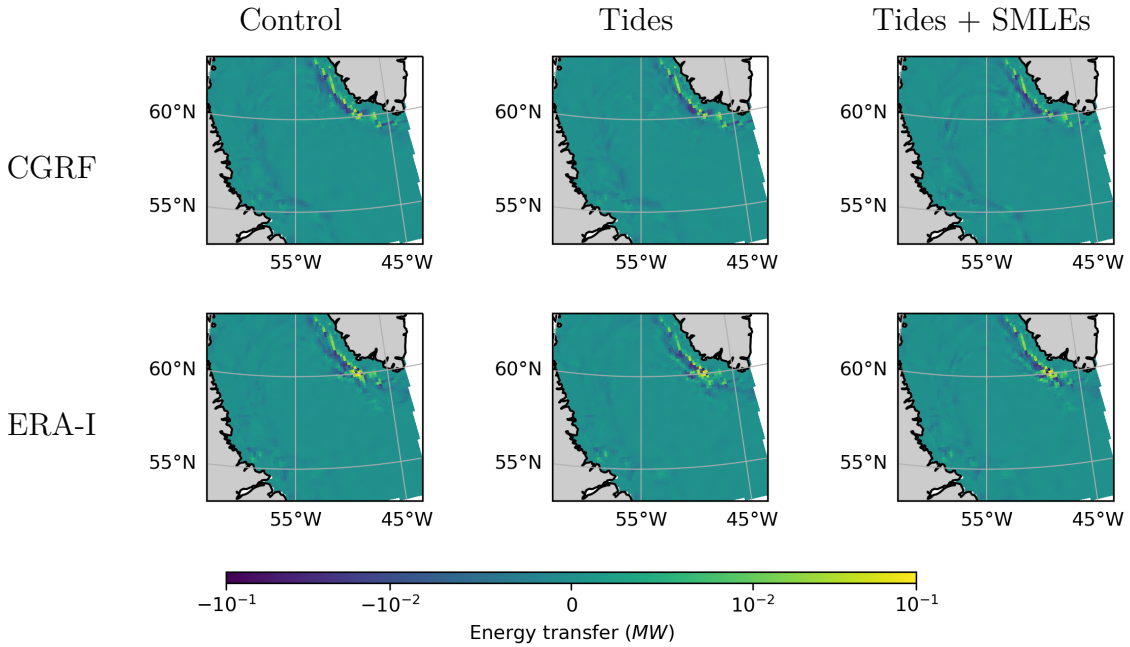

Figure 3.16: Maps of average mean kinetic to eddy kinetic energy transfer (i.e., barotropic instabilities) in the top 2,000 m for all six simulations during the year from October 2016 to September 2017. The colour scale is linear from -10^{-2} to 10^{-2} and logarithmic elsewhere.

both lead to slightly reduced BC generation. This is clear if one focusses on the brightness and/or the areal extent of the yellow colour around Cape Desolation. Figure 3.17 supports this observation, with tidal forcing and the SMLEp both leading to decreases in total BC energy transfer at the surface and at depth. One additional interesting phenomenon here is the diverging impact of ERA-I forcing at the surface, where it is lower than CGRF, versus at depth, where it is substantially higher. This is consistent with the EKE time-series (Figure 3.14), which exhibits the same behaviour.

The signature of BTs in Figure 3.16 is less pronounced than those of BCs. This is most clear from the colour bar, which has a maximum value 10^5 W whereas its counterpart in

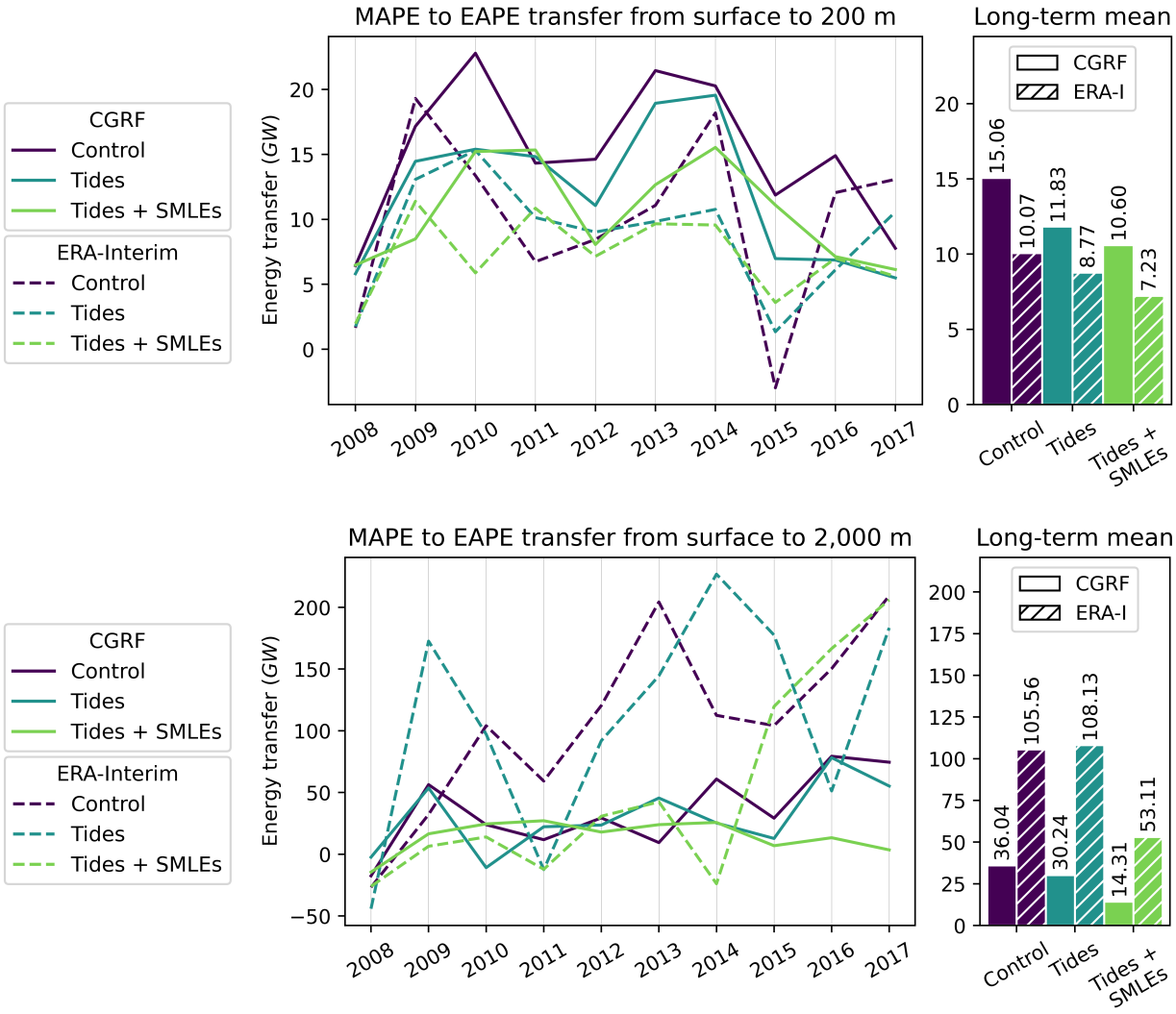

Figure 3.17: Energy transfer rates from mean available potential energy to eddy available potential energy integrated (i.e., baroclinic instabilities) within the Labrador Sea, from the surface to 200 m (**top**) and to 2,000 m (**bottom**). Yearly averages are defined from October to September.

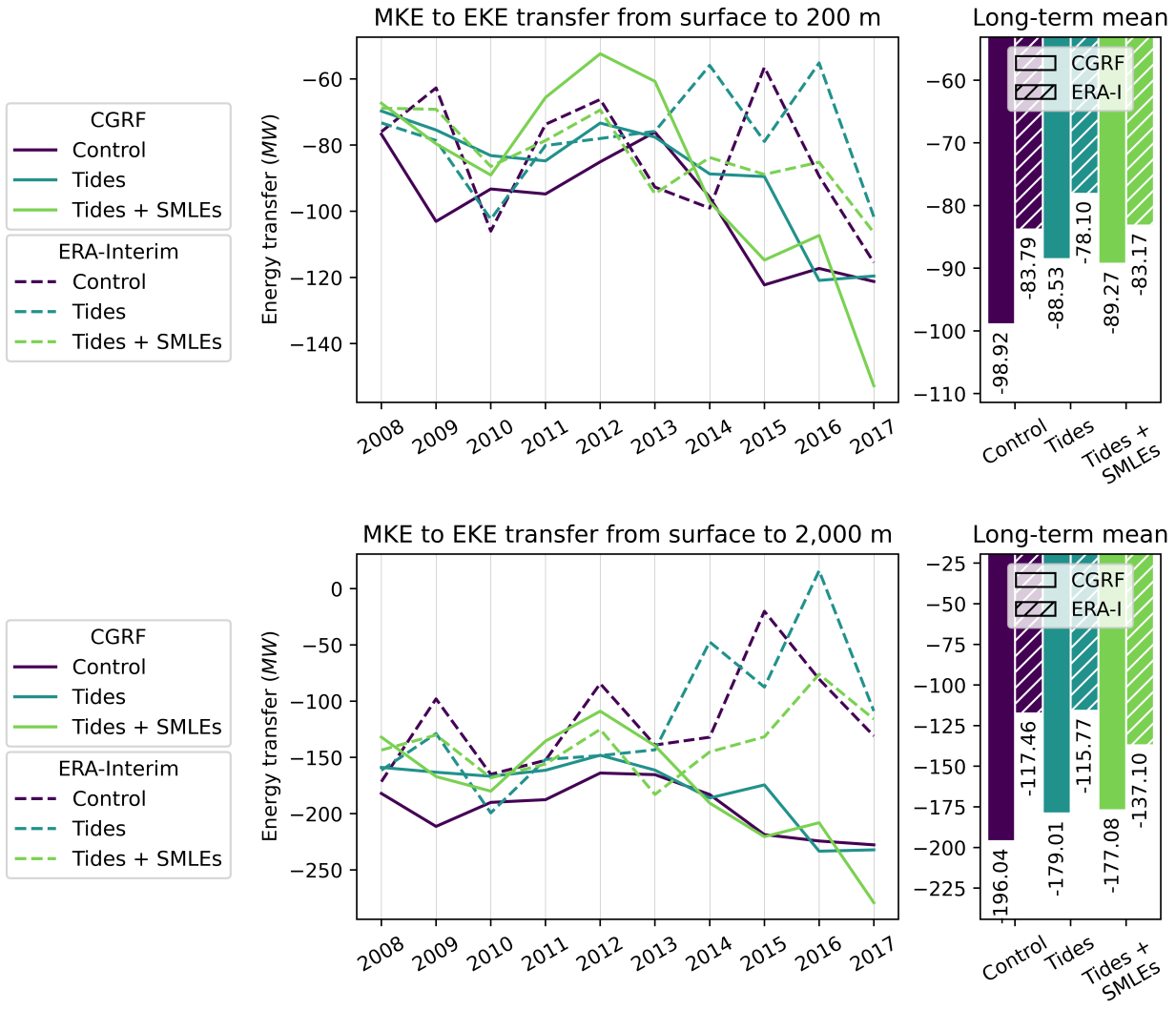

Figure 3.18: Energy transfer rates from mean kinetic energy to eddy kinetic energy (i.e., barotropic instabilitites) integrated within the Labrador Sea, from the surface to 200 m (**top**) and to 2,000 m (**bottom**). Yearly averages are defined from October to September.

Figure 3.15 is $>10^{11}$ W. Additionally, the median value of BT energy transfer is near 0, i.e., BTs are neither generated nor attenuated throughout most of the LS. The majority of the positive values are found around Cape Desolation, where highly barotropic IRs are generated. Elsewhere around the shelfbreak, BTs are only attenuated, and this effect is more pronounced in the CGRF-forced simulations than with ERA-I. BTs are also attenuated in the northern vicinity of Cape Desolation, implying that much of the BT generation in this region is dissipated locally. Considering the time-series in Figure 3.18, the BT energy transfer is almost entirely negative, implying that EKE is mostly being transferred into MKE rather than vice versa. Additionally, variability between years and runs is high, making it difficult to draw clear conclusions. However, it can be noted that the EKE to MKE transfer is stronger

in the CGRF-forced simulations, and this is consistent with the stronger eddy attenuation at the Labrador shelf in Figure 3.16.

A considerable shortcoming of this analysis is the horizontal resolution of our ANHA4 simulations. Both Rieck et al. (2019) and Gou et al. (2023) note that energy transfer rates are higher within higher resolution simulations. For this reason, we can expect to capture signatures of only the largest CEs and BCEs (which are mainly baroclinic and range in size from approximately 10 to 30 km) in our analysis of BCs. For context, Rieck et al. (2019) note that CE-driven EKE between 1,000 and 1,500 m depth dominates surface EKE in observations. This phenomenon is not replicated in Figure 3.14, which can be expected since the authors also note that a 1/12° simulation was similarly unable to resolve this behaviour.

Because IRs, which have a significant barotropic component, are larger than CEs and BCEs, it might be expected that ANHA4 would capture a higher portion of the BT energy transfer. However, both Rieck et al. (2019) and Gou et al. (2023) note similar rates of energy transfer between BCs and BTs (i.e., within an order of magnitude); the maximums in our maps are roughly 10^5 orders of magnitude apart, so we are therefore missing a large portion of the BTs that exist in reality. However, it is important to highlight that this is not per se a shortcoming in our analysis; it is likely moreso a feature of numerical models with low to medium resolutions.

3.6 Strength of the submesoscale mixed layer eddy parameterization

Within each cell of the model, the SMLE streamfunction is evaluated in $(\mathbf{i}, \mathbf{j})$ and saved to the model output. The streamfunction units are $m^2\ s^{-1}$, and advective tracer velocities are obtained by taking its curl, i.e., $\mathbf{u}^* = \nabla \times \mathbf{\Psi}$. In this section, we consider the scalar magnitude of the streamfunction output. Figure 3.19 shows the seasonal cycle of the streamfunction (green) on the left, along with six-year means from 2012 to 2017 on the right. The region considered is the full LS, including the boundary currents, because we are interested in the SMLEp's effects on both the shelfbreak front as well as around the convective patch. In the seasonal time-series, we also include the corresponding mean interior MLD over the same six-year period (black).

In both ERAI-TS (dashed) and CGRF-TS (solid), the MLD leads the streamfunction, with both peaking in March and subsequently returning to zero in mid-summer. This makes sense; $\mathbf{\Psi}$ is proportional to the product of the horizontal buoyancy gradient, the mixed layer

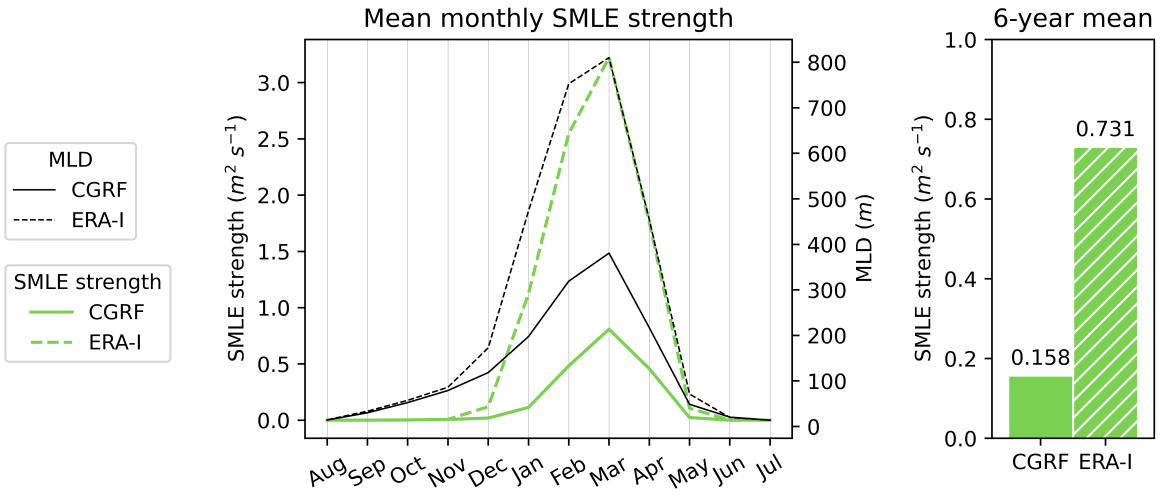

Figure 3.19: Strength of the SMLE parameterization, spatially-averaged throughout the full Labrador Sea (i.e., including the boundary currents). In the monthly time-series, for reference, we also plot spatially-averaged mixed layer depths in the interior only. A relatively short six-year period during 2012–2017 is analyzed due to computational constraints.

depth, and the inertial period, so it can only begin growing after the MLD has started to deepen.

Comparing ERAI-TS and CGRF-TS, the former experiences higher values of $\mathbf{\Psi}$, which is consistent with its deeper MLDs and larger convective patch. This difference is shown qualitatively in the maps of maximums in $\mathbf{\Psi}$ (Figure 3.20), in which ERAI-TS contains brighter yellows/greens and greater southward and eastward extents of the convective patch than CGRF-TS. More generally, these maps can also be compared with those of maximum MLDs in Figure 3.6. This reveals several interesting, although not unexpected, results. First, the highest values of $\mathbf{\Psi}$ are found around the north-western border of the convective patch, where MLDs rapidly shoal as they approach the continental shelf in the vicinity of the shelf-break front. In the south-east, MLDs shoal much more gradually, reducing the buoyancy gradient and thus leading to weaker values of $\mathbf{\Psi}$. Second, in all four maps of Figure 3.20, the regions of the deepest MLDs also experience reduced $\mathbf{\Psi}$ (represented visually as blue filaments surrounded by yellow/green). This is explained by the weak buoyancy gradients within the interior of the convective patch. Finally, it is also important to note the non-zero values of $\mathbf{\Psi}$ outside the formal deep convection patch (i.e., where MLD $>$ 1,000 m). For example, signatures of the inner coastal current on the Labrador Shelf can be seen in all four maps. This indicates that, although $\mathbf{\Psi}$ is maximized around the perimeter of the convective patch, it is also having an effect over the shelves and likely on the shelfbreak front as well.

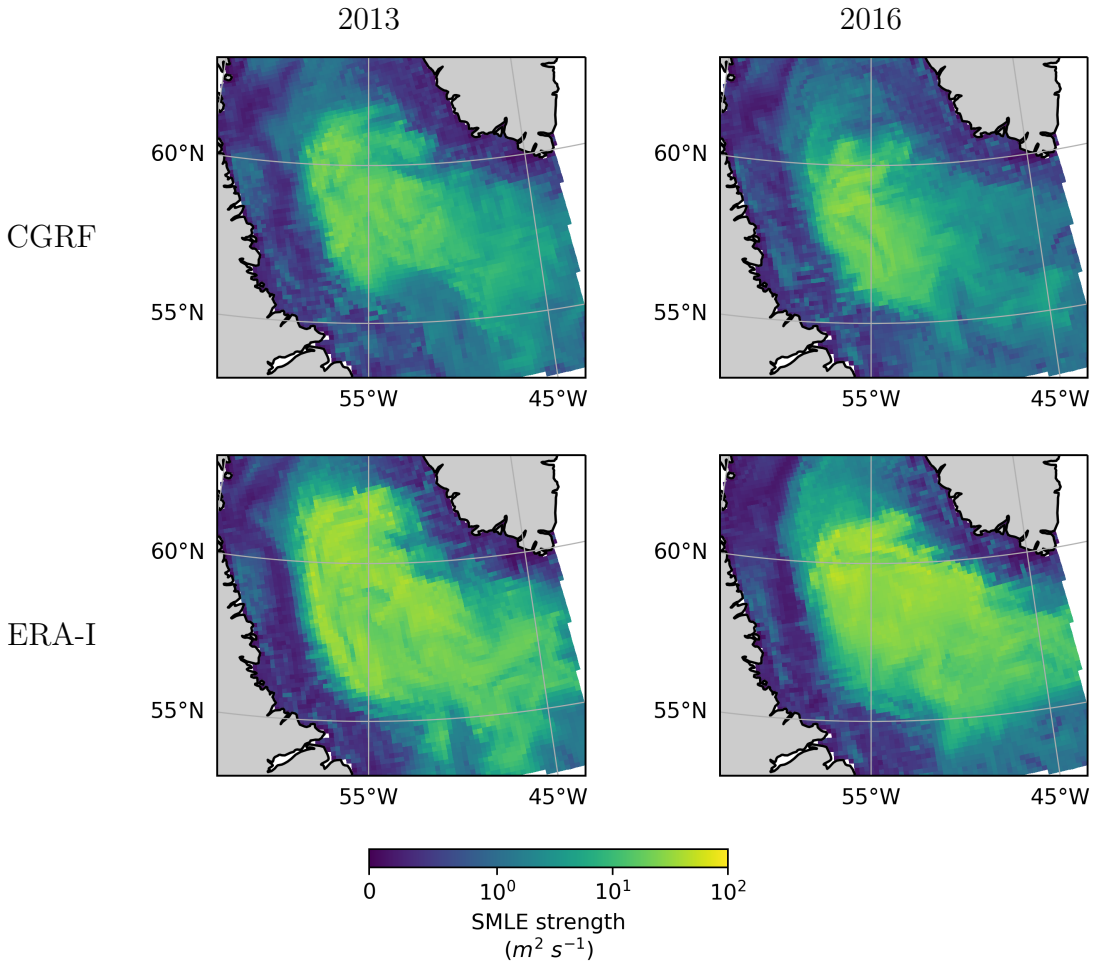

Figure 3.20: Maps of yearly maximums in SMLE flux within the water column during 2013 and 2016, defined from October to September. The colour scale is linear from 0 to 10^0 and logarithmic elsewhere.

3.7 Oxygen and carbon content

Deep convection in the LS represents an important pathway for oxygen and CO_2 to enter the abyssal ocean (Courtois et al., 2020), and observations suggest that 30% of the ventilation in the subpolar NA takes place in this region (Rhein et al., 2017). Within the broader context of the AMOC, which accounts for 41% of the global air-sea CO_2 flux (Lozier, 2023), the consensus that it will most likely weaken over the next century (Lee et al., 2023) means changes can also be expected to affect ventilation in the LS. The ultimate justification for this study is how tidal forcing and the SMLEp affect deep convection, and hence how they might be used in global coupled climate models to improve their accuracy. So, while our focus is not biogeochemistry, we include here a short discussion about oxygen and carbon concentrations, since it is relevant to the coupled climate modelling community.

Carbon and oxygen concentrations are estimated using the BLING biogeochemistry model coupled to ANHA4. Figure 3.21 shows average concentrations of both carbon (top panel) and oxygen (bottom panel) in the top 2,000 m of the interior LS. In both panels, high-frequency variability is low, so no time-averages are taken. Comparing the CGRF-forced simulations with the ERA-I simulations, concentrations in the latter are higher. This is consistent with the stronger forcing and convection, and hence ventilation, associated with the ERA-I product.

Although it is out of scope to attempt to explain the long-term variability, it is noteworthy that the carbon and oxygen concentrations do not follow the same multi-year trends. In other words, oxygen concentrations increase and decrease over time, whereas carbon concentrations ostensibly experience a steady increase. The general shape of the oxygen concentrations is consistent with the strength of the atmospheric forcing and the winter convection, with decreased concentrations during years of weak convection (2010–2013) and increased concentrations in years of stronger convection (2008–2009, 2014–2016). Conversely, carbon concentrations appear to experience no such variability.

Considering the 10-year means, the effects of tidal forcing and the SMLEp are in both cases to decrease oxygen concentrations. As with the time-series, the oxygen concentration means follow the same pattern as the MLD (i.e., Figures 3.5 and 3.8), suggesting a dominance of the strength of deep convection rather than lateral boundary-interior fluxes. Conversely, the carbon concentration means do not follow this pattern. Instead, tidal forcing increases the mean carbon concentrations in both CGRF-T and ERAI-T, whereas the SMLEp has a diverging effect, decreasing the concentration in CGRF-TS while having little effect in ERAI-TS. This is similar to the fluxes, which also experience a pattern where tidal forcing has the

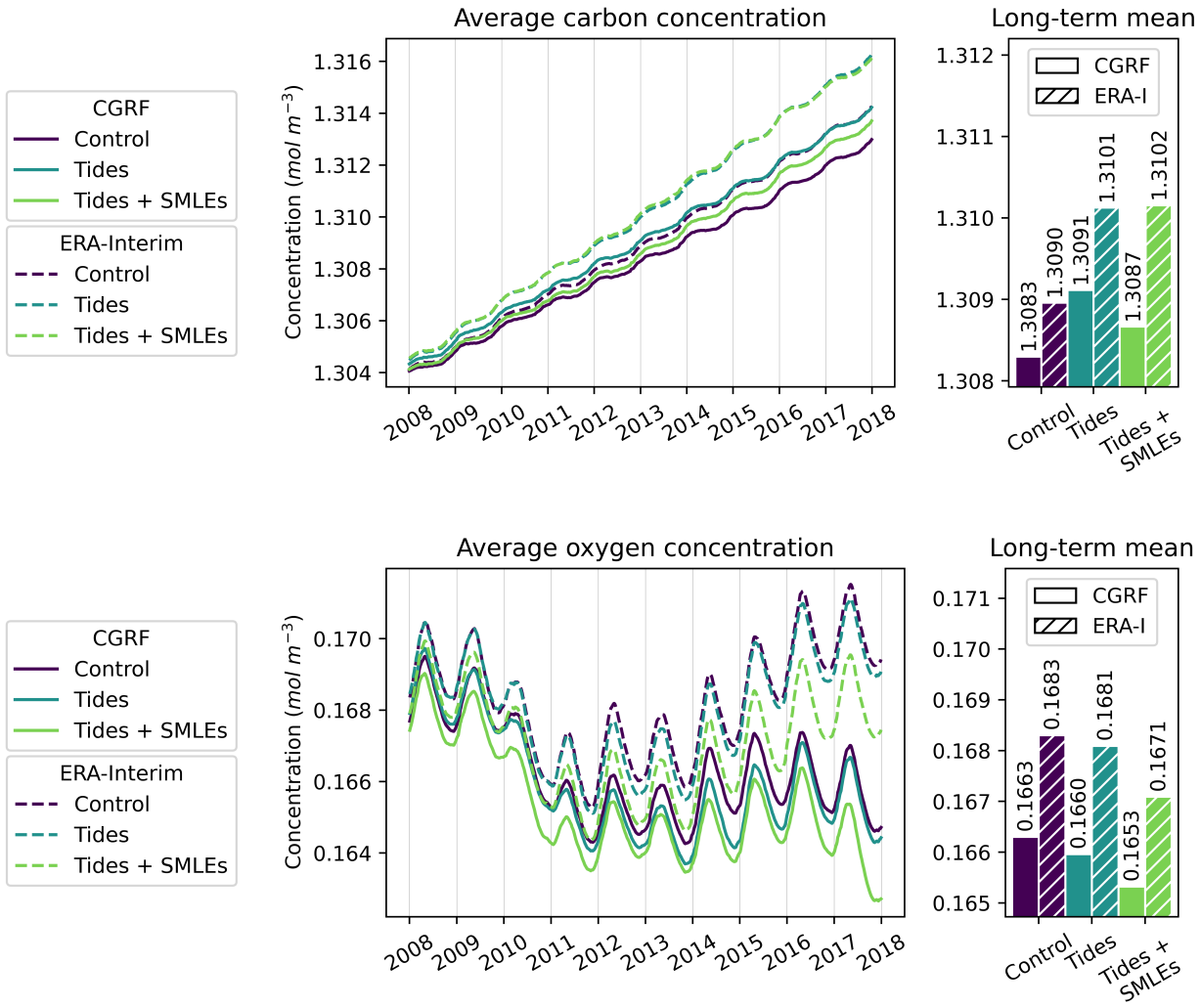

Figure 3.21: Oxygen and carbon contents in the top 2,000 m of the interior Labrador Sea.

same effect in both CGRF-T and ERAI-T but the SMLEp only has an effect in CGRF-TS and not in ERAI-TS. It is therefore possible that the steady carbon drift in the time-series is masking year-to-year variability that would otherwise correlate with the fluxes.

Chapter 4

Discussion and conclusion

We have evaluated the effects of tidal forcing and the SMLEp on deep convection in the LS by employing six atmospherically-forced NEMO simulations. Three simulations use CGRF atmospheric forcing, while the remaining three use ERA-I. For each set of three, one run has both tidal forcing and the SMLEp activated, a second run as only tidal forcing, and a third control run has neither. The mean current system in all simulations compares well with observations, although the medium horizontal resolution of 1/4° prevents the model from capturing small scale features like the WGCC. The mean hydrography is similarly realistic, with the caveat that our simulations appear to have a shallower and saltier (>35.00 PSU) layer of mid-depth water, likely associated with the well-documented salinity drift phenomenon commonly experienced by numerical ocean models (Rattan et al., 2010).

Both tidal forcing and the SMLEp increase convective resistance and reduce the strength of winter deep convection. The reduction in strength is diagnosed in two ways, firstly by using the mean winter MLDs within the interior LS (defined wherever depth is greater than 3,000 m), and secondly by using the mean winter convective volume (defined here as the volume of the mixed layer where the MLD is deeper than 1,000 m). In the former analysis, we are also able to compare our model MLDs with those from Argo float data as well as from a 1/60° nested model encompassing the LS. Taken together, the mean MLDs and convective volumes indicate that the deep biases present in the control runs are reduced by both tidal forcing and the SMLEp for both atmospheric forcing products. Specifically, relative to the biases between the mean MLDs of the control runs and the mean Argo MLD, tidal forcing alone reduced the bias by 24.5% (6.5%) using CGRF (ERA-I), while tidal forcing and the SMLEp reduced bias by 86.1% (46.9%) using CGRF (ERA-I). Part of reason for the smaller bias reduction in the ERA-I simulations is that they experience much stronger convection in general, most likely due to stronger atmospheric forcing (see Figure 3.11). And hence, the

percent reductions in MLD appear smaller.

The specific mechanisms by which tidal forcing and the SMLEp reduce deep convection are varied and require nuance. Below, we present some concluding observations about both.

The SMLEp:

- In ERAI-TS, the SMLEp does not strongly affect freshwater and heat fluxes, nor does it affect freshwater and heat contents. Conversely, it does affect the fluxes and contents in CGRF-TS. Since ERAI-TS and CGRF-TS both experience strongly decreased winter MLDs and convective volumes, the primary effect of the SMLEp must be to slump isopycnals during post-convection restratification, thereby reducing pre-conditioning during the following autumn, rather than to cause increased buoyancy flux into the interior LS.
- However, the relatively stronger bias reduction in CGRF-TS MLDs and the similarly strong reduction in convective volume might indicate that the altered fluxes also play a minor/secondary role in inhibiting deep convection. This is supported by our maps of SMLEp strength, which exhibit non-zero values over the continental shelves and around the shelfbreak, implying active cross-front tracer advection in the boundary currents. If we consider CGRF-TS's heat content and fluxes over time, we see a discrepancy between the mean surface export (53.76 TW) and lateral import (57.96 TW), and this leads to a significant year-on-year build-up of (stratifying) heat below the surface 200 m. Paradoxically, the SMLEp also causes a non-negligible decrease in lateral freshwater import, which would have a destratifying effect (variability in the surface freshwater fluxes is relatively minor and therefore neglected).
- Because our initial estimates of heat and freshwater fluxes are measured relative to arbitrary reference values, and because we do not estimate volume fluxes, it is difficult to conclude whether the SMLEp in CGRF-TS is causing an increased import of warm and salty water, a decreased import of cold and fresh water, or some combination of both. However, based on our estimations of the MAPE to EAPE transfer, there is an implied reduction in baroclinic instabilities both at the surface and at depth. It therefore seems reasonable that the altered fluxes are related to a net reduction in the import of water that is, on average, cold and fresh.
- The different behaviour of the SMLEp in ERAI-TS and CGRF-TS is challenging to explain; ERAI-TS experiences a similar reduction in baroclinic instabilities but no substantial changes in lateral fluxes, FWC, or heat content. In general, boundary-interior exchange is driven by eddies or wind transport; since we have controlled for the wind, it is possible that barotropic eddy attenuation (which is relatively much stronger

in ERAI-TS) is counteracting the reduction in baroclinic instabilities. However, this seems unlikely, in large part because the rate of MKE to EKE transfer is much smaller than that of MAPE to EAPE, implying that our 1/4° resolution is failing to capture a sufficient portion of the expected barotropic instabilities.

Tidal forcing:

- Unlike with the SMLEp, tidal forcing has the same effect with both ERA-I and CGRF forcing. Namely, it increases FWC and reduces heat content, both in the surface and at depth, while increasing the lateral freshwater import and decreasing the lateral heat import.
- The MAPE to EAPE and MKE to EKE transfer rates, which tidal forcing generally affects more strongly at the surface than at depth, indicate that the altered boundary-interior exchange might be related to changes in the near-surface lateral fluxes. As in the case of the SMLEp, we are unable to confirm if this is causing a net increase in cold and fresh import or a net decrease in warm and salty import. However, since the surface of the boundary currents is typically characterized by the former, this is a strong possibility.
- We are also unable to say if the principal stratifying effect is due to internal tides changing the vertical diffusivities, which could affect diapycnal mixing both in the interior LS and along the boundary currents, or if it is related to some other effect such as the barotropic tide inducing increased cross-shelf mixing.

A potential contradiction exists between the buoyancy fluxes in CGRF-TS and the tidally-forced simulations. Specifically, the increased lateral heat import and decreased lateral freshwater import in CGRF-TS appears to ultimately increase stratification. Conversely, the tidally-forced runs experience decreased lateral heat import and increased lateral freshwater transport, which surprisingly also increases stratification. This difference might be explained by the spatial distribution of the buoyancy fluxes. For example, if the tidal forcing increases near-surface fluxes of cold and fresh Arctic-origin water but the SMLEp increases fluxes of warm and salty Irminger water at depth.

Going forward, these possibilities could be investigated by directly calculating the lateral buoyancy fluxes, rather than inferring them from the surface fluxes, which would clarify where (i.e., where along the shelfbreak as well as where in depth) and how fluxes are being affected. In combination with analyses of the available potential energy, this would also clarify the portion(s) of the stratification from boundary-interior exchange versus interior-only dynamics. Ideally, this would also be paired with estimates of the effective vertical diffusivities, which would reveal whether the principal effect of tidal forcing is to increase/decrease

vertical mixing or another process like altering the cross-shelf exchange.

Regardless, our main result is that both tidal forcing and the SMLEp reduce the strength of deep convection and thereby reduce deep wintertime MLD biases in the LS. We consider this a robust result, since it is observed in both the CGRF-forced simulations and the ERA-I simulations. One outcome of these changes is a reduction in the ventilation of the LS, which experiences decreases in oxygen content with both tidal forcing and the SMLEp. The effects on carbon concentration are less consistent, implying that carbon contents are modulated by lateral fluxes rather than just the strength of the deep convection.

These results lead us to conclude that tidal forcing and the SMLEp are valid tools for improving MLDs in medium-resolution OGCMs with unrealistically deep convection. And since this is a noted issue within global coupled climate models, we therefore recommend that climate modellers consider employing tidal forcing and the SMLEp in their future models.

References

Adcroft, A., Campin, J.-M., Doddridge, E., Dutkiewicz, S., Evangelinos, C., Ferreira, D., ... others (2018). Mitgcm documentation. *Release checkpoint67a-12-gbf23121*, *19*.

Arbic, B. K. (2022). Incorporating tides and internal gravity waves within global ocean general circulation models: A review. *Progress in Oceanography*, *206*, 102824.

Assene, F., Koch-Larrouy, A., Dadou, I., Tchilibou, M., Morvan, G., Chanut, J., ... Tran, T.-K. (2023). Internal tides off the amazon shelf part i: importance for the structuring of ocean temperature during two contrasted seasons. *EGUsphere*, *2023*, 1–46.

Bamber, J., Tedstone, A., King, M., Howat, I., Enderlin, E., Van Den Broeke, M., & Noel, B. (2018). Land ice freshwater budget of the arctic and north atlantic oceans: 1. data, methods, and results. *Journal of Geophysical Research: Oceans*, *123*(3), 1827–1837.

Beaupré-Laperrière, A., Mucci, A., & Thomas, H. (2020). The recent state and variability of the carbonate system of the canadian arctic archipelago and adjacent basins in the context of ocean acidification. *Biogeosciences*, *17*(14), 3923–3942.

Bennetts, L. G., Shakespeare, C. J., Vreugdenhil, C. A., Foppert, A., Gayen, B., Meyer, A., ... others (2023). Closing the loops on southern ocean dynamics: From the circumpolar current to ice shelves and from bottom mixing to surface waves. *Authorea Preprints*.

Bodner, A. S., Fox-Kemper, B., Johnson, L., Van Roekel, L. P., McWilliams, J. C., Sullivan, P. P., ... Dong, J. (2023). Modifying the mixed layer eddy parameterization to include frontogenesis arrest by boundary layer turbulence. *Journal of Physical Oceanography*, *53*(1), 323–339.

Bower, A., Lozier, S., Biastoch, A., Drouin, K., Foukal, N., Furey, H., ... Zou, S. (2019). Lagrangian views of the pathways of the atlantic meridional overturning circulation. *Journal of Geophysical Research: Oceans*, *124*(8), 5313–5335.

Bryan, K. (1969). A numerical method for the study of the circulation of the world ocean. *Journal of Computational Physics*, *4*(3), 347-376.

Buckley, M. W., & Marshall, J. (2016). Observations, inferences, and mechanisms of the atlantic meridional overturning circulation: A review. *Reviews of Geophysics*, *54*(1), 5–63.

Calvert, D., Nurser, G., Bell, M. J., & Fox-Kemper, B. (2020). The impact of a parameterization of submesoscale mixed layer eddies on mixed layer depths in the nemo ocean model. *Ocean Modelling*, *154*, 101678.

Carmack, E. C. (2007). The alpha/beta ocean distinction: A perspective on freshwater fluxes, convection, nutrients and productivity in high-latitude seas. *Deep Sea Research Part II: Topical Studies in Oceanography*, *54*(23-26), 2578–2598.

Cartwright, D. E. (1977). Oceanic tides. *Reports on Progress in Physics*, *40*(6), 665.

Chanut, J., Barnier, B., Large, W., Debreu, L., Penduff, T., Molines, J. M., & Mathiot, P. (2008). Mesoscale eddies in the labrador sea and their contribution to convection and restratification. *Journal of Physical Oceanography*, *38*(8), 1617–1643.

Courtois, P., Garcia-Quintana, Y., Hu, X., & Myers, P. G. (2020). Kinematic subduction rate of labrador sea water from an eddy-permitting numerical model. *Journal of Geophysical Research: Oceans*, *125*(7), e2019JC015475.

Courtois, P., Hu, X., Pennelly, C., Spence, P., & Myers, P. G. (2017). Mixed layer depth calculation in deep convection regions in ocean numerical models. *Ocean Modelling*, *120*, 60–78.

Dai, A., Qian, T., Trenberth, K. E., & Milliman, J. D. (2009). Changes in continental freshwater discharge from 1948 to 2004. *Journal of climate*, *22*(10), 2773–2792.

Dee, D. P., Uppala, S. M., Simmons, A. J., Berrisford, P., Poli, P., Kobayashi, S., ... others (2011). The era-interim reanalysis: Configuration and performance of the data assimilation system. *Quarterly Journal of the royal meteorological society*, *137*(656), 553–597.

De Jong, M., Bower, A., & Furey, H. (2016). Seasonal and interannual variations of irminger ring formation and boundary–interior heat exchange in flame. *Journal of Physical Oceanography*, *46*(6), 1717–1734.

Dengler, M., Fischer, J., Schott, F. A., & Zantopp, R. (2006). Deep labrador current and its variability in 1996–2005. *Geophysical Research Letters*, *33*(21).

Ditlevsen, P., & Ditlevsen, S. (2023). Warning of a forthcoming collapse of the atlantic meridional overturning circulation. *Nature Communications*, *14*(1), 1–12.

Dussin, R., Barnier, B., Brodeau, L., & Molines, J. M. (2016). Drakkar forcing set dfs5. *MyOcean Report*.

Egbert, G. D., & Ray, R. D. (2003). Semi-diurnal and diurnal tidal dissipation from topex/poseidon altimetry. *Geophysical Research Letters*, *30*(17).

Fennel, K., Mattern, J. P., Doney, S. C., Bopp, L., Moore, A. M., Wang, B., & Yu, L. (2022). Ocean biogeochemical modelling. *Nature Reviews Methods Primers*, *2*(1), 76.

Fichefet, T., & Maqueda, M. M. (1997). Sensitivity of a global sea ice model to the treatment of ice thermodynamics and dynamics. *Journal of Geophysical Research: Oceans*, *102*(C6), 12609–12646.

Fischer, J., Visbeck, M., Zantopp, R., & Nunes, N. (2010). Interannual to decadal variability of outflow from the labrador sea. *Geophysical Research Letters*, *37*(24).

Fox-Kemper, B., Danabasoglu, G., Ferrari, R., Griffies, S., Hallberg, R., Holland, M., ... Samuels, B. (2011). Parameterization of mixed layer eddies. iii: Implementation and impact in global ocean climate simulations. *Ocean Modelling*, *39*(1-2), 61–78.

Fox-Kemper, B., & Ferrari, R. (2008). Parameterization of mixed layer eddies. part ii: Prognosis and impact. *Journal of Physical Oceanography*, *38*(6), 1166–1179.

Fox-Kemper, B., Ferrari, R., & Hallberg, R. (2008). Parameterization of mixed layer eddies. part i: Theory and diagnosis. *Journal of Physical Oceanography*, *38*(6), 1145–1165.

Frajka-Williams, E., Rhines, P. B., & Eriksen, C. C. (2014). Horizontal stratification during deep convection in the labrador sea. *Journal of physical oceanography*, *44*(1), 220–228.

Fratantoni, P. S., & McCartney, M. S. (2010). Freshwater export from the labrador current to the north atlantic current at the tail of the grand banks of newfoundland. *Deep Sea Research Part I: Oceanographic Research Papers*, *57*(2), 258–283.

Fratantoni, P. S., & Pickart, R. S. (2007). The western north atlantic shelfbreak current system in summer. *Journal of Physical Oceanography*, *37*(10), 2509–2533.

Furner, R., Williams, J., Horsburgh, K., & Saulter, A. (2016). Nemo-surge: Setting up an accurate tidal model. *Forecasting Research Technical Report No. FRTR610*.

Galbraith, E. D., Gnanadesikan, A., Dunne, J. P., & Hiscock, M. R. (2010). Regional impacts of iron-light colimitation in a global biogeochemical model. *Biogeosciences*, *7*(3), 1043–1064.

Garcia-Quintana, Y., Courtois, P., Hu, X., Pennelly, C., Kieke, D., & Myers, P. G. (2019). Sensitivity of labrador sea water formation to changes in model resolution, atmospheric forcing, and freshwater input. *Journal of Geophysical Research: Oceans*, *124*(3), 2126–2152.

Garrett, C., & Kunze, E. (2007). Internal tide generation in the deep ocean. *Annu. Rev. Fluid Mech.*, *39*, 57–87.

Gary, S. F., Lozier, M. S., Biastoch, A., & Böning, C. W. (2012). Reconciling tracer and float observations of the export pathways of labrador sea water. *Geophysical Research Letters*, *39*(24).

Gent, P. R., & McWilliams, J. C. (1990). Isopycnal mixing in ocean circulation models. *Journal of Physical Oceanography*, *20*(1), 150–155.

Gillard, L. C., Pennelly, C., Johnson, H. L., & Myers, P. G. (2022). The effects of atmospheric and lateral buoyancy fluxes on labrador sea mixed layer depth. *Ocean Modelling*, *171*, 101974.

Gou, R., Li, P., Wiegand, K. N., Pennelly, C., Kieke, D., & Myers, P. G. (2023). Variability of eddy formation off the west greenland coast from a 1/60° model. *Journal of Physical Oceanography*, *53*(10), 2475–2490.

Gou, R., Pennelly, C., & Myers, P. G. (2022). The changing behavior of the west greenland current system in a very high-resolution model. *Journal of Geophysical Research: Oceans*, *127*(8).

Griffies, S. M., et al. (2012). Elements of the modular ocean model (mom). *GFDL Ocean Group Tech. Rep*, *7*(620), 47.

Griffiths, S. D., & Hill, D. F. (2015). Tidal modeling. *Handbook of Sea-Level Research*, 438–451.

Hall, M. M., Torres, D. J., & Yashayaev, I. (2013). Absolute velocity along the ar7w section in the labrador sea. *Deep Sea Research Part I: Oceanographic Research Papers*, *72*, 72–87.

Hamilton, L. C., Wirsing, J., & Saito, K. (2018). Demographic variation and change in the inuit arctic. *Environmental Research Letters*, *13*(11), 115007.

Hewitt, H. T., Roberts, M., Mathiot, P., Biastoch, A., Blockley, E., Chassignet, E. P., ... others (2020). Resolving and parameterizing the ocean mesoscale in earth system models. *Current Climate Change Reports*, *6*, 137–152.

Hirschi, J. J.-M., Barnier, B., Böning, C., Biastoch, A., Blaker, A. T., Coward, A., ... others (2020). The atlantic meridional overturning circulation in high-resolution models. *Journal of Geophysical Research: Oceans*, *125*(4), e2019JC015522.

Holte, J., & Talley, L. (2009). A new algorithm for finding mixed layer depths with applications to argo data and subantarctic mode water formation. *Journal of Atmospheric and Oceanic Technology*, *26*(9), 1920–1939.

Holte, J., Talley, L. D., Gilson, J., & Roemmich, D. (2017). An argo mixed layer climatology and database. *Geophysical Research Letters*, *44*(11), 5618–5626.

Hu, X., Sun, J., Chan, T. O., & Myers, P. G. (2018). Thermodynamic and dynamic ice thickness contributions in the canadian arctic archipelago in nemo-lim2 numerical simulations. *The Cryosphere*, *12*(4), 1233–1247.

Johns, W. E., Baringer, M. O., Beal, L., Cunningham, S., Kanzow, T., Bryden, H. L., ... others (2011). Continuous, array-based estimates of atlantic ocean heat transport at 26.5 n. *Journal of Climate*, *24*(10), 2429–2449.

Karsten, R. H., McMillan, J., Lickley, M., & Haynes, R. (2008). Assessment of tidal current energy in the minas passage, bay of fundy. *Proceedings of the Institution of Mechanical Engineers, Part A: Journal of Power and Energy*, *222*(5), 493–507.

Kieke, D., Klein, B., Stramma, L., Rhein, M., & Koltermann, K. P. (2009). Variability and propagation of labrador sea water in the southern subpolar north atlantic. *Deep Sea Research Part I: Oceanographic Research Papers*, *56*(10), 1656–1674.

Kieke, D., Rhein, M., Stramma, L., Smethie, W. M., Bullister, J. L., & LeBel, D. A. (2007). Changes in the pool of labrador sea water in the subpolar north atlantic. *Geophysical Research Letters*, *34*(6).

Lab Sea Group. (1998). The labrador sea deep convection experiment. *Bulletin of the American Meteorological Society*, *79*(10), 2033–2058.

Large, W., & Yeager, S. (2009). The global climatology of an interannually varying air–sea flux data set. *Climate dynamics*, *33*, 341–364.

Large, W. B. (2006). Surface fluxes for practitioners of global ocean data assimilation. *Ocean weather forecasting: An integrated view of oceanography*, 229–270.

Lazier, J. R., & Wright, D. G. (1993). Annual velocity variations in the labrador current. *Journal of Physical Oceanography*, *23*(4), 659–678.

Leclair, M., & Madec, G. (2009). A conservative leapfrog time stepping method. *Ocean Modelling*, *30*(2-3), 88–94.

Lee, H., Calvin, K., Dasgupta, D., Krinner, G., Mukherji, A., Thorne, P., ... others (2023). Climate change 2023: Synthesis report. contribution of working groups i, ii and iii to the sixth assessment report of the intergovernmental panel on climate change.

Lenton, T. M., Held, H., Kriegler, E., Hall, J. W., Lucht, W., Rahmstorf, S., & Schellnhuber, H. J. (2008). Tipping elements in the earth's climate system. *Proceedings of the national Academy of Sciences*, *105*(6), 1786–1793.

Lindström, G., Pers, C., Rosberg, J., Strömqvist, J., & Arheimer, B. (2010). Development and testing of the hype (hydrological predictions for the environment) water quality model for different spatial scales. *Hydrology research*, *41*(3-4), 295–319.

Lozier, M. S. (2023). Overturning in the subpolar north atlantic: a review. *Philosophical Transactions of the Royal Society A*, *381*(2262), 20220191.

Lozier, M. S., Li, F., Bacon, S., Bahr, F., Bower, A. S., Cunningham, S., ... others (2019). A sea change in our view of overturning in the subpolar north atlantic. *Science*, *363*(6426), 516–521.

Lyard, F. H., Allain, D. J., Cancet, M., Carrère, L., & Picot, N. (2021). Fes2014 global ocean tide atlas: design and performance. *Ocean Science*, *17*(3), 615–649.

Madec, G., Bell, M., & Bourdallé-Badie, R. (2022). Nemo ocean engine version 4.2.0 [Computer software manual]. 11 Bd d'Alembert, 78280 Guyancourt, France.

Madec, G., Bourdallé-Badie, R., Bouttier, P.-A., Bricaud, C., Bruciaferri, D., Calvert, D., ... others (2017). Nemo ocean engine.

Madec, G., Delecluse, P., Imbard, M., & Levy, C. (1997). Ocean general circulation model reference manual. *Note du Pôle de modélisation*.

Manabe, S., & Bryan, K. (1969). Climate calculations with a combined ocean-atmosphere model. *J. atmos. Sci*, *26*(4), 786–789.

Marshall, J., & Schott, F. (1999). Open-ocean convection: Observations, theory, and models. *Reviews of geophysics*, *37*(1), 1–64.

Masina, S., Storto, A., Ferry, N., Valdivieso, M., Haines, K., Balmaseda, M., ... Parent, L. (2017). An ensemble of eddy-permitting global ocean reanalyzes from the myocean project. *Climate Dynamics*, *49*, 813–841.

McCarthy, G. D., Brown, P. J., Flagg, C. N., Goni, G., Houpert, L., Hughes, C. W., ... others (2020). Sustainable observations of the amoc: Methodology and technology. *Reviews of Geophysics*, *58*(1), e2019RG000654.

Megann, A. (2024). Quantifying numerical mixing in a tidally forced global eddy-permitting ocean model. *Ocean Modelling*, *188*, 102329.

Menary, M. B., Jackson, L. C., & Lozier, M. S. (2020). Reconciling the relationship between the amoc and labrador sea in osnap observations and climate models. *Geophysical Research Letters*, *47*(18), e2020GL089793.

Morison, J., Kwok, R., Peralta-Ferriz, C., Alkire, M., Rigor, I., Andersen, R., & Steele, M. (2012). Changing arctic ocean freshwater pathways. *Nature*, *481*(7379), 66–70.

Morrison, A., Hogg, A. M., England, M. H., & Spence, P. (2020). Warm circumpolar deep water transport toward antarctica driven by local dense water export in canyons. *Science Advances*, *6*(18), eaav2516.

Munk, W., & Wunsch, C. (1998). Abyssal recipes ii: Energetics of tidal and wind mixing. *Deep Sea Research Part I: Oceanographic Research Papers*, *45*(12), 1977–2010.

Myers, P. G. (2005). Impact of freshwater from the canadian arctic archipelago on labrador sea water formation. *Geophysical Research Letters*, *32*(6).

Myers, P. G., Donnelly, C., & Ribergaard, M. H. (2009). Structure and variability of the west greenland current in summer derived from 6 repeat standard sections. *Progress in Oceanography*, *80*(1-2), 93–112.

Naughten, K. A., Holland, P. R., & De Rydt, J. (2023). Unavoidable future increase in west antarctic ice-shelf melting over the twenty-first century. *Nature Climate Change*, 1–7.

Paquin, J.-P., Lu, Y., Taylor, S., Blanken, H., Marcotte, G., Hu, X., ... others (2020). High-resolution modelling of a coastal harbour in the presence of strong tides and significant river runoff. *Ocean Dynamics*, *70*, 365–385.

Pennelly, C., & Myers, P. G. (2020). Introducing lab60: A 1/ 60° nemo 3.6 numerical simulation of the labrador sea. *Geoscientific Model Development*, *13*(10), 4959–4975.

Pennelly, C., & Myers, P. G. (2022). Tracking irminger rings' properties using a submesoscale ocean model. *Progress in Oceanography*, *201*, 102735.

Petit, T., Lozier, M., Rühs, S., Handmann, P., & Biastoch, A. (2023). Propagation and transformation of upper north atlantic deep water from the subpolar gyre to 26.5° n. *Journal of Geophysical Research: Oceans*, e2023JC019726.

Pörtner, H.-O., Roberts, D. C., Masson-Delmotte, V., Zhai, P., Tignor, M., Poloczanska, E., & Weyer, N. (2019). The ocean and cryosphere in a changing climate. *IPCC Special Report on the Ocean and Cryosphere in a Changing Climate*.

Purich, A., & Doddridge, E. W. (2023). Record low antarctic sea ice coverage indicates a new sea ice state. *Communications Earth & Environment*, *4*(1), 314.

Rackow, T., Sein, D. V., Semmler, T., Danilov, S., Koldunov, N. V., Sidorenko, D., ... Jung, T. (2019). Sensitivity of deep ocean biases to horizontal resolution in prototype cmip6 simulations with awi-cm1. 0. *Geoscientific Model Development*, *12*(7), 2635–2656.

Rattan, S., Myers, P. G., Treguier, A.-M., Theetten, S., Biastoch, A., & Böning, C. (2010). Towards an understanding of labrador sea salinity drift in eddy-permitting simulations. *Ocean Modelling*, *35*(1-2), 77–88.

Rhein, M., Kieke, D., & Steinfeldt, R. (2015). Advection of north atlantic deep water from the labrador sea to the southern hemisphere. *Journal of Geophysical Research: Oceans*, *120*(4), 2471–2487.

Rhein, M., Steinfeldt, R., Kieke, D., Stendardo, I., & Yashayaev, I. (2017). Ventilation variability of labrador sea water and its impact on oxygen and anthropogenic carbon: a review. *Philosophical Transactions of the Royal Society A: Mathematical, Physical and Engineering Sciences*, *375*(2102), 20160321.

Richaud, B., Hu, X., Darmaraki, S., Fennel, K., Lu, Y., & Oliver, E. C. (2024). Drivers of marine heatwaves in the arctic ocean. *Journal of Geophysical Research: Oceans*, *129*(2), e2023JC020324.

Rieck, J. K., Böning, C. W., & Getzlaff, K. (2019). The nature of eddy kinetic energy in the labrador sea: Different types of mesoscale eddies, their temporal variability, and impact on deep convection. *Journal of Physical Oceanography*, *49*(8), 2075–2094.

Rühs, S., Oliver, E. C., Biastoch, A., Böning, C. W., Dowd, M., Getzlaff, K., ... Myers, P. G. (2021). Changing spatial patterns of deep convection in the subpolar north atlantic. *Journal of Geophysical Research: Oceans*, *126*(7), e2021JC017245.

Rykova, T., Straneo, F., & Bower, A. S. (2015). Seasonal and interannual variability of the west greenland current system in the labrador sea in 1993–2008. *Journal of Geophysical Research: Oceans*, *120*(2), 1318–1332.

Smith, G. C., Roy, F., Mann, P., Dupont, F., Brasnett, B., Lemieux, J.-F., ... Belair, S. (2014). A new atmospheric dataset for forcing ice–ocean models: Evaluation of reforecasts using the canadian global deterministic prediction system. *Quarterly Journal of the Royal Meteorological Society*, *140*(680), 881–894.

Stepanov, V. N., & Hughes, C. W. (2004). Parameterization of ocean self-attraction and loading in numerical models of the ocean circulation. *Journal of Geophysical Research: Oceans*, *109*(C3).

Stewart, R. H. (2003). Introduction to physical oceanography, pdf version. *Dept. Of Oceanography. Texas A & M University*.

Von Storch, J.-S., Eden, C., Fast, I., Haak, H., Hernández-Deckers, D., Maier-Reimer, E., ... Stammer, D. (2012). An estimate of the lorenz energy cycle for the world ocean based on the storm/ncep simulation. *Journal of physical oceanography*, *42*(12), 2185–2205.

Wang, Q., Danilov, S., Sidorenko, D., Timmermann, R., Wekerle, C., Wang, X., ... Schröter, J. (2014). The finite element sea ice-ocean model (fesom) v. 1.4: formulation of an ocean general circulation model. *Geoscientific Model Development*, *7*(2), 663–693.

Yashayaev, I. (2024). Intensification and shutdown of deep convection in the labrador sea were caused by changes in atmospheric and freshwater dynamics. *Communications Earth & Environment*, *5*(1), 156.

Yashayaev, I., & Loder, J. W. (2016). Recurrent replenishment of labrador sea water and associated decadal-scale variability. *Journal of Geophysical Research: Oceans*, *121*(11), 8095–8114.

Yeager, S., Castruccio, F., Chang, P., Danabasoglu, G., Maroon, E., Small, J., ... Zhang, S. (2021). An outsized role for the labrador sea in the multidecadal variability of the atlantic overturning circulation. *Science Advances*, *7*(41), 1–14.

Zhang, J., Weijer, W., Steele, M., Cheng, W., Verma, T., & Veneziani, M. (2021). Labrador sea freshening linked to beaufort gyre freshwater release. *Nature communications*, *12*(1), 1–8.